

Dissertation zur Erlangung des Doktorgrades
der Fakultät für Chemie und Pharmazie
der Ludwig-Maximilians-Universität München

Iron Fumarate Nanoparticles
as Carriers for
Functional Biomacromolecules

Negar Mirzazadeh Dizaji

aus

Tabriz, Iran

2024

Erklärung

Diese Dissertation wurde im Sinne von § 7 der Promotionsordnung vom 28. November 2011 von Herrn Prof. Dr. Thomas Bein betreut.

Eidesstattliche Versicherung

Diese Dissertation wurde eigenständig und ohne unerlaubte Hilfe erarbeitet.

München, 03/03/2025

Negar Mizazadeh Dizaji

Dissertation eingereicht am: 12/11/2024

1. Gutachter: Prof. Dr. Thomas Bein

2. Gutachterin: Prof. Dr. Hanna Engelke

Mündliche Prüfung am: 20/12/2024

Acknowledgment

I am grateful to the individuals who have been significant in my life and supported me throughout my PhD journey. Your assistance and companionship have been invaluable, and without you, completing this doctoral dissertation would not have been possible.

First and foremost, I want to express my sincere appreciation to my supervisors, Prof. Thomas Bein and Prof. Hanna Engelke, for their consistent support and invaluable guidance during my PhD experience. Their expertise and insights in science have been instrumental in overcoming challenging projects and achieving success. I am truly grateful for their kindness, patience, and unwavering support throughout my doctoral journey.

I extend my heartfelt appreciation to Prof. Wagner, Prof. Tinnefeld, and Prof. Lamb for their generosity in providing access to their facilities and supporting my research.

I am extremely grateful to Dr. Ulrich Lächelt, Dr. Stefan Wuttke, and Dr. Alexander Borodavka for their invaluable contributions to our fruitful discussions. Their insights, expertise, and constructive input have greatly enriched our collaborative efforts, leading to significant progress and advancements in our work. A heartfelt thank you goes out to Yi Lin for his exceptional collaboration. His dedication, professionalism, and positive attitude have greatly enhanced our teamwork, fostering an environment of mutual respect and shared success. It has been a pleasure working together.

A special thank you goes to our secretary, Corrina Heidt, whose efficient support, organization, and assistance have greatly facilitated the administrative aspects of my work. Thanks also to Dr.

Steffen Schmidt for helping me with SEM microscopy measurement and Tina Reuther for her invaluable support in the lab.

I am thankful to the Meso-bio subgroup members for their company and engaging discussions, which have cultivated a supportive and motivating research atmosphere. I also want to express my appreciation to all the AK Bein members for their assistance and for contributing to a positive work environment.

I would also like to express my sincere appreciation to DAAD for their generous scholarship, which has provided me with the financial support necessary to pursue my doctoral studies.

To my beloved family, wonderful parents, and lovely brother, thank you for your unconditional love, unwavering support, and endless encouragement throughout this journey. Your belief in me has been a constant source of strength and motivation.

Last but not least, I express my deepest gratitude to my husband, Amir, for his love, patience, understanding, and unwavering support during the ups and downs of my doctoral studies. Your presence and encouragement have been my solace, and I am deeply grateful for your consistent belief in me.

Abstract

In recent decades, biomacromolecules like proteins, mRNA, and the CRISPR-Cas system have become indispensable in medical and biotechnological fields, paving the way for new therapeutic strategies and advancements. While proteins play essential roles in cellular processes, driving interest in them for therapy and drug development, mRNA acts as a versatile intermediary between DNA and protein synthesis, finding applications from vaccines to gene therapy. Similarly, the CRISPR-Cas system has transformed genetic manipulation, offering precise genome editing for therapeutic purposes. However, challenges like poor stability, rapid degradation, and limited cellular uptake often hinder the effective utilization of these biomacromolecules. To address these obstacles, nanoparticles (NPs) emerge as promising solutions to overcome these challenges and unlock innovative healthcare approaches.

Among the diverse array of NPs, the hybrid metal-organic nanoparticles have garnered significant attention due to their intriguing and unique properties, including tunable size, biocompatibility, and versatile surface chemistry. These characteristics render metal-organic NPs highly suitable for encapsulating and delivering biomacromolecules, enhancing their stability, promoting cellular uptake, and enabling targeted delivery. Iron-fumarate nanoparticles (Fe-fum NPs), a subclass of metal-organic NPs, possess unique characteristics stemming from their composition, which includes iron ions coordinated with fumarate ligands. These NPs demonstrate magnetic behavior, offer tunable sizes, and can encapsulate diverse cargoes. The controlled synthesis and modification of Fe-fum NPs have paved the way for their potential application across various domains in medicine and biotechnology. Although the capacity of Fe-fum NPs to store therapeutic small

molecules and effectively release them to cancer cells is well established, their potential for delivering functional biomacromolecules, such as proteins and RNAs, has been relatively underexplored. The inherent pore sizes of Fe-fum nanoparticles prove insufficient to accommodate the dimensions of numerous proteins and RNA molecules, thus posing challenges for their effective entrapment within the nanoparticle pores. To overcome this limitation, *in situ* encapsulation of biomacromolecules in Fe-fum NPs emerges as a promising strategy, in which the nanoparticles form around biomacromolecules via a biomimetic mineralization process, ensuring a notable loading efficiency and minimal premature leakage of the biomacromolecule.

The *in situ* encapsulation of biomacromolecules within Fe-fum NPs needs meticulous attention to synthesis conditions. This involves transitioning to water-based synthesis methods to eliminate harmful solvents, maintaining a pH near the physiological range of around 7.4, and avoiding high temperatures. Such measures are essential for preserving these delicate biomacromolecules' structural and functional integrity, thus optimizing the efficacy of Fe-fum NPs as carriers for such molecules. Initial efforts in our study to reevaluate the synthesis according to the conditions mentioned above encountered a novel challenge: either the nanoparticles increased in size or underwent aggregation. Achieving small, uniformly sized particles is crucial to optimizing their distribution within the body and facilitating cellular uptake. Thus, the first part of this thesis focuses on investigating the impact of various synthesis parameters, including solvents, modulators, and coatings, on the size, aggregation, and degradation of Fe-fum NPs synthesized using a biomimetic mineralization approach that preserves protein integrity. Our findings reveal specific conditions that facilitate the production of colloiddally stable Fe-fum NPs capable of incorporating proteins. Applying a lipid coating after the synthesis of nanoparticles stabilized the

size of Fe-fum in an aqueous buffer, allowing for cellular applications. Another crucial aspect of nanoparticles is their ability to release their cargo into the cytoplasm of cells after cellular internalization. Often, internalization is mediated via endocytosis, and cytosolic release implies escape from the endosome. The endosomal release ensures the payload reaches its target, facilitating the desired biological effect. In this study, we demonstrate that lipid-coated Fe-fum NPs are internalized by cells, and intracellular release of the loaded proteins and small molecules can be triggered externally via glucose shock. Furthermore, we showed that small molecule cargo can be released from the endosome by leveraging the internal trigger mechanism provided by histidine, offering an additional method for controlled release within the cellular environment.

The second part of this thesis explores the versatility of the introduced biomineralization method involving Fe-fum NPs. It further investigates their capacity to maintain the structural integrity and operational effectiveness of diverse proteins throughout the synthesis and subsequent release process. For this, we initially demonstrated the ability of the Fe-fum NPs to encapsulate four distinct model proteins, including bovine serum albumin (BSA), horse radish peroxidase (HRP), green fluorescent protein (GFP), and Cas9/sgRNA ribonucleoproteins (RNPs). These Fe-fum NPs exhibited notably high loading efficiency for proteins, and facilitated their successful delivery into cells while maintaining protein activity. The delivery of RNPs via Fe-fum NPs resulted in efficient gene knockout in *HeLa* cells. Furthermore, we explored the potential of Fe-fum NPs in safeguarding proteins against harsh environmental conditions. Our findings revealed that integration into Fe-fum NPs effectively preserved and shielded the activity of RNPs even under conditions of pH 3.5 exposure and two months of storage at 4°C, conditions known to compromise the functionality of unprotected RNPs severely.

The last part of this project delved into the potential of Fe-fum NPs as carriers for RNA, with a specific focus on mRNA delivery. Using a biomineralization technique during synthesis, RNA molecules were successfully integrated into the Fe-fum NPs, facilitating their efficient delivery into cells. Moreover, the utilization of mCherry-encoding mRNA as a model RNA confirmed the successful translation and production of mCherry protein within the cells upon glucose shock, indicating the intact delivery of mRNA and subsequent translation process. These findings underscore the potential utility of Fe-fum NPs as highly effective carriers for RNA molecules, thereby contributing to the advancement of RNA-based therapeutic and biotechnological applications.

In summary, our study introduces an innovative room-temperature synthesis technique for producing Fe-fum NPs in mildly acidic aqueous settings. We demonstrate the ability to form Fe-fum NPs via biomimetic mineralization around biomacromolecules, encompassing diverse model proteins and large RNA molecules. This establishes an effective platform for delivering such molecules while preserving their functionality. Moreover, Fe-fum NPs were very efficient in safeguarding proteins from degradation during storage and against challenging environmental conditions.

Table of contents

CHAPTER 1	1
1. Introduction.....	2
1.1. Biomacromolecular Therapeutics.....	2
1.1.1. Protein-based Therapeutics	2
1.1.2. RNA-based Therapeutics	6
1.1.3. CRISPR/Cas Technology	10
1.2. Biological Barriers to Biomacromolecular Therapeutics	13
1.3. Nanoparticles (NPs) as delivery vehicles for therapeutics	15
1.3.1. Endosomal escape of NPs	16
1.4. NP-mediated Delivery of Biomacromolecules	19
1.5. Metal-organic frameworks	24
1.5.1. Iron Fumarate Nanoparticles	27
1.6. References	30
CHAPTER 2	46
2. Characterization	47
2.1. Dynamic light scattering (DLS)	47
2.2. Zeta potential.....	48

2.3.	X-ray diffraction (XRD)	51
2.4.	Scanning Electron Microscopy (SEM)	52
2.5.	Molecular spectroscopy	54
2.5.1.	Ultraviolet-visible (UV/VIS) spectroscopy	56
2.5.2.	Infrared (IR) Spectroscopy	57
2.5.3.	Fluorescence Spectroscopy	57
2.6.	Fluorescence Microscopy and Confocal Microscopy	59
2.6.1.	Fluorescence Microscopy	59
2.6.2.	Confocal microscopy	61
2.7.	Flow cytometry (FC)	63
2.8.	Agarose gel electrophoresis	65
2.9.	References	67
CHAPTER 3		71
3.	Control of aggregation and degradation of iron fumarate nanoparticles for protein encapsulation and intracellular delivery	72
3.1.	Introduction	73
3.2.	Results	74
3.2.1.	Size control	74
3.2.2.	Protein encapsulation	80

3.2.3.	Cytosolic release	81
3.3.	Conclusion.....	85
3.4.	Material and methods.....	86
3.4.1.	Synthesis.....	86
3.4.2.	Characterization methods	91
3.5.	References	93
3.6.	Supplementary figures	98
CHAPTER 4	104
4.	Biomimetic Mineralization of Iron-Fumarate Nanoparticles for Protective Encapsulation and Intracellular Delivery of Proteins.....	105
4.1.	Introduction.....	107
4.2.	Results.....	109
4.2.1.	Synthesis and Characterization of Biomimetically Mineralized Iron-fumarate Nanoparticles	109
4.2.2.	Intracellular Delivery of BSA.....	113
4.2.3.	Intracellular Delivery and Activity of HRP	114
4.2.4.	Intracellular Delivery, Activity, and Preservation of Cas9/sgRNA RNPs.....	116
4.3.	Conclusion.....	121
4.4.	Material and methods.....	121

4.4.1. Synthesis.....	121
4.4.2. Characterization methods.....	124
4.5. References.....	132
4.6. Supplementary figures.....	138
CHAPTER 5.....	152
5. Intracellular delivery of mRNA by iron-fumarate nanoparticles.....	153
5.1. Introduction.....	154
5.2. Results.....	155
5.3. Conclusion.....	161
5.4. Materials and methods.....	161
5.4.1. Synthesis.....	161
5.4.2. Characteristic methods.....	162
5.5. References.....	167
5.6. Supplementary figures.....	172
CHAPTER 6.....	176
6. Conclusion and Outlook.....	177
CHAPTER 7.....	180
7. Curriculum Vitae.....	181

CHAPTER 1

Introduction

1. Introduction

1.1. Biomacromolecular Therapeutics

In medicinal research, small molecules have long been the center of attention. Small molecule-based therapeutics typically act by binding to specific target proteins and interfering with their biological activities. However, only a limited number of proteins possess such binding sites¹². Additionally, small molecules might cause undesirable side effects by interacting with multiple targets in the body and unwanted drug-drug interactions³. Despite the fast progress in medical science and technology, finding effective treatments for serious diseases like cancer, neurodegenerative disorders, and metabolic issues is still a big challenge using traditional small-molecule drugs^{4,5}. In recent decades, biomacromolecular therapeutics have shown great promise in addressing these challenges through their ability to precisely target and modulate the complicated biological processes that trigger various diseases. Biomacromolecular therapeutics often cause fewer side effects since they are designed to mimic endogenous molecules. They are also favored for their *in vivo* pharmacokinetics due to their compatibility with biological systems. Moreover, they generally undergo faster FDA approval processes as their well-defined mechanisms of action and reduced toxicity profiles speed up the regulatory assessment⁴. Biomacromolecular therapeutics encompass a diverse range, including proteins, peptides, plasmid DNA, and RNA molecules. This doctoral thesis focuses on therapeutics based on proteins, RNAs, and their combination.

1.1.1. Protein-based Therapeutics

Proteins, a class of biomacromolecules, serve as essential components in the functioning and structure of cells. These molecules are produced from the combination of the 20 standard amino

acids, forming polypeptide chains. The sequence of these amino acids within a protein determines their three-dimensional structure and the specific roles they play in biological systems. This structural arrangement dictates their physical interactions with other molecules, thus their biological functions. Proteins, in their various forms, including hormones, enzymes, and cytokines, are indispensable for life since they maintain essential biological processes, organize sophisticated biological pathways, facilitate communication between cells, and serve many other functions ^{6,7}.

Given the critical role of proteins in various biological processes, any disruption in their functions or dysregulation in their synthesis can lead to diseases or contribute to the development of different medical conditions ⁸. This concept is fundamental in understanding the molecular basis of diseases and developing therapeutic strategies by restoring proper regulation or utilizing dysregulation itself as an indicator for targeting cells that require intervention ^{9,10}. Meanwhile, protein-based therapeutics represent a rapidly expanding frontier in modern medicine, offering innovative solutions for addressing diseases caused by such dysregulation of crucial biological processes. These therapeutics, including hormones, enzymes, monoclonal antibodies, growth factors, and other protein classes, have demonstrated remarkable potential in diagnosing and treating various diseases. One of the simplest examples of a protein-based therapeutic is insulin. Insulin is a naturally occurring protein hormone produced by the pancreas that regulates blood sugar levels. People with diabetes, particularly Type 1 diabetes, have a deficiency in insulin production or impaired insulin function. To manage their condition, they require insulin therapy. This therapy uses synthetic or recombinant human insulin to replace the missing or malfunctioning natural insulin to help regulate blood sugar levels ¹¹. Another example of protein-based therapeutics is enzyme replacement therapies (ERT), which have become a lifeline for individuals with rare

genetic disorders, supplementing missing or defective enzymes to restore proper metabolic functions. While ERT doesn't cure these rare genetic diseases, it can significantly alleviate symptoms and improve the quality of life for people with conditions like Gaucher disease, Fabry disease, and Pompe disease ^{12,13}. A distinguishing characteristic of protein-based therapeutics is their inherent specificity and affinity for specific molecular targets, allowing for precise modulation of complex biological pathways. Monoclonal antibodies, for instance, have revolutionized the treatment of cancer and autoimmune diseases by directly targeting harmful cells while sparing healthy ones ¹⁴. Monoclonal antibodies can recognize and bind to specific molecules or antigens on the surface of cells or pathogens. This binding can neutralize antigens by blocking their function, thus preventing processes like viral entry or cancer cell signaling. Additionally, it can facilitate opsonization by marking the cells or pathogens for phagocytosis by immune cells ¹⁵. The versatility of protein therapeutics extends into the exciting field of regenerative medicine, offering promising avenues for tissue repair and rebuilding. These therapeutic proteins, such as growth factors and cytokines, stimulate cell growth, differentiation, and tissue regeneration. Such proteins can be applied in various contexts, such as wound healing, tissue engineering, and treating degenerative diseases ¹⁶.

Protein-based therapeutics offer numerous advantages compared to small-molecule drugs. First, proteins frequently serve intricate and particular functions that chemical compounds cannot replicate. Additionally, due to the specific nature of protein functions, the probability of protein therapeutics interfering with normal biological processes and causing adverse effects is often reduced. Moreover, as the body naturally produces many of the therapeutic proteins, they are generally well-tolerated and less likely to provoke immune responses ^{7,17}. Furthermore, protein

therapeutics and small molecules follow distinct degradation pathways within the human body. While small molecules undergo enzymatic metabolism mostly in the liver, proteins are primarily degraded by the proteasome and lysosome systems^{18,19}. Therapeutic proteins undergo degradation by proteases and peptidases, like endogenous substrates, ultimately breaking down into amino acids, which are then mostly recovered and reused by the body. This unique degradation process for proteins ensures a higher degree of predictability in drug action and safety, as it prevents the accumulation of non-functional or harmful proteins.

The administration of proteins through intravenous injection has a long history in the field of medicine, with well-established protocols for delivering therapeutic proteins directly into the bloodstream. This straightforward method has been the basis of protein therapies such as insulin administration²⁰. However, with the emergence of advanced approaches like antibody engineering and regenerative medicine, the landscape of protein therapeutics has become more intricate. These therapies often require sophisticated genetic engineering techniques to craft highly targeted antibodies or facilitate tissue repair and replacement. Consequently, these contemporary applications need a more profound comprehension of the intricate biological processes underlying these advancements. Moreover, the challenge of delivering complex protein therapeutics to the proper target tissues or cells without triggering immune responses or side effects has become a critical bottleneck in their development. Hence, addressing these multifaceted issues in biology and delivery mechanisms is crucial to realizing the full potential of more advanced protein-based therapeutics in clinical practice.

1.1.2. RNA-based Therapeutics

RNA (Ribonucleic Acid) is a polymeric molecule that plays a fundamental role in various biological processes. While it was initially believed that RNA molecules only acted as messengers between DNA and protein synthesis, it is now understood that they are involved in numerous cellular activities owing to their diverse secondary and tertiary structures ²¹. The primary structure of RNA is composed of a linear sequence of nucleotides, each made up of a nitrogenous base, a ribose sugar, and a phosphate group ²². The nitrogenous bases of RNA include adenine (A), guanine (G), cytosine (C), and uracil (U) and connect to the ribose sugar molecule via a glycosidic bond. The phosphate group is linked to the carbon at the 3' position of one ribose sugar and the 5' position of the next ribose sugar through a phosphodiester bond. **Figure 1-1** represents a four-nucleotide segment of RNA with all four RNA nucleobases. Due to the presence of the phosphate group, the backbone of an RNA molecule is negatively charged and hydrophilic. RNA's secondary structure arises from a complementary base pairing between nucleotides in the primary sequence. This base pairing forms hydrogen bonds between adenine and uracil or between cytosine and guanine ²³. As a result, RNA can fold into various structural motifs, such as hairpin loops, bulges, internal loops, and stem-loop structures. The tertiary structure of RNA results from additional interactions between different regions of the RNA molecule, ultimately shaping its three-dimensional architecture. These interactions contribute to RNA's overall stability and functionality ²⁴. RNA's ability to adopt diverse structures allows it to participate in essential cellular processes, including gene expression, protein synthesis, regulation of gene expression, and catalysis of biochemical reactions ²⁴.

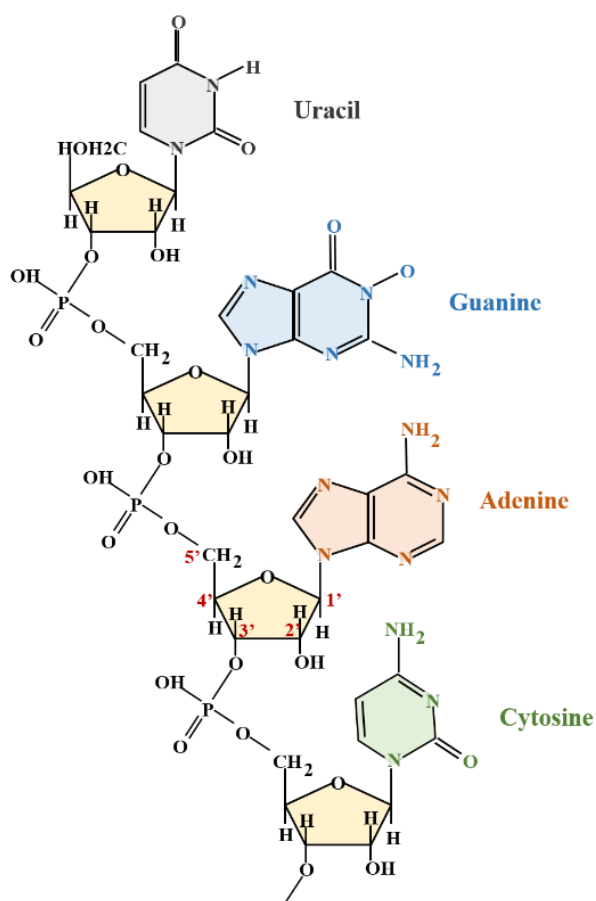


Figure 1-1. RNA primary structure showing a four-nucleotide segment of RNA with all four RNA nucleobases.

Over the last few decades, RNA-based therapeutics have attracted significant interest from academia and the industry ^{25,26}. The diversity in RNA structures offers flexibility in designing therapeutic approaches; based on their function mechanism, RNA molecules have been studied to treat various diseases, including genetic disorders, infectious diseases, and cancers ^{27,28}. Some of the major types of therapeutic RNA include small interfering RNA (siRNA), micro-RNA (miRNA), and messenger RNA (mRNA), each with a distinct function mechanism. For example, siRNA and miRNA, which are small and double-stranded RNA molecules, function by binding to

a complementary sequence on mRNA. They can inhibit translation or induce mRNA degradation, leading to a blockage or reduction in protein translation, thereby regulating gene expression.²⁹ In contrast, mRNA's principal concept is to trigger the production of target protein transiently after reaching the protein biosynthesis machinery called the ribosome²⁷. They can be used to express a deficient protein or antigen for vaccination^{26,30}. The subsequent section will place a greater emphasis on mRNA-based therapeutics.

1.1.2.1. IVT mRNA Technology

Messenger RNA (mRNA) is a single-stranded RNA synthesized from a DNA template. It is the carrier of coding information, subsequently translated and processed to yield functional proteins³¹. Recently, there has been growing interest in utilizing *in vitro* transcribed (IVT) mRNA as a potential novel drug class for delivering genetic information. IVT-mRNA molecules are designed to mimic natural mRNA for transiently expressing proteins³². IVT-mRNA-based therapeutics offer several advantages over traditional protein-based, plasmid DNA (pDNA)-based, and other conventional approaches.

While in protein-based therapeutics, several copies of a protein need to be delivered into the cells, in mRNA-based approaches, once a single mRNA molecule reaches the cytosol, it can be translated to numerous copies of protein³³. Additionally, mRNA therapeutics are more straightforward to design and manufacture than small molecule- or protein-based approaches that facilitate faster control over cancer mutations or unexpected epidemic diseases³⁴. mRNA therapeutics allow for a quicker and more scalable manufacturing process, as the same production infrastructure can be repurposed for multiple applications by simply altering the genetic code within the mRNA. This inherent versatility makes mRNA an attractive platform for developing

novel therapies and vaccines, offering a promising avenue for addressing various diseases and medical challenges. This flexibility was underscored during the COVID-19 pandemic when scientists quickly developed mRNA vaccines, such as the Pfizer-BioNTech and Moderna vaccines, in response to the emergent SARS-CoV-2 virus. Traditional vaccine development methods would have taken significantly longer³⁵. Another significant benefit of the mRNA-based approach is the production of proteins by host cells in a natural manner. Consequently, the generated proteins undergo essential post-translational processing, such as glycosylation, subunit cleavage, and proper protein folding, ensuring the integrity and functionality of the produced proteins³⁶.

IVT-mRNA offers several advantages over plasmid DNA (pDNA) concerning the intracellular expression of disease-related proteins. One key benefit is that IVT-mRNA molecules only need to reach the ribosomes in the cytosol for translation into proteins, whereas pDNA molecules need to enter the nucleus. As a result, IVT-mRNA-mediated protein expression bypasses the biological barrier of the nuclear membrane, facilitating the direct translation into proteins within the cytoplasm³⁷. Additionally, given its site of action, IVT-mRNA reduces the risk of integration with the host genome. This holds significant importance as pDNA has the potential to integrate into the host genome, causing certain risks, such as unintended gene mutations and disruptions to normal cellular function. Additionally, the integration of pDNA into the host genome may lead to unpredictable gene expression patterns, autoimmune reactions, and the activation of dormant viruses. By utilizing IVT-mRNA, these integration-related concerns are minimized^{34,38}. Moreover, mRNA gene therapy eliminates the requirement for selecting a specific promoter, making the transfection process relatively efficient and direct³⁹. Another advantage of therapeutic IVT-mRNA is that, similar to endogenous mRNA, they are subject to cellular regulatory processes.

After fulfilling their intended function, they are typically degraded within cells and have a relatively short lifespan, typically ranging from a few hours to a few days. This controlled degradation is an important aspect of how mRNA-based therapies are designed to work, ensuring that their effects are temporary and reversible, with a limited duration of presence in cells ⁴⁰.

In 2023, the Nobel Prize in Physiology or Medicine was awarded for groundbreaking discoveries in the field of mRNA technology. The prize recognized the pioneering work of scientists who revolutionized medical research and treatment through the development and application of mRNA-based vaccines and therapeutics. Their innovative breakthroughs not only enabled the rapid development of effective vaccines against infectious diseases such as COVID-19 but also opened new avenues for treating a wide range of ailments, from cancer to genetic disorders. The Nobel Committee's decision underscored the transformative impact of mRNA technology on global health and reaffirmed the importance of scientific innovation in addressing pressing healthcare challenges.

1.1.3. CRISPR/Cas Technology

Clustered Regularly Interspaced Short Palindromic Repeats (CRISPR) and CRISPR-associated protein (Cas), also known as CRISPR/Cas technology, is a revolutionary gene-editing tool that has transformed the field of genetics and molecular biology ^{41,42}. CRISPR technology combines protein-based and RNA-based approaches, enabling precise and targeted gene editing. This innovative synergy allows for the modification, deletion, or insertion of genetic material with remarkable precision, revolutionizing genetic engineering and offering potential treatments for genetic disorders, advanced research tools, and therapeutic solutions for different medical conditions ⁴³. CRISPR/Cas systems encompass a variety of Cas proteins, each with distinct

characteristics and applications. Cas9 stands out as one of the most prevalent and extensively studied Cas proteins due to its simplicity, versatility, efficiency, and specificity ⁴¹. The protein component, Cas9, acts as a molecular scissor, guided by the RNA component (usually single-guide RNA or sgRNA) to locate and edit specific DNA sequences ⁴³. **Figure 1-2** provides a schematic of CRISPR/Cas9 machinery depicting the Cas9 endonuclease enzyme's role in cleaving DNA at a precise location as directed by the guiding RNA component. CRISPR/Cas is an applicable technology to be used as a therapeutic method against many different targets, such as viruses ⁴⁴, bacteria ⁴⁵, cancer ⁴⁶, and neurodegenerative diseases ⁴⁷.

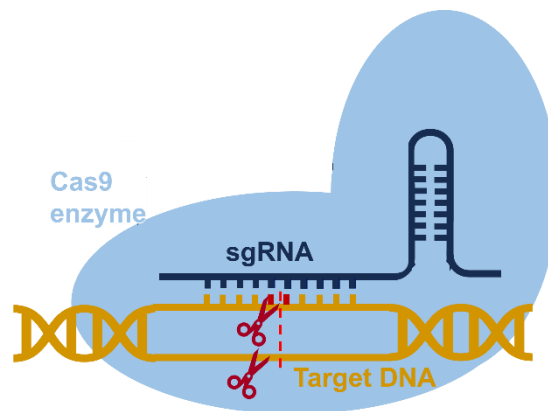


Figure 1-2. The CRISPR/Cas9 System. The CRISPR/Cas9 system consists of a single guide RNA (sgRNA) and Cas9 nuclease, which is able to cleave DNA at specific sites marked by the sgRNA.

An essential need for the CRISPR/Cas9 complex to operate effectively is the efficient delivery of the complex into the nuclei of the target cells. CRISPR/Cas can be introduced to cells via plasmid DNA (pDNA)-mediated expression of Cas9 and sgRNA, or mRNA-mediated expression of Cas9, or through the delivery of recombinant Cas9 protein and sgRNA ribonucleoprotein (RNP)

complexes into cells. (**Figure 1-3**)⁴⁸. The delivery of the RNP complex provides a transient method for gene editing, circumventing numerous challenges typically associated with the other two delivery strategies. The direct introduction of Cas9 protein eliminates potential delays related to protein expression, reducing the risk of sgRNA degradation before performing its action. This, in turn, could have significant implications for pharmacokinetics and pharmacodynamics (PK-PD), as the steps involved in getting the right genetic instructions and the editing tool to the right place in the cell happen in a more straightforward sequence, which can make the entire process more efficient and predictable⁴⁹. Moreover, controlling the amount of Cas9 within the cell through

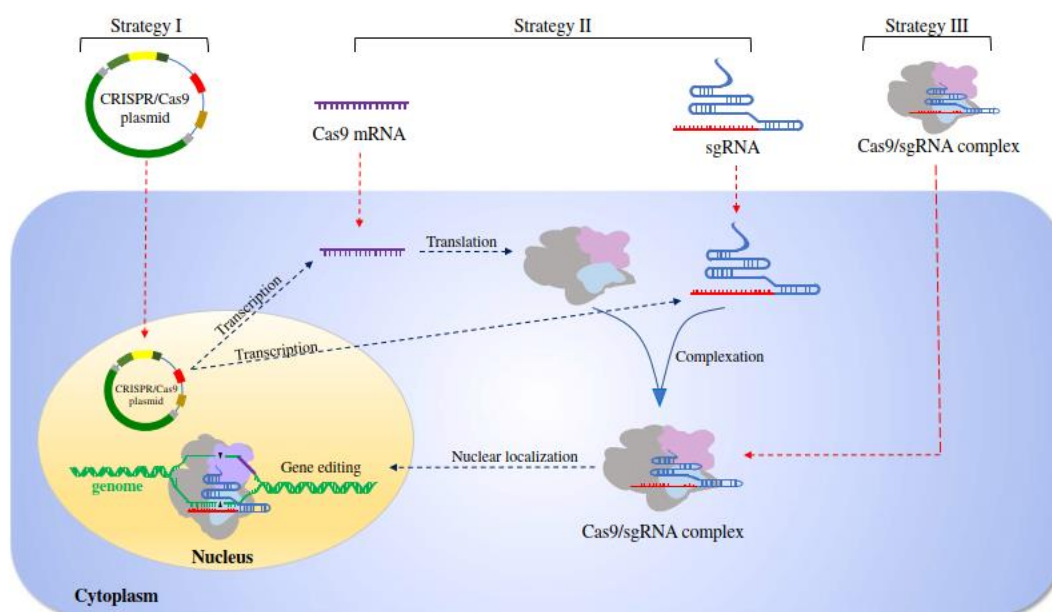


Figure 1-3. Different strategies for introducing CRISPR/Cas9 system into the cells. The first strategy involves utilizing a plasmid-based CRISPR/Cas9 system that encodes both the Cas9 protein and sgRNA within the same vector. The vector itself encodes both the Cas9 protein and sgRNA, which then combine within cells to form the Cas9/sgRNA complex for genome editing. The second strategy implies delivering a mixture of Cas9 mRNA and sgRNA. Inside the cells, the Cas9 mRNA is translated into Cas9 protein, which subsequently combines with sgRNA to create the Cas9/sgRNA complex. The third strategy engages directly in delivering the Cas9/sgRNA complex into the cells, bypassing the need for additional components or processes. Image reproduced from Liu *et al.*, 2017⁴⁸.

direct protein application offers a crucial advantage over plasmid-based expression, lowering the risk of excessive Cas9 levels and potential off-target cleavage. This reduces the chances of unintended changes in the genome at locations other than the intended target. Moreover, insertional mutagenesis is a concern when foreign genetic material is permanently integrated into the host genome, potentially disrupting normal gene function. Direct delivery of RNP does not involve the permanent integration of foreign DNA, reducing the risk of insertional mutagenesis. Furthermore, the delivery of RNPs provides a reliable framework for cells with limited transcription and translation activity ⁴¹. These advantages of RNP delivery make it a promising platform in the CRISPR/Cas genome editing technology field.

1.2. Biological Barriers to Biomacromolecular Therapeutics

Most novel drug candidates, including biomacromolecular therapeutics, need to efficiently penetrate the cytosol in sufficient concentration to achieve their therapeutic objectives ⁵⁰. After drug administration, various natural barriers, including serum proteins like proteases, renal clearance systems, vascular endothelial barriers, cellular membranes, and more, present substantial challenges for biomacromolecular therapeutics to reach their intracellular targets at the needed concentrations ⁴.

The primary challenge during the circulation of biomacromolecules involves the binding and altering of their characteristics by serum proteins. The stability of biomacromolecules is challenged by enzymes naturally existing in the blood, such as proteases and RNases (**Figure 1-4 a**). These enzymes can significantly impact the half-life of biomacromolecules ^{51,52} Following administration into the bloodstream, biomacromolecules are eliminated from circulation through renal or hepatic clearance, which is strongly enhanced by the binding of serum proteins (**Figure**

1-4 b)⁵³. One of the most substantial challenges specific to biomacromolecular therapeutics relates to their interactions with cellular membranes and the resistance posed by vascular endothelial permeability⁵⁴. In the case of many diseases, therapeutics need to traverse endothelial cell vessel barriers to access the target tissues. A highly severe example of this challenge is the blood-brain barrier, which acts as a highly selective semipermeable boundary and effectively restricts the passage of most biological drugs to the central nervous system⁵⁵.

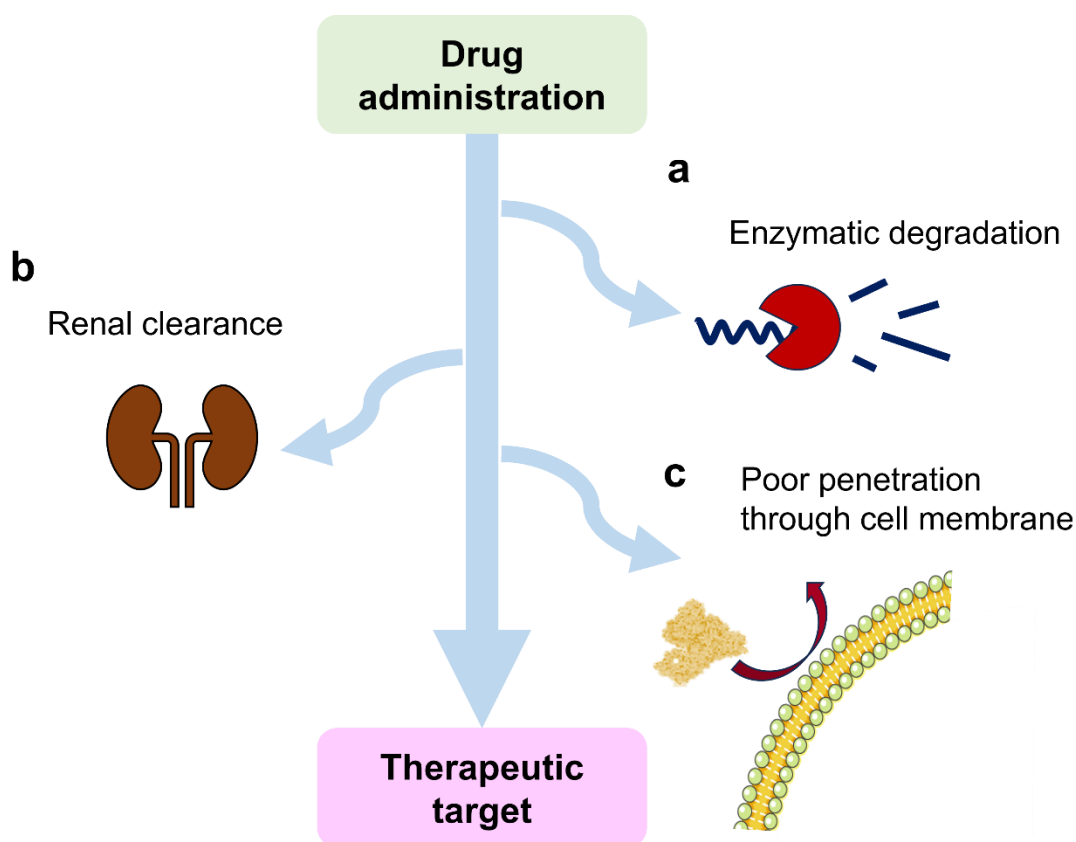


Figure 1-4. Biological barriers present significant obstacles for biomacromolecules to reach their intended targets after administration. (a) enzymatic degradation, **(b)** renal clearance can quickly diminish their bioavailability, and **(c)** the restricted membrane permeability of biomacromolecules limits their ability in reaching intracellular targets.

Last but not least, when biomacromolecules manage to reach the targeted cells, they often face one of the most prominent hurdles, which is the challenge of traversing the cell membrane's lipid bilayer. This lipid bilayer envelops cells and is a protective barrier that selectively controls what enters and exits the cell. Cellular uptake becomes a critical concern as biomacromolecules may be too large, negatively charged, or hydrophilic to traverse the hydrophobic cell membrane efficiently. This challenge is particularly pronounced when attempting to deliver therapeutic payloads directly into the cell's interior, where they can exert their intended effects.⁵⁶ (**Figure 1-4 c**).

Overcoming these obstacles and achieving successful intracellular delivery of intact biomacromolecules in the target tissue is crucial for enhancing the efficiency of biomacromolecular therapeutics. Optimizing biomacromolecule modifications, utilizing targeted approaches, and, more importantly, developing innovative delivery strategies can help to improve the intracellular delivery of these therapeutics, ultimately maximizing their therapeutic potential and efficacy.

1.3. Nanoparticles (NPs) as delivery vehicles for therapeutics

The development of innovative delivery methods can help improve the intracellular delivery of biomacromolecular therapeutics, ultimately maximizing their therapeutic potential and efficacy. Recent advancements in nanotechnology have revealed the potential of nanomaterials as promising vectors that can overcome various biological barriers to successful drug delivery. With their specific size-dependent physicochemical properties, nanoparticles provide a unique platform for drug delivery purposes. During the last few decades, many efforts have been made to develop

nanocarriers for controllable drug release in targeted tissue that reduce side effects and enhance therapeutic efficacy ⁵⁷.

A beneficial NP-mediated delivery system needs primarily high encapsulation efficiency, the ability to protect the cargo from degradation, deliver it to the target tissue, and the ability to internalize into the cell. Once internalized by the cells, they must facilitate the escape of the cargo from endosomal entrapment and release their cargo efficiently into the cells ^{58,59}.

1.3.1. Endosomal escape of NPs

Most nanoparticle delivery systems enter cells via a process called endocytosis ⁶⁰. This process is facilitated by specific interactions on the cell surface or involves the nonspecific engulfment of molecules in the extracellular fluid ^{61,62}. The internalized particles then become confined within membrane-bound endosomes and navigate through a complex endosomal pathway, including early endosomes, recycling endosomes, multivesicular bodies, late endosomes, and lysosomes ⁶³. The particles internalized by this pathway may undergo recycling back to the cell surface or face degradation due to exposure to lysosomal enzymes ⁶⁴. When nanoparticles remain entrapped within endosomes, the cargo encapsulated within the NPs is essentially trapped in the endosome unless it possesses the ability to penetrate the endosomal membrane. This constraint imposes limitations on the types of biomacromolecules that NPs can effectively carry. They must either be biomacromolecules that are inherently effective within the endosome environment or possess the unique capability to escape the endosome. However, most biomacromolecules with therapeutic potential, such as nucleic acids and specific proteins, primarily exert their effects in the cytosol. This presents a significant challenge because these molecules typically cannot cross cellular membranes independently. As a result, there is a critical need for endosomal escape mechanisms

to facilitate cargo release from endosomes and enable the therapeutic molecules to reach their target sites in the cytosol, where they can exert their intended biological effects ⁶⁵. There are four main mechanisms through which nanoparticles can facilitate endosomal escape, as outlined below and depicted schematically in **Figure 1-5**:

1) Fusion with endosomal membrane: Some nanoparticles or vesicles can fuse with the endosomal membrane, effectively becoming a part of it. This fusion disrupts the endosomal membrane's integrity, and the nanoparticle undergoes a structural transformation where it essentially turns inside out. Consequently, the simultaneous escape from the endosome and the nanoparticle enables the release of cargo into the cytoplasm ⁶⁶ (**Figure 1-5 a**).

2) Osmotic pressure: As endosomes mature, ATPase proton pumps within their membranes actively transport protons from the cytosol into the endosomes, acidifying endosomal compartments and activating hydrolytic enzymes ⁶³. Nanoparticles, which possess buffering capacities, prevent the endosome's pH decrease and prompt the cell to maintain proton pumping into the endosome to achieve the desired pH level. As a result, this causes the influx of chloride ions and water molecules, increasing the pressure within the endosome and ultimately leading to its rupture ^{67,68}. Another proposed mechanism based on osmotic pressure is that the endosome's pH reduction leads to the particles' instant disintegration into numerous sub-units. This sudden change induces a significant rise in osmotic pressure within the endosome, triggering the release of cargo ⁶⁹ (**Figure 1-5 b**).

3) Swelling: Many nanoparticles have been designed to swell within endosomes or lysosomes when the pH drops. Some researchers have proposed that the physical stress from particle swelling

can cause the endosome to tear, allowing the loaded cargo to enter the cell's interior⁷⁰ (**Figure 1-5**

c).

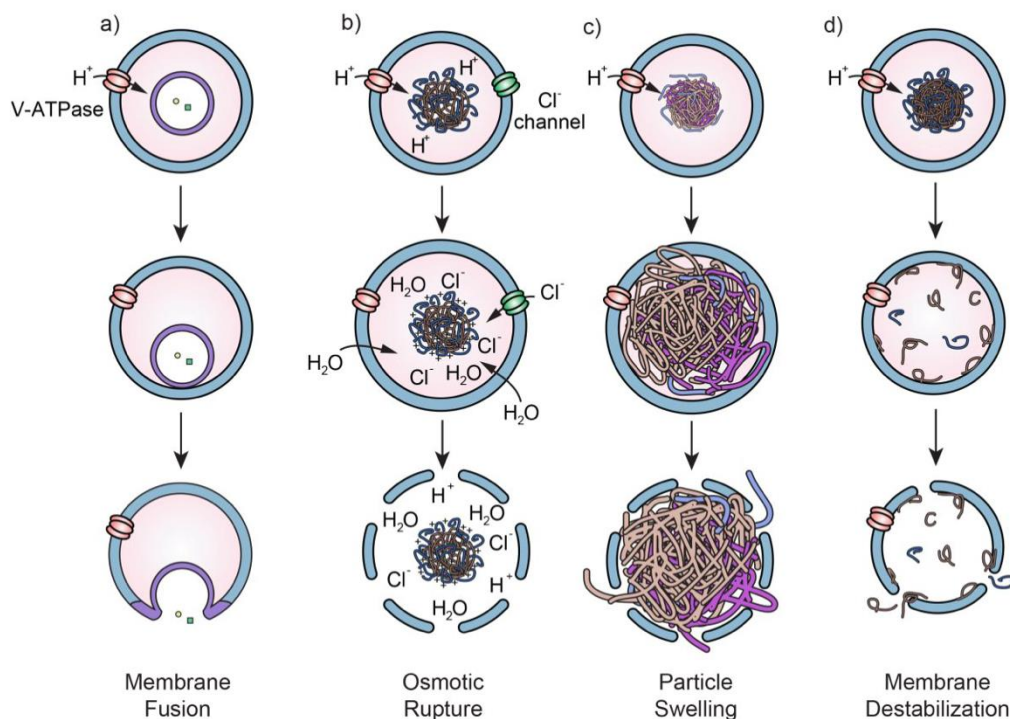


Figure 1-5. Schematic of proposed mechanisms for endosomal escape induced by NPs. (a) Fusion between the nanoparticle structure and the endosomal membrane, (b) Buffering within the acidifying endo/lysosome leads to an influx of chloride ions and subsequent endo/lysosome lysis due to elevated osmotic pressure. (c) The swelling of pH-responsive nanogels results in the rupture of the endosomal membrane via increased mechanical strain. (d) pH-responsive nanoparticles escape by disassembling and destabilizing the endosomal membrane. Image reproduced from Smith *et al.*, 2019⁶⁸.

4) Membrane destabilization and pore formation: Nanoparticles can be designed to release specific materials, compounds, or peptides when they are within the endosome. For example, pH-sensitive nanoparticles can be engineered to dissociate or release their cargo in response to the acidic environment of the endosome. Then, the released substances can interact with the lipids in the endosomal membrane, causing significant internal membrane stress capable of generating

pores within the lipid membrane. The process of pore formation enables the release of the content into the cytoplasm^{70,71} (**Figure 1-5 d**).

1.4. NP-mediated Delivery of Biomacromolecules

Due to the growing number of newly developed and approved biomacromolecular therapeutic agents, designing suitable delivery systems for these drugs is an increased need. Nanomaterials have been extensively investigated for the delivery of biomacromolecules. They can employ various strategies, including complexation, absorption, or encapsulation of the molecules, to facilitate efficient and controlled delivery of biomacromolecular therapeutics^{72,73}. Up to now, different types of nanocarriers have been established for biomacromolecule delivery, including organic materials (e.g., lipid and polymer-based NPs) and inorganic materials (e.g., mesoporous silica and metal-based NPs) and hybrid metal-organic materials.

Lipid-based nanomaterials

Lipid-based nanoparticles from synthetic and naturally derived sources are one of the most advanced nanocarriers for RNA and protein delivery²⁷. Lipids and liposomes, whether anionic, cationic, or neutral, have undergone extensive research to deliver biomacromolecules into mammalian cells. Generally, non-cationic lipids or liposomes exhibit lower *in vitro* and *in vivo* delivery efficiency when compared to cationic ones⁷⁴. In typical lipid-based formulations for RNA delivery, cationic liposomes form lipoplex complexes with negatively charged RNA molecules through electrostatic interactions, resulting in an overall positive charge. This electrostatic binding ensures effective encapsulation and protection of the RNA payload within the nanoparticles and facilitates the association with negatively charged cell membranes and, thus, efficient delivery to

the target cells⁷⁵. Moreover, due to their high positive charge, they can cause an endosomal rupture by initiating a proton sponge effect or interaction with anionic lipids of the endosomal membranes, resulting in the release of encapsulated biomacromolecules into the cytoplasm^{74,76}. On the other hand, the high tendency of cationic liposomes to interact and disrupt the cellular membranes increases their cytotoxicity compared to anionic or neutral liposomes⁷⁶.

Non-cationic lipids or liposomes can be used in combination with cationic lipids to create lipid-based NPs with specific properties for biomacromolecule delivery. These formulations are often tailored to achieve desired characteristics such as stability, targeting, and controlled release. The choice of lipids and their combinations can be adjusted based on the specific requirements of the delivery system and the type of biomacromolecule being transported. This flexibility in lipid selection allows for a broad range of lipid-based NP formulations, each designed to optimize the delivery of different biomacromolecules. An example of commercially available reagents of this group is the well-known LipofectamineTM class of reagents, which has become prevalent for *in vitro* RNA transfections⁷⁵. An instance of the innovative use of lipid-based NPs can be seen in the COVID-19 mRNA vaccine, which utilizes these nanoparticles to deliver the mRNA encoding the spike protein of the virus, providing an effective means of protection against the disease⁷⁷. Lipid-based NPs, mainly based on cationic lipids, have also been studied extensively for protein delivery for decades. Proteins have been integrated into liposomal NPs using various techniques, including reverse-phase evaporation, injection, freeze-thaw cycles, extrusion, and dry lipid hydration, resulting in varying incorporation efficiency⁷⁸. Commercial transfection agents like Lipofectamine CRISPRMAX and 2000 are examples of cationic lipid-based NPs assessed for their effectiveness in delivering negatively charged Cas9-RNPs into cells⁷⁹.

Despite the ease of formulation and facile synthesis, some drawbacks limit the application of lipid-based NPs as effective carriers: Liposomes tend to fuse or undergo conformational changes during long-term storage, which can compromise their original structure. This instability poses a significant risk of molecular leakage, leading to decreased delivery efficiency. Furthermore, due to the susceptibility of lipid moieties to oxidative reactions and hydrolysis of phospholipids, such chemical interactions can result in undesired alterations in the permeability of the liposome bilayer⁸⁰. Additionally, such reactions can generate byproducts that have the potential to adversely impact sensitive biomacromolecular cargo. For example, the presence of certain chemical functional groups, such as those involved in oxidation, hydrolysis, or transesterification, during storage can lead to mRNA degradation. This degradation process involves the cleavage of the mRNA backbone into smaller fragments⁸¹.

Polymer-based nanomaterials

Polymer-based nanomaterials are commonly derived from biocompatible and biodegradable polymers, wherein the drug is entrapped, encapsulated, or attached to the nanoparticle matrix, resulting in diverse architectures, including polyplexes, layer-by-layer assemblies, nanogels, polymersomes, etc⁸². Polymeric nanomaterials can comprise many sources, including natural polymers like chitosan and synthetic ones, such as poly-L-lysine and polyethylenimine^{83,84}. These NPs also come in diverse chemistries and physical attributes, providing the capacity to shield the payload from degradation, facilitate the controlled release of cargo, and allow structural modifications to adjust their physicochemical properties⁸⁵.

Recently, there has been substantial research on using polymeric NPs for mRNA delivery. Cationic polymers represent the most prevalent type of this group for mRNA delivery owing to their ability to bind and condense the negatively charged mRNA via the electrostatic interaction and forming polyplexes^{1,72}. The entire Cas9-RNP complex also carries a negative charge, which facilitates the forming of complexes with cationic systems⁸⁶. The positive charge of cationic polymers can promote cellular uptake by interaction with negatively charged cell membranes, facilitating endocytosis and the uptake into the cells. Cationic polymers can be designed to improve endosomal escape via various mechanisms, including pH-responsiveness, membrane interaction, and osmotic swelling⁷⁴.

While negatively charged biomacromolecules are very suitable for interaction with cationic polymers, creating polyplexes with other proteins can be challenging since they may exhibit moderate or neutral charges under physiological conditions, depending on their isoelectric point⁸⁷. This necessitates the use of biological or chemical modifications of biomacromolecules or carriers to facilitate electrostatic interactions. However, these modifications may potentially interfere with the proteins' biological functions and add complexity to the system.⁷⁸

Besides their wide use and various advantages, polymeric NPs have some drawbacks, such as charge density, dose-limiting toxicity, and relatively low transfection efficiency except for a few polymers with optimized transfection efficiencies^{27,88}. Furthermore, the systemic administration of polyplexes faces challenges due to their instability in physiological settings. Physiological salts and blood proteins can easily interact with polyplexes, increasing the likelihood of premature payload release and even complete dissociation before reaching its intended target⁸⁹. Moreover, the choice of polymer and formulation parameters must align with the physical and chemical

properties of the cargo molecule, such as size, charge and charge density, solubility, and stability. Different biomacromolecules may require distinct polymers and NP designs. Thus, a distinct polymer may not be universally applicable to all biomacromolecules.

Inorganic nanomaterials

In general, inorganic nanocarriers are represented by solid nanoparticles, often derived from metallic compounds, but they can also originate from mineral substances like silica or phosphate⁷⁸. These NPs can be designed to exhibit diverse sizes, structures, and physical properties resulting from the properties of their core materials⁹⁰. The advantages of inorganic nanocarriers include the ability to conduct synthesis in an aqueous medium, unique properties, and chemical reactivity that could enable alternative targeting mechanisms (e.g., magnetic properties), and practical imaging attributes (e.g., optical properties)^{72,91,92}. Gold NPs (AuNPs) are one of the most studied examples of inorganic nanomaterials known as bioinert. They are popular because of their simple synthesis, biocompatibility, and facile functionalization with thiol groups. In the field of biomacromolecule delivery, these NPs have been studied for the delivery of RNA, proteins, and Cas9/sgRNA complexes^{5,27,93}. One important feature of AuNPs is the high surface-to-volume ratio, enabling them to increase the payload-to-carrier ratio and significantly improve the delivery effectiveness of AuNPs. For example, thiol-functionalized nucleotide molecules can be directly grafted on AuNPs, and the degree of grafting can be controlled by using different thiol groups (i.e., monothiol-, tetrathiol-, etc.). This strategy is highly effective for augmenting the quantity of loaded nucleic acid⁹⁴.

Silica-based nanoparticles are other prevalent inorganic nanoparticles that have demonstrated successful applications in drug delivery and provide numerous benefits in terms of their loading capacity and ease of functionalization. They have gained popularity as delivery carriers due to their chemical stability, thermal resistance, extended cargo-loading capabilities, and adaptable structure. They have shown efficiency in delivering CRISPR/Cas RNP and RNA molecules ⁹⁵. Other types of inorganic NPs, such as quantum dots, iron oxide, and calcium phosphate nanoparticles, possess distinct structural attributes, each with inherent advantages, such as responsive release to external stimuli, favorable distribution within the body, and reactivity to photothermal processes ⁵.

Nonetheless, the clinical utility of inorganic NPs is constrained by poor solubility and safety issues, particularly when heavy metals are incorporated into the formulations ⁵⁴. Moreover, inorganic nanoparticles predominantly adhere biomacromolecules to their surfaces through non-covalent bonding or covalent bioconjugation, which yields restricted protection against *in vivo* degradation for these biomacromolecules. Notably, when the payload is introduced into pores, for example, in the case of using mesoporous silica nanoparticles, it can be susceptible to significant leakage ⁹⁶. Inorganic NPs are in the initial phases of advancement and necessitate further enhancements to achieve the capability of effectively delivering therapeutic molecules, including biomacromolecules, to the intended location within clinical settings ⁹⁷.

1.5. Metal-organic frameworks

Metal-organic frameworks (MOFs) have emerged as highly versatile and intriguing materials, bridging the gap between inorganic and organic chemistry ⁹⁸. These NPs are crystalline, porous structures fabricated from the assembly of metal ions or metal clusters linked by organic linkers

via coordination bonds⁹⁹. Due to their ordered porous construction and large surface-to-volume ratio, MOFs provide desirable structures that can load and release different cargo, such as medical drugs¹⁰⁰. Furthermore, considering the near-infinite types of organic and inorganic substances, the composition and structure of MOFs are highly tunable. Also, both external and internal surfaces can be functionalized independently. These properties make it possible to design MOF NPs as a platform to fulfill the specific requirements of the desired application^{101,102}.

Over the last few years, extensive research has been done into incorporating biomacromolecules within MOFs. A wide range of biomacromolecules containing enzymes¹⁰³, antibodies¹⁰⁴, and nucleic acids¹⁰⁴ have been efficiently integrated into MOF NPs. Biomacromolecule-MOF composites offer versatile applications encompassing separation processes, biocatalysis, biosensors, and biomedical endeavors. Biomacromolecules are commonly integrated into MOFs through three distinct approaches: 1) entrapment within the pores of MOFs, 2) attachment to the external surface of MOF crystals, and 3) encapsulation within MOFs through *in-situ* processes¹⁰⁵. Teplensky *et al.* used a Zr-based MOF NP (NU-1000) with a large pore size to load siRNA molecules into the pores¹⁰⁶. In another study, Hidalgo *et al.* incorporated an intact miRNA into the cages of iron (III) carboxylate MOF NPs. The miRNA-loaded MOFs successfully released the biologically active payload into the cytoplasm¹⁰⁷. Zhang *et al.* used mesoporous ZIF-8 NPs to immobilize Cyt c on their surface, leading to enhanced enzyme activity¹⁰⁸.

While entrapment into the pores and attachment to the surface have demonstrated their efficiency in biomacromolecule incorporation, these techniques still exhibit some limitations. Dimensions of the biomacromolecules are usually larger than the pore size of the MOF NPs, making it hard for post-synthetic infiltration into these cages without any alteration in their structure. Moreover, the

adsorption on the external surface of the MOF NPs may not offer sufficient protection of the biomacromolecules against environmental hazards, particularly in the context of medical applications. Additionally, the surface of MOF NPs provides less space for loading compared to their interior volume, which limits the loading efficiency. To overcome these limitations, *in situ* encapsulation has emerged as a potent method for biomacromolecule incorporation over recent years. In this approach, MOFs develop around biomacromolecules through a biomimetic mineralization process, resulting in a high loading efficiency and minimal premature leakage of the biomacromolecule ¹⁰⁹ (**Figure 1-6**). In a pioneering study, Liang *et al.* demonstrated that under physiological conditions, proteins, enzymes, and DNA promote the creation of MOFs by concentrating the framework's building blocks and facilitating crystallization around the biomacromolecules. The formed MOFs act as protective coatings, shielding biomacromolecules from severe environmental conditions ¹¹⁰. In another study, Zhang *et al.* developed biomimetic MOF NPs for the targeted delivery of siRNA coated with a cell-derived membrane. Their final

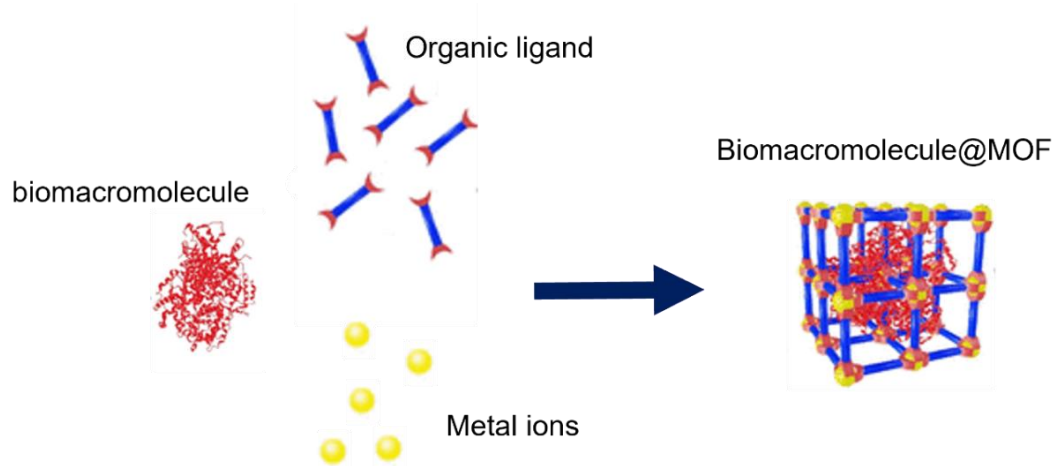


Figure 1-6. The biomineralization of metal organic frameworks around biomacromolecules. Organic ligands and metal ions assemble around biomacromolecules yielding MOF nanoparticles.

platform could successfully silence multiple gene targets and attain great control of tumor growth in breast cancer mouse models ¹¹¹. The biom mineralized Zn-based MOF NPs have also exhibited their effectiveness in encapsulating Cas9 protein in complex with the anionic sgRNA ^{42,112}.

The *in situ* encapsulation of biomacromolecules in MOFs via biom mineralization predominantly relies on zinc imidazolate framework (ZIF) materials, specifically ZIF-8 and ZIF-90, composed of zinc and imidazole derivatives ^{108,113–116}. One rationale for choosing these ZIF structures is their ability to be synthesized under mild aqueous conditions, at room temperature, and at physiological pH. Within these ZIF structures, the imidazole components become protonated at slightly acidic pH levels, which is advantageous for promoting disassembly and cargo release within endosomes and lysosomes ¹¹⁷. Nonetheless, the attribute of easy degradability may pose challenges regarding storage. Given the diverse advantages of metal-organic nanoparticles, exploring new alternatives and optimizing their synthesis conditions in a manner compatible with biomacromolecules holds significant promise as an alternative approach.

1.5.1. Iron Fumarate Nanoparticles

Iron fumarate nanoparticles (Fe-fum NPs) are a subclass of metal-organic NPs, representing a promising class of nanomaterials that have gained increasing attention due to their unique properties and potential applications in various fields. Fe-fum NPs are composed of iron ions coordinated with fumarate ligands. These nanoparticles exhibit remarkable properties arising from their composition, such as magnetic behavior ¹¹⁸, tunable sizes ¹¹⁹, and the ability to encapsulate various cargoes ^{101,102}. The controlled synthesis and modification of Fe-fum NPs have allowed their utilization in multiple fields, such as drug delivery, imaging, catalysis ¹²⁰, and environmental remediation ¹²¹.

Previously, it has been demonstrated that coated, crystalline Fe-fum NPs (MIL-88A) can store therapeutic small molecules with minimal premature leakage and release them to cancer cells efficiently ¹⁰². Nonetheless, their potential for delivering functional biomacromolecules, including proteins and RNAs, remains relatively unexplored. Fe-fum NPs usually possess a pore size in the range of 11–13 Å ¹¹⁹ which is typically smaller than the dimensions of many proteins and RNA molecules. Thus, incorporating biomacromolecules into these nanomaterials after synthesis is challenging. Addressing this limitation, the *in situ* encapsulation of biomacromolecules in Fe-fum NPs can be a promising strategy.

In the pursuit of harnessing the potential of Fe-fum NPs as useful carriers for encapsulating biomacromolecules, the primary concern is to ensure that the synthesis conditions employed are favorable for maintaining the structural and functional integrity of the delicate biomacromolecules. This requirement needs a reevaluation of the synthesis process toward a water-based condition (excluding harmful solvents), elevating the pH of the environment as close as possible to 7.4 and avoiding high temperatures. Another critical requirement in utilizing Fe-fum NPs for drug delivery is to attain small, uniformly sized particles in the 10-200 nm range to optimize their distribution within the body and cellular uptake ⁵⁴. Subsequently, upon cellular internalization, typically through endocytosis, another fundamental aspect is their effective escape from endosomes and the subsequent release of their cargo into the cytoplasm, ultimately ensuring the drug's therapeutic effectiveness.

In this PhD project, we use iron fumarate nanoparticles for intracellular delivery of biological macromolecules, including proteins and RNAs. The primary challenge was to ensure that the synthesis conditions employed are favorable for maintaining the structural and functional integrity

of the delicate biomacromolecules. In the initial experiments, reevaluation of the synthesis toward biomacromolecule-friendly synthesis conditions resulted in an increase in the size of the NPs or their agglomeration, presenting a new challenge. To control the size distribution of the NPs, we investigated and manipulated several parameters during or after the synthesis of Fe-fum NPs to obtain the desired properties.

In conclusion, we introduce a novel room-temperature synthesis method for generating Fe-fum NPs under mildly acidic aqueous conditions. Our study demonstrates the capability of forming Fe-fum NPs through biomimetic mineralization around biomacromolecules, including various model proteins and large RNA molecules, establishing an efficient platform for the delivery of such molecules while protecting them from degradation during storage, even in challenging environmental conditions.

1.6. References

1. Dammes, N. & Peer, D. Paving the Road for RNA Therapeutics. *Trends in Pharmacological Sciences* Preprint at <https://doi.org/10.1016/j.tips.2020.08.004> (2020).
2. Hopkins, A. L. & Groom, C. R. The druggable genome. *Nat Rev Drug Discov* (2002) doi:10.1038/nrd892.
3. Hopkins, A. L. Network pharmacology: The next paradigm in drug discovery. *Nature Chemical Biology* vol. 4 682–690 Preprint at <https://doi.org/10.1038/nchembio.118> (2008).
4. Tian, Y., Tirrell, M. V. & LaBelle, J. L. Harnessing the Therapeutic Potential of Biomacromolecules through Intracellular Delivery of Nucleic Acids, Peptides, and Proteins. *Advanced Healthcare Materials* vol. 11 Preprint at <https://doi.org/10.1002/adhm.202102600> (2022).
5. Luther, D. C. *et al.* Delivery of drugs, proteins, and nucleic acids using inorganic nanoparticles. *Advanced Drug Delivery Reviews* vol. 156 188–213 Preprint at <https://doi.org/10.1016/j.addr.2020.06.020> (2020).
6. Jain, M. *et al.* Introduction to Protein Therapeutics. in *Protein-based Therapeutics* (eds. Singh, D. B. & Tripathi, T.) 1–22 (Springer Nature Singapore, Singapore, 2023). doi:10.1007/978-981-19-8249-1_1.
7. Leader, B., Baca, Q. J. & Golan, D. E. Protein therapeutics: a summary and pharmacological classification. *Nat Rev Drug Discov* **7**, 21–39 (2008).

8. Jishi, A., Qi, X. & Miranda, H. C. Implications of mRNA translation dysregulation for neurological disorders. *Seminars in Cell and Developmental Biology* vol. 114 11–19 Preprint at <https://doi.org/10.1016/j.semcdb.2020.09.005> (2021).
9. Vaklavas, C., Blume, S. W. & Grizzle, W. E. Translational dysregulation in cancer: Molecular insights and potential clinical applications in biomarker development. *Frontiers in Oncology* vol. 7 Preprint at <https://doi.org/10.3389/fonc.2017.00158> (2017).
10. Le Quesne, J. P. C., Spriggs, K. A., Bushell, M. & Willis, A. E. Dysregulation of protein synthesis and disease. *Journal of Pathology* vol. 220 140–151 Preprint at <https://doi.org/10.1002/path.2627> (2010).
11. Dimitrov, D. S. Therapeutic proteins. *Methods in Molecular Biology* **899**, 1–26 (2012).
12. Keller S. Alexander *et al.* Replacement Therapies in Metabolic Disease. *Curr Pharm Biotechnol* **19**, 282–399 (2018).
13. Marchetti, M., Faggiano, S. & Mozzarelli, A. Enzyme Replacement Therapy for Genetic Disorders Associated with Enzyme Deficiency. *Curr Med Chem* **29**, 489–525 (2021).
14. Jarboe, J., Gupta, A. & Saif, W. Therapeutic human monoclonal antibodies against cancer. *Methods in Molecular Biology* **1060**, 61–77 (2014).
15. Sousa, F. *et al.* Nanoparticles for the delivery of therapeutic antibodies: Dogma or promising strategy? *Expert Opinion on Drug Delivery* vol. 14 1163–1176 Preprint at <https://doi.org/10.1080/17425247.2017.1273345> (2017).

16. Zhang, Y. *et al.* Sustained protein therapeutics enabled by self-healing nanocomposite hydrogels for non-invasive bone regeneration. *Biomater Sci* **8**, 682–693 (2020).
17. Gurevich, E. V. & Gurevich, V. V. Therapeutic potential of small molecules and engineered proteins. *Handb Exp Pharmacol* **219**, 1–12 (2014).
18. Almazroo, O. A., Miah, M. K. & Venkataramanan, R. Drug Metabolism in the Liver. *Clinics in Liver Disease* vol. 21 1–20 Preprint at <https://doi.org/10.1016/j.cld.2016.08.001> (2017).
19. Pei, J. *et al.* Targeting Lysosomal Degradation Pathways: New Strategies and Techniques for Drug Discovery. *Journal of Medicinal Chemistry* vol. 64 3493–3507 Preprint at <https://doi.org/10.1021/acs.jmedchem.0c01689> (2021).
20. Singh, R., Singh, S. & Lillard, J. W. Past, present, and future technologies for oral delivery of therapeutic proteins. *Journal of Pharmaceutical Sciences* vol. 97 2497–2523 Preprint at <https://doi.org/10.1002/jps.21183> (2008).
21. Mortimer, S. A., Kidwell, M. A. & Doudna, J. A. Insights into RNA structure and function from genome-wide studies. *Nature Reviews Genetics* Preprint at <https://doi.org/10.1038/nrg3681> (2014).
22. Tinoco, I. & Bustamante, C. How RNA folds. *J Mol Biol* (1999) doi:10.1006/jmbi.1999.3001.
23. Achar, A. & Sætrom, P. RNA motif discovery: A computational overview. *Biology Direct* vol. 10 Preprint at <https://doi.org/10.1186/s13062-015-0090-5> (2015).

24. Seetin, M. G. & Mathews, D. H. RNA structure prediction: An overview of methods. *Methods in Molecular Biology* vol. 905 99–122 Preprint at https://doi.org/10.1007/978-1-61779-949-5_8 (2012).
25. Shin, H. *et al.* Recent Advances in RNA Therapeutics and RNA Delivery Systems Based on Nanoparticles. *Advanced Therapeutics* vol. 1 Preprint at <https://doi.org/10.1002/adtp.201800065> (2018).
26. Vavilis, T. *et al.* mRNA in the Context of Protein Replacement Therapy. *Pharmaceutics* vol. 15 Preprint at <https://doi.org/10.3390/pharmaceutics15010166> (2023).
27. Han, X., Mitchell, M. J. & Nie, G. Nanomaterials for Therapeutic RNA Delivery. *Matter* Preprint at <https://doi.org/10.1016/j.matt.2020.09.020> (2020).
28. Bajan, S. & Hutvagner, G. RNA-Based Therapeutics: From Antisense Oligonucleotides to miRNAs. *Cells* Preprint at <https://doi.org/10.3390/cells9010137> (2020).
29. Castanotto, D. & Rossi, J. J. The promises and pitfalls of RNA-interference-based therapeutics. *Nature* vol. 457 426–433 Preprint at <https://doi.org/10.1038/nature07758> (2009).
30. Pascolo, S. *Vaccination with Messenger RNA (MRNA)*. www.qiagen.com.
31. Qin, S. *et al.* mRNA-based therapeutics: powerful and versatile tools to combat diseases. *Signal Transduction and Targeted Therapy* vol. 7 Preprint at <https://doi.org/10.1038/s41392-022-01007-w> (2022).

32. Kwon, H. *et al.* Emergence of synthetic mRNA: In vitro synthesis of mRNA and its applications in regenerative medicine. *Biomaterials* vol. 156 172–193 Preprint at <https://doi.org/10.1016/j.biomaterials.2017.11.034> (2018).
33. Jackson, D. A., Pombo, A. & Iborra, F. The balance sheet for transcription: an analysis of nuclear RNA metabolism in mammalian cells. *The FASEB Journal* (2000) doi:10.1096/fasebj.14.2.242.
34. Shin, H. *et al.* Recent Advances in RNA Therapeutics and RNA Delivery Systems Based on Nanoparticles. *Adv Ther (Weinh)* **1**, 1–27 (2018).
35. Whitley, J. *et al.* Development of mRNA manufacturing for vaccines and therapeutics: mRNA platform requirements and development of a scalable production process to support early phase clinical trials. *Translational Research* vol. 242 38–55 Preprint at <https://doi.org/10.1016/j.trsl.2021.11.009> (2022).
36. Verbeke, R., Lentacker, I., De Smedt, S. C. & Dewitte, H. The dawn of mRNA vaccines: The COVID-19 case. *Journal of Controlled Release* (2021) doi:10.1016/j.jconrel.2021.03.043.
37. Mellott, A. J., Forrest, M. L. & Detamore, M. S. Physical non-viral gene delivery methods for tissue engineering. *Annals of Biomedical Engineering* vol. 41 446–468 Preprint at <https://doi.org/10.1007/s10439-012-0678-1> (2013).
38. Verbeke, R., Lentacker, I., De Smedt, S. C. & Dewitte, H. Three decades of messenger RNA vaccine development. *Nano Today* Preprint at <https://doi.org/10.1016/j.nantod.2019.100766> (2019).

39. Meng, Z. *et al.* A new developing class of gene delivery: Messenger RNA-based therapeutics. *Biomaterials Science* vol. 5 2381–2392 Preprint at <https://doi.org/10.1039/c7bm00712d> (2017).
40. Sahin, U., Karikó, K. & Türeci, Ö. mRNA-based therapeutics-developing a new class of drugs. *Nature Reviews Drug Discovery* vol. 13 759–780 Preprint at <https://doi.org/10.1038/nrd4278> (2014).
41. Zhang, S., Shen, J., Li, D. & Cheng, Y. Strategies in the delivery of Cas9 ribonucleoprotein for CRISPR/Cas9 genome editing. *Theranostics* vol. 11 614–648 Preprint at <https://doi.org/10.7150/thno.47007> (2020).
42. Alsaiari, S. K. *et al.* Endosomal Escape and Delivery of CRISPR/Cas9 Genome Editing Machinery Enabled by Nanoscale Zeolitic Imidazolate Framework. *J Am Chem Soc* (2018) doi:10.1021/jacs.7b11754.
43. Mali, P. *et al.* RNA-guided human genome engineering via Cas9. *Science (1979)* (2013) doi:10.1126/science.1232033.
44. Liao, H. K. *et al.* Use of the CRISPR/Cas9 system as an intracellular defense against HIV-1 infection in human cells. *Nat Commun* (2015) doi:10.1038/ncomms7413.
45. Choudhary, E., Thakur, P., Pareek, M. & Agarwal, N. Gene silencing by CRISPR interference in mycobacteria. *Nat Commun* (2015) doi:10.1038/ncomms7267.
46. Hemphill, J., Borchardt, E. K., Brown, K., Asokan, A. & Deiters, A. Optical control of CRISPR/Cas9 gene editing. *J Am Chem Soc* (2015) doi:10.1021/ja512664v.

47. Shin, J. W. & Lee, J.-M. The prospects of CRISPR-based genome engineering in the treatment of neurodegenerative disorders. *Ther Adv Neurol Disord* (2018) doi:10.1177/1756285617741837.
48. Liu, C., Zhang, L., Liu, H. & Cheng, K. Delivery strategies of the CRISPR-Cas9 gene-editing system for therapeutic applications. *Journal of Controlled Release* vol. 266 17–26 Preprint at <https://doi.org/10.1016/j.jconrel.2017.09.012> (2017).
49. AA, D. Advantage of Delivering the Gene Therapy Tool (Cas9) as Purified Protein Formulation. *Journal of Formulation Science & Bioavailability* **01**, (2018).
50. MacHtakova, M., Thérien-Aubin, H. & Landfester, K. Polymer nano-systems for the encapsulation and delivery of active biomacromolecular therapeutic agents. *Chemical Society Reviews* vol. 51 128–152 Preprint at <https://doi.org/10.1039/d1cs00686j> (2022).
51. Damase, T. R. *et al.* The Limitless Future of RNA Therapeutics. *Frontiers in Bioengineering and Biotechnology* vol. 9 Preprint at <https://doi.org/10.3389/fbioe.2021.628137> (2021).
52. Lee, Y. W. *et al.* Protein delivery into the cell cytosol using non-viral nanocarriers. *Theranostics* vol. 9 3280–3292 Preprint at <https://doi.org/10.7150/thno.34412> (2019).
53. Huang, Y. *et al.* Elimination pathways of systemically delivered siRNA. *Molecular Therapy* **19**, 381–385 (2011).

54. Mitchell, M. J. *et al.* Engineering precision nanoparticles for drug delivery. *Nature Reviews Drug Discovery* vol. 20 101–124 Preprint at <https://doi.org/10.1038/s41573-020-0090-8> (2021).
 55. Daneman, R. & Prat, A. The blood–brain barrier. *Cold Spring Harb Perspect Biol* (2015) doi:10.1101/cshperspect.a020412.
 56. Juliano, R. L. & Carver, K. Cellular uptake and intracellular trafficking of oligonucleotides. *Advanced Drug Delivery Reviews* vol. 87 35–45 Preprint at <https://doi.org/10.1016/j.addr.2015.04.005> (2015).
 57. Doane, T. L. & Burda, C. The unique role of nanoparticles in nanomedicine: Imaging, drug delivery and therapy. *Chemical Society Reviews* Preprint at <https://doi.org/10.1039/c2cs15260f> (2012).
 58. Wu, Z. & Li, T. Nanoparticle-Mediated Cytoplasmic Delivery of Messenger RNA Vaccines: Challenges and Future Perspectives. *Pharm Res* **38**, 473–478 (2021).
 59. Zong, Y., Lin, Y., Wei, T. & Cheng, Q. Lipid Nanoparticle (LNP) Enables mRNA Delivery for Cancer Therapy. *Advanced Materials* (2023) doi:10.1002/adma.202303261.
 60. Canton, I. & Battaglia, G. Endocytosis at the nanoscale. *Chem Soc Rev* **41**, 2718–2739 (2012).
 61. Sandvig, K., Kavaliauskiene, S. & Skotland, T. Clathrin-independent endocytosis: an increasing degree of complexity. *Histochemistry and Cell Biology* vol. 150 107–118 Preprint at <https://doi.org/10.1007/s00418-018-1678-5> (2018).
-

62. Mettlen, M., Chen, P. H., Srinivasan, S., Danuser, G. & Schmid, S. L. Regulation of Clathrin-Mediated Endocytosis. *Annual Review of Biochemistry* vol. 87 871–896 Preprint at <https://doi.org/10.1146/annurev-biochem-062917-012644> (2018).
63. Huotari, J. & Helenius, A. Endosome maturation. *EMBO Journal* vol. 30 3481–3500 Preprint at <https://doi.org/10.1038/emboj.2011.286> (2011).
64. Presley, E. & Maxfield, F. R. *Sorting of Membrane Components from Endosomes and Subsequent Recycling to the Cell Surface Occurs by a Bulk Flow Process.*
65. Pei, D. & Buyanova, M. Overcoming Endosomal Entrapment in Drug Delivery. *Bioconjugate Chemistry* vol. 30 273–283 Preprint at <https://doi.org/10.1021/acs.bioconjchem.8b00778> (2019).
66. Joshi, B. S., de Beer, M. A., Giepmans, B. N. G. & Zuhorn, I. S. Endocytosis of Extracellular Vesicles and Release of Their Cargo from Endosomes. *ACS Nano* **14**, 4444–4455 (2020).
67. Wojnilowicz, M., Glab, A., Bertucci, A., Caruso, F. & Cavalieri, F. Super-resolution Imaging of Proton Sponge-Triggered Rupture of Endosomes and Cytosolic Release of Small Interfering RNA. *ACS Nano* **13**, 187–202 (2019).
68. Smith, S. A., Selby, L. I., Johnston, A. P. R. & Such, G. K. The Endosomal Escape of Nanoparticles: Toward More Efficient Cellular Delivery. *Bioconjugate Chemistry* vol. 30 263–272 Preprint at <https://doi.org/10.1021/acs.bioconjchem.8b00732> (2019).
69. Massignani, M. *et al.* Enhanced fluorescence imaging of live cells by effective cytosolic delivery of probes. *PLoS One* **5**, (2010).

70. Martens, T. F., Remaut, K., Demeester, J., De Smedt, S. C. & Braeckmans, K. Intracellular delivery of nanomaterials: How to catch endosomal escape in the act. *Nano Today* Preprint at <https://doi.org/10.1016/j.nantod.2014.04.011> (2014).
71. Varkouhi, Amir; Scholte, Marije; Storm, Gert; Haisma, H. Endosomal escape pathways for delivery of biologicals. *Journal of Controlled Release* (2010) doi:10.1016/j.jconrel.2010.11.004.
72. Byun, M. J. *et al.* Advances in Nanoparticles for Effective Delivery of RNA Therapeutics. *Biochip Journal* Preprint at <https://doi.org/10.1007/s13206-022-00052-5> (2022).
73. Kaczmarek, J. C., Kowalski, P. S. & Anderson, D. G. Advances in the delivery of RNA therapeutics: From concept to clinical reality. *Genome Medicine* vol. 9 Preprint at <https://doi.org/10.1186/s13073-017-0450-0> (2017).
74. Liang, W. & Lam, J. K. W. Endosomal Escape Pathways for Non-Viral Nucleic Acid Delivery Systems. in *Molecular Regulation of Endocytosis* (ed. Ceresa, B.) Ch. 17 (IntechOpen, Rijeka, 2012). doi:10.5772/46006.
75. Kauffman, K. J., Webber, M. J. & Anderson, D. G. Materials for non-viral intracellular delivery of messenger RNA therapeutics. *Journal of Controlled Release* **240**, 227–234 (2016).
76. Tseu, G. Y. W. & Kamaruzaman, K. A. A Review of Different Types of Liposomes and Their Advancements as a Form of Gene Therapy Treatment for Breast Cancer. *Molecules* vol. 28 Preprint at <https://doi.org/10.3390/molecules28031498> (2023).

77. Hou, X., Zaks, T., Langer, R. & Dong, Y. Lipid nanoparticles for mRNA delivery. *Nature Reviews Materials* vol. 6 1078–1094 Preprint at <https://doi.org/10.1038/s41578-021-00358-0> (2021).
78. Le Saux, S. *et al.* Nanotechnologies for Intracellular Protein Delivery: Recent Progress in Inorganic and Organic Nanocarriers. *Advanced Therapeutics* vol. 4 Preprint at <https://doi.org/10.1002/adtp.202100009> (2021).
79. Zuris, J. A. *et al.* Cationic lipid-mediated delivery of proteins enables efficient protein-based genome editing in vitro and in vivo. *Nat Biotechnol* **33**, 73–80 (2015).
80. Mirón-Barroso, S., Domènech, E. B. & Trigueros, S. Nanotechnology-based strategies to overcome current barriers in gene delivery. *International Journal of Molecular Sciences* vol. 22 Preprint at <https://doi.org/10.3390/ijms22168537> (2021).
81. Packer, M., Gyawali, D., Yerabolu, R., Schariter, J. & White, P. A novel mechanism for the loss of mRNA activity in lipid nanoparticle delivery systems. *Nat Commun* **12**, (2021).
82. Yu, M., Wu, J., Shi, J. & Farokhzad, O. C. Nanotechnology for protein delivery: Overview and perspectives. *Journal of Controlled Release* **240**, 24–37 (2016).
83. Guo, J. *et al.* Systemic delivery of therapeutic small interfering RNA using a pH-triggered amphiphilic poly-l-lysine nanocarrier to suppress prostate cancer growth in mice. *European Journal of Pharmaceutical Sciences* **45**, 521–532 (2012).
84. McCullough, Dc. *Molecular Therapy-Nucleic Acids*. www.moleculartherapy.org/mtna.

85. Ho, W. *et al.* Next-Generation Vaccines: Nanoparticle-Mediated DNA and mRNA Delivery. *Advanced Healthcare Materials* vol. 10 Preprint at <https://doi.org/10.1002/adhm.202001812> (2021).
86. Rui, Y. *et al.* Carboxylated Branched Poly(B-Amino Ester) Nanoparticles Enable Robust Cytosolic Protein Delivery and CRISPR-Cas9 Gene Editing. *Sci. Adv* vol. 5 <https://www.science.org> (2019).
87. Chang, H. *et al.* Rational Design of a Polymer with Robust Efficacy for Intracellular Protein and Peptide Delivery. *Nano Lett* **17**, 1678–1684 (2017).
88. Yang, W., Mixich, L., Boonstra, E. & Cabral, H. Polymer-Based mRNA Delivery Strategies for Advanced Therapies. *Advanced Healthcare Materials* Preprint at <https://doi.org/10.1002/adhm.202202688> (2023).
89. Insua, I., Wilkinson, A. & Fernandez-Trillo, F. Polyion complex (PIC) particles: Preparation and biomedical applications. *Eur Polym J* **81**, 198–215 (2016).
90. Tonga, G. Y., Moyano, D. F., Kim, C. S. & Rotello, V. M. Inorganic nanoparticles for therapeutic delivery: Trials, tribulations and promise. *Current Opinion in Colloid and Interface Science* vol. 19 49–55 Preprint at <https://doi.org/10.1016/j.cocis.2014.03.004> (2014).
91. Ding, Y. *et al.* Gold nanoparticles for nucleic acid delivery. *Molecular Therapy* vol. 22 1075–1083 Preprint at <https://doi.org/10.1038/mt.2014.30> (2014).

92. Jiang, Y., Huo, S., Hardie, J., Liang, X. J. & Rotello, V. M. Progress and perspective of inorganic nanoparticle-based siRNA delivery systems. *Expert Opinion on Drug Delivery* vol. 13 547–559 Preprint at <https://doi.org/10.1517/17425247.2016.1134486> (2016).
93. Mout, R. & Rotello, V. Cytosolic and Nuclear Delivery of CRISPR/Cas9-ribonucleoprotein for Gene Editing Using Arginine Functionalized Gold Nanoparticles. *Bio Protoc* **7**, (2017).
94. Remant Bahadur, K. C., Thapa, B. & Bhattarai, N. Gold nanoparticle-based gene delivery: Promises and challenges. *Nanotechnology Reviews* vol. 3 269–280 Preprint at <https://doi.org/10.1515/ntrev-2013-0026> (2014).
95. Janjua, T. I. *et al.* Silica nanoparticles: A review of their safety and current strategies to overcome biological barriers. *Adv Drug Deliv Rev* 115115 (2023) doi:10.1016/j.addr.2023.115115.
96. Tong, P. H. *et al.* Metal-organic frameworks (MOFs) as host materials for the enhanced delivery of biomacromolecular therapeutics. *Chemical Communications* Preprint at <https://doi.org/10.1039/d1cc05157a> (2021).
97. Sharma, A. R. *et al.* Recent advances of metal-based nanoparticles in nucleic acid delivery for therapeutic applications. *Journal of Nanobiotechnology* vol. 20 Preprint at <https://doi.org/10.1186/s12951-022-01650-z> (2022).
98. Horcajada, P. *et al.* Metal-organic frameworks as efficient materials for drug delivery. *Angewandte Chemie - International Edition* (2006) doi:10.1002/anie.200601878.

99. Liu, D., Zou, D., Zhu, H. & Zhang, J. Mesoporous Metal–Organic Frameworks: Synthetic Strategies and Emerging Applications. *Small* **0**, 1801454 (2018).
100. Wu, M. X. & Yang, Y. W. Metal–Organic Framework (MOF)-Based Drug/Cargo Delivery and Cancer Therapy. *Advanced Materials* Preprint at <https://doi.org/10.1002/adma.201606134> (2017).
101. Illes, B., Wuttke, S. & Engelke, H. Liposome-Coated Iron Fumarate Metal-Organic Framework Nanoparticles for Combination Therapy. *Nanomaterials* (2017) doi:10.3390/nano7110351.
102. Illes, B. *et al.* Exosome-coated metal-organic framework nanoparticles: An efficient drug delivery platform. *Chemistry of Materials* (2017) doi:10.1021/acs.chemmater.7b02358.
103. Lian, X., Erazo-Oliveras, A., Pellois, J. P. & Zhou, H. C. High efficiency and long-term intracellular activity of an enzymatic nanofactory based on metal-organic frameworks. *Nat Commun* **8**, (2017).
104. Qiu, G.-H. *et al.* Synchronous detection of ebolavirus conserved RNA sequences and ebolavirus-encoded miRNA-like fragment based on a zwitterionic copper (II) metal–organic framework. *Talanta* **180**, 396–402 (2018).
105. An, H. *et al.* Incorporation of biomolecules in Metal-Organic Frameworks for advanced applications. *Coordination Chemistry Reviews* vol. 384 90–106 Preprint at <https://doi.org/10.1016/j.ccr.2019.01.001> (2019).

106. Teplensky, M. H. *et al.* A Highly Porous Metal-Organic Framework System to Deliver Payloads for Gene Knockdown. *Chem* **5**, 2926–2941 (2019).
107. Hidalgo, T. *et al.* Biocompatible iron(iii) carboxylate metal-organic frameworks as promising RNA nanocarriers. *Nanoscale* **12**, 4839–4845 (2020).
108. Zhang, C. *et al.* Immobilization on Metal–Organic Framework Engenders High Sensitivity for Enzymatic Electrochemical Detection. *ACS Appl Mater Interfaces* **9**, 13831–13836 (2017).
109. Zou, D. *et al.* A general approach for biomimetic mineralization of MOF particles using biomolecules. *Colloids Surf B Biointerfaces* **193**, 111108 (2020).
110. Liang, K. *et al.* Biomimetic mineralization of metal-organic frameworks as protective coatings for biomacromolecules. *Nat Commun* (2015) doi:10.1038/ncomms8240.
111. Zhuang, J. *et al.* Targeted Gene Silencing in Vivo by Platelet Membrane-Coated Metal-Organic Framework Nanoparticles. *Sci. Adv* vol. 6 <https://www.science.org> (2020).
112. Yang, X. *et al.* Nanoscale ATP-Responsive Zeolitic Imidazole Framework-90 as a General Platform for Cytosolic Protein Delivery and Genome Editing. *J Am Chem Soc* (2019) doi:10.1021/jacs.8b11996.
113. Wu, X., Ge, J., Yang, C., Hou, M. & Liu, Z. Facile synthesis of multiple enzyme-containing metal–organic frameworks in a biomolecule-friendly environment. *Chemical Communications* **51**, 13408–13411 (2015).

114. Hou, C. *et al.* Facile synthesis of enzyme-embedded magnetic metal–organic frameworks as a reusable mimic multi-enzyme system: mimetic peroxidase properties and colorimetric sensor. *Nanoscale* **7**, 18770–18779 (2015).
115. Lyu, F., Zhang, Y., Zare, R. N., Ge, J. & Liu, Z. One-pot synthesis of protein-embedded metal-organic frameworks with enhanced biological activities. *Nano Lett* **14**, 5761–5765 (2014).
116. Liang, W. *et al.* Metal-Organic Framework-Based Enzyme Biocomposites. *Chemical Reviews* Preprint at <https://doi.org/10.1021/acs.chemrev.0c01029> (2021).
117. Gao, S. *et al.* Improving the Acidic Stability of Zeolitic Imidazolate Frameworks by Biofunctional Molecules. *Chem* (2019) doi:10.1016/j.chempr.2019.03.025.
118. Horcajada, P. *et al.* Porous metal-organic-framework nanoscale carriers as a potential platform for drug delivery and imaging. *Nat Mater* (2010) doi:10.1038/nmat2608.
119. Hirschle, P. *et al.* Tuning the Morphological Appearance of Iron(III) Fumarate: Impact on Material Characteristics and Biocompatibility. *Chemistry of Materials* (2020) doi:10.1021/acs.chemmater.9b03662.
120. Wang, J. *et al.* Metal-organic frameworks MIL-88A with suitable synthesis conditions and optimal dosage for effective catalytic degradation of Orange G through persulfate activation. *RSC Adv* **6**, 112502–112511 (2016).
121. Wu, H. *et al.* Arsenic removal from water by metal-organic framework MIL-88A microrods. *Environmental Science and Pollution Research* **25**, 27196–27202 (2018).
-

CHAPTER 2

Characterization

2. Characterization

2.1. Dynamic light scattering (DLS)

Dynamic Light Scattering (DLS) is a valuable technique for determining the hydrodynamic size distribution of submicron-sized particles in suspension or of polymers in solution. The technique is also called photon correlation spectroscopy (PCS) or quasi-elastic light scattering (QELS) ^{1,2}.

The principles of DLS are based on measuring the particles' Brownian motion, which is related to their thermal motion within the medium ². Brownian motion is the random movement of a particle suspended in a fluid due to collisions with molecules of the surrounding medium. This motion is influenced by both temperature and the viscosity of the medium. As the particle size gets bigger, the Brownian motion gets slower. The hydrodynamic diameter of a particle, which refers to the size of a particle that diffuses within a fluid, is related to the translational diffusion coefficient and is expressed by the Stokes-Einstein equation as follows ³:

$$R(h) = \frac{kT}{6\pi\eta D} \quad (2-1)$$

Equation 2-1. Stokes-Einstein equation; $R(h)$: hydrodynamic radius, k : Boltzmann constant, T : absolute temperature, η : viscosity of the dispersant, D : translational diffusion coefficient.

The temperature (T) and viscosity (η) of the dispersant at that temperature are known. Thus, a particle's hydrodynamic radius can be calculated from a measurement of its diffusion coefficient (D) in the dispersant.

In dynamic light scattering measurements, a monochromatic visible light ($\lambda = 633 \text{ nm}$) is focused on a diluted sample in a cuvette. When the light hits small particles, it scatters in all directions

(Rayleigh scattering). The scattering intensity fluctuates over time due to the Brownian motion of the particles in suspension. The instrument measures the rate and intensity of fluctuation and, by using a correlator, evaluates the time scale of the particle's movement and their hydrodynamic radius/diameter. A correlator is designed to measure the degree of similarity between two signals or one signal with itself at varying time intervals. If the intensity of a signal is compared with itself at a time lag of zero, the two signals will be completely correlated. As the time lag increases, the changes in the movement cause a reduction in the correlation; finally, the correlation will be zero at some point. The time lag of this deterioration in correlation is characteristic of the diffusion speed and hence the particles' size. For larger particles, the signal changes slowly, and the correlation will persist for a long time. In contrast, smaller particles move rapidly, and correlation decreases more quickly. These correlation functions are plotted versus time lag on a log scale and provide detailed information about the samples, including the mean size and mono-polydispersity of a sample ².

In this work, the DLS measurements were carried out using a Malvern Zetasizer-Nano instrument with a 4 mW He-Ne laser ($\lambda = 633 \text{ nm}$) and an avalanche photo detector.

2.2. Zeta potential

Zeta potential (also described with the Greek letter ζ) is a physical property of a particle in suspension, providing information about the external surface charge. This information can be used to optimize the particles' formulation and to confirm external modifications. Moreover, in biological studies, this information can help to predict particles' interactions with surfaces such as cell membranes or other organelles ⁴.

When a particle is dispersed in a liquid, its functional groups on the surface react with the surrounding medium, resulting in the loss of ions from the particles or adsorption of charged substances. This process results in a surface charge and subsequent accumulation of oppositely charged ions. Depending on the strength of the surface charge, a double layer of ions in the surrounding solution forms around the particle. **Figure 2-1** depicts this double layer consisting of the inner dense layer called the stern layer (ions firmly bound), and the outer slipping one called the diffuse layer (ions loosely bound) ⁵. The layers are tightly connected to the enclosed particles and follow their Brownian movement while the rest of the surrounding ions move independently of the particles ^{4,5}.

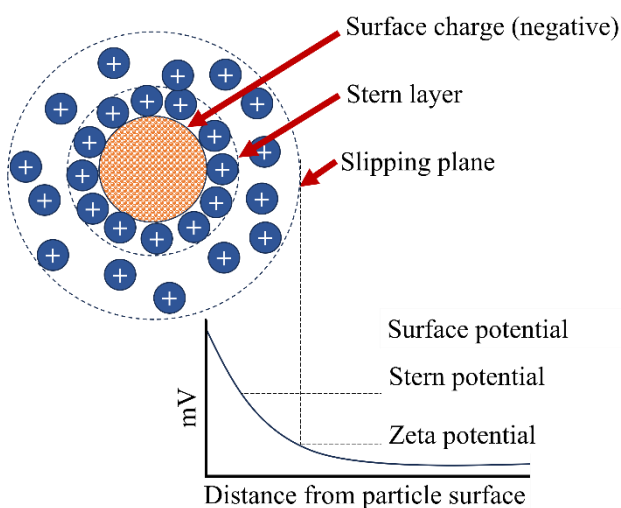


Figure 2-1. Illustration of zeta potential showing the surface charge, the Stern layer, and the slipping layer.

The zeta potential is defined as the electric potential difference between the bulk solvent and the stationary layer adhered to the dispersed particle. If the potential increases from the bulk liquid phase toward the particle's surface, the zeta potential is positive ⁶.

The Zeta Potential can be calculated by determining the particles' electrophoretic mobility (U_E). When an electric field is applied across an electrolyte, the suspended charged particles move toward the electrode of the opposite charge. The viscous forces compete with this movement. When these conflicting forces get into a balance, the movement of the particles reaches a constant velocity. Thus, the particles' velocity (electrophoretic mobility) depends on the electric field's strength, the surrounding medium's properties, including dielectric constant and viscosity, and the zeta potential of the particles ⁴. Zeta potential is related to electrophoretic mobility according to the Henry equation (**Equation 2-2**).

$$U_E = \frac{2 \varepsilon \zeta f(\kappa\alpha)}{3 \eta} \quad (2-2)$$

Equation 2-2. Henry equation. U_E : electrophoretic mobility, ε : dielectric constant of the sample, ζ : zeta potential, $f(\kappa\alpha)$: Henry function, η : viscosity of the solution.

The parameter ' κ ' in the Henry function is termed the Debye length, and the κ^{-1} is usually considered as the thickness of the electrical double layer. The parameter ' α ' states the radius of the particle. Hence, ' $\kappa\alpha$ ' is the ratio of the particle radius to the electrical double-layer thickness ⁴. For particles larger than 200 nm and a polar medium, the Henry function can be approximated to 1.5 (with the Smoluchowski model). For small particles in a non-polar medium, the Henry function is estimated to be 1.0 (with the Hückel model). With these approximations, the Zeta potential of particles can be calculated.

This work involved Zeta potential measurements with a Malvern Zetasizer Nano equipped with a 4 mW He-Ne laser ($\lambda = 633$ nm) and an avalanche photodetector.

2.3. X-ray diffraction (XRD)

X-ray diffraction (XRD) is a standard non-destructive technique that gives information about the crystallinity and structure of a material. X-ray beams are chosen in this technique since their wavelength is similar to the interatomic spacing (between 0.2 and 10 nm) in the sample ⁷.

A typical XRD instrument usually generates monochromatic X-radiation in a cathode ray tube. An electron beam is produced by heating a metal filament (the cathode) while applying a high voltage to the vacuum tube. Thereby, the electrons are accelerated towards the target anode (typically Cu, Mo, or Co). The collision of the accelerated electrons with the anode material leads to the emission of X-rays in a continuous spectrum (Bremsstrahlung) and a series of discrete X-rays. Typically, monochromatic X-rays are used in an XRD measurement, which can be achieved by applying monochromators or blocking filters ^{8,9}.

In crystalline structures, the diffracted beams experience both constructive and destructive interference. In destructive interference, diffracted beams cancel each other out. In contrast, constructive interference happens when beams with similar wavelengths are added to create a new beam with a higher amplitude ⁸. The greater amplitude converts into a larger signal for this specific diffraction angle. Then, the difference between atomic planes can be determined using Bragg's law (**Equation 2-3**), which is also represented schematically in (**Figure 2-2**) ⁹.

$$n\lambda = 2d \sin \theta \quad (2-3)$$

Equation 2-3. Bragg's law; n : order of interference, λ : wavelength of X-rays, d : lattice plane spacing, θ : angle of incidence.

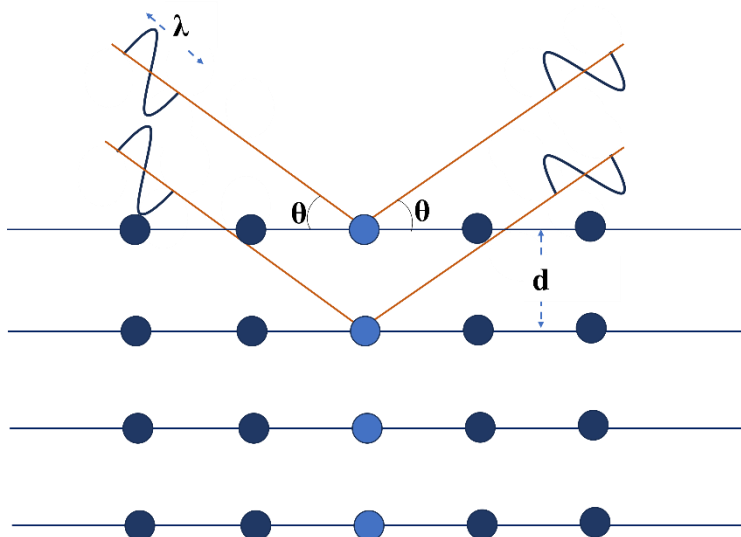


Figure 2-2. Schematic representation of the Bragg's law, illustrating the X-ray diffraction in a crystalline material.

In this thesis, X-ray diffraction of the samples was measured on a STOE Transmission-Diffractometer System STADI P with a Ge (111) primary monochromator using Cu-K α 1 radiation in transmission geometry.

2.4. Scanning Electron Microscopy (SEM)

Scanning electron microscopy (SEM) is a powerful technique to generate high-resolution images of samples by scanning the surface with a focused beam of electrons. In conventional light microscopes, visible light radiation (wavelength: 400 – 700 nm) is used to illuminate the specimen; thus, the resolution is limited to 100 nm. Radiations with shorter wavelengths interact more strongly with nanoscale materials and yield images with higher resolution¹⁰. The illumination source in electron microscopes is a highly accelerated beam of electrons with a shorter wavelength and facilitates achieving images with resolution down to less than 0.1 nm¹¹.

In a typical SEM, an electron beam is first emitted from an electron gun (electron source), which is then narrowed to a size of 0.4-5 nm using condenser lenses. The condensed electron beam, which carries significant amounts of kinetic energy, is then focused onto a spot and is scanned serially across the specimen. At each spot, the interaction with the sample causes an energy loss of the electron beam due to random scattering and absorption by the sample. The energy loss is converted to different signals, which are collected and used to form an image of specimen ¹⁰. In most of the SEMs, secondary electrons, which are low-energy electrons ejected from excited atoms, and backscattered electrons, which are reflected electrons, are used as signals for imaging the sample.

Figure 2-3 illustrates a schematic of an SEM setup ¹⁰.

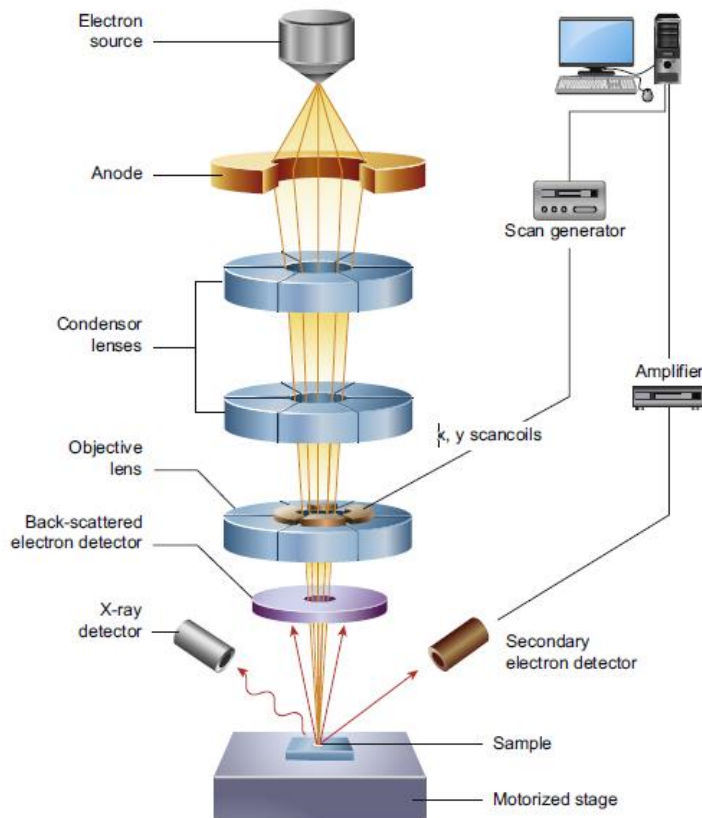


Figure 2-3. Scheme of a scanning electron microscope setup. Image reproduced from Inkson *et al.*, 2016 ¹⁰.

To acquire SEM images, it is necessary for the sample's surface to possess electrical conductivity to prevent charge accumulation. The surface of non-conductive samples is usually coated with electrically conductive materials, such as Au or C, before performing SEM.

All SEM micrographs in this thesis were recorded with a Helios NanoLab G3UC (FEI) operating at acceleration voltages between 2 and 20 kV. For sample preparation, the sample dispersion was dried overnight on a carbon film placed on an aluminum sample holder, followed by carbon sputtering before the measurement.

2.5. Molecular spectroscopy

Spectroscopy techniques are widely used to provide quantitative and qualitative information based on the interpretation of spectra resulting from the interaction of electromagnetic radiation with matter. Electromagnetic radiation can be described as mass-less particles called photons that move at the speed of light. The energy of each photon can be determined based on the frequency of the related electromagnetic wave (**Error! Reference source not found.**)¹².

$$E = h\nu = \frac{hc}{\lambda} \quad (2-4)$$

Equation 2-4. Planck equation; E : energy of a photon measured in electron volts, h : Planck's constant, ν : frequency measured in cycles per second (Hertz), c : velocity of light, λ : wavelength measured in meters.

An essential requirement for the interaction between electromagnetic radiation and a substance is that the energy of photons ($h\nu$) should match the energy difference between the internal states of the molecule (electronic, rotational, vibrational)¹³. The various spectroscopic methods differ regarding the type of interaction between radiation and matter to be monitored (such as absorption,

emission, or diffraction) and the region of the electromagnetic spectrum used in the analysis ¹². A general scheme of the electromagnetic spectrum is presented in **Figure 2-4** ¹². Methods using light in the ultra-violet, visible, or infrared region are discussed in the following.

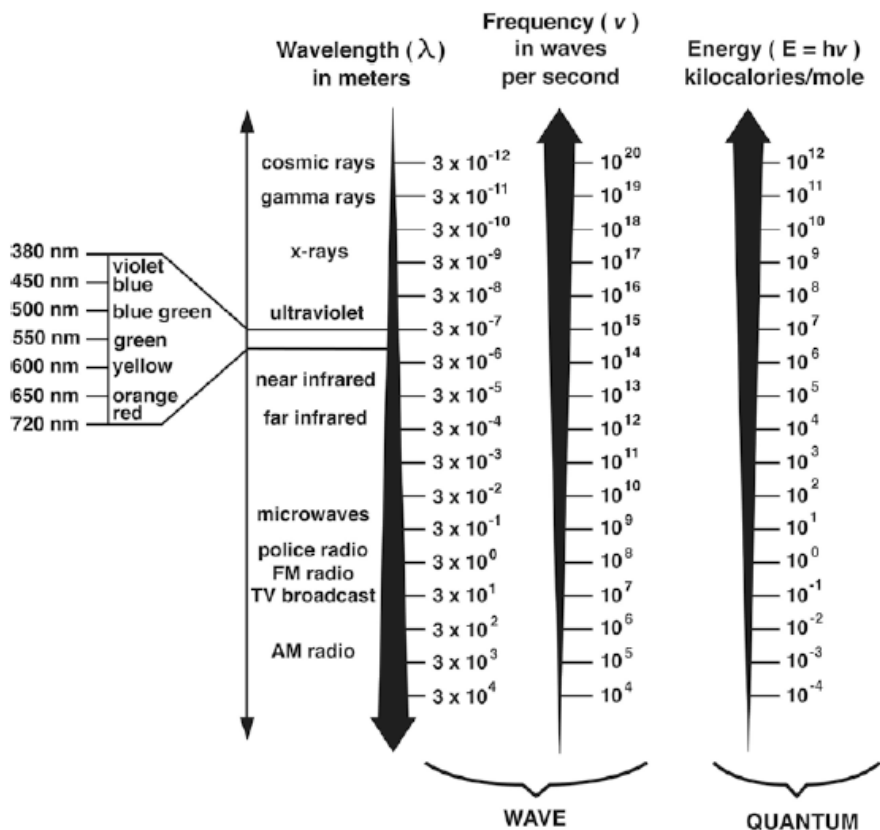


Figure 2-4. Overview of the complete electromagnetic spectrum. Image reproduced from Penner, *Basic Principles of Spectroscopy*, 2017 ¹².

2.5.1. Ultraviolet-visible (UV/VIS) spectroscopy

UV/VIS spectroscopy is used to identify, characterize, and quantify molecular compounds. This technique exploits the interaction of electromagnetic waves in the ultraviolet (200–400 nm) and visible (400–800 nm) ranges with electrons, generally valence electrons in the outer orbitals of the molecules. The absorption of light at a specific wavelength leads to the excitation of electrons to higher energy states. The energy of the absorbed photons is equal to the energy difference of the states and gives information about the electronic properties of a sample ¹⁴. Moreover, the concentration of the analyte can be quantified by the Lambert-Beer law (**Equation 2-5**).

$$A = -\log\left(\frac{I}{I_0}\right) = \varepsilon \cdot c \cdot d \quad (2-5)$$

Equation 2-1. Lambert-Beers law; *A*: Absorption, *I*: Intensity of the incident light, *I*₀: Intensity of transmitted light, ε : Molar extinction coefficient, *c*: Concentration of the analyte, *d*: Path length through the sample.

A UV/VIS spectrometer setup usually contains a light source, a monochromator, a sample compartment, and a detector (**Figure 2-5**). In this work, UV/VIS measurements were performed on a NanoDrop 2000c spectrophotometer from Thermo Fisher Scientific.

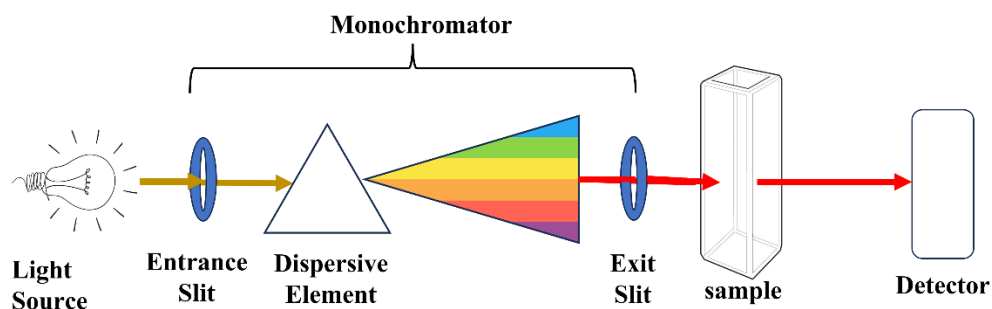


Figure 2-5. Instrumentation of a UV-VIS Spectrophotometer.

2.5.2. Infrared (IR) Spectroscopy

Infrared (IR) spectroscopy is an analytical technique to elucidate molecular structures and their functional groups based on the interaction of infrared radiation with a molecule. Due to non-invasive and rapid measurements, IR spectroscopy is a very beneficial method for characterizing proteins and analyzing various solid, liquid, and gaseous samples.

In the IR spectroscopy technique, radiation in the mid-infrared ($4000 - 400 \text{ cm}^{-1}$) is illuminated on the samples, and its effect on the vibration mode of covalent bonds is studied. After exposure to IR radiation, the molecule will absorb the radiation that matches the vibrational frequency of one (or more) of its bonds. The absorbed IR radiation increases the vibration amplitude while the frequency remains the same¹³. An interferometer is employed in IR spectroscopy to measure and produce a frequency-dependent spectrum through Fourier transformation. This spectrum acts as a fingerprint map, allowing for the identification of the vibrational bands associated with specific functional groups.

In this work, the infrared spectra of dried sample powder were recorded on a Thermo Scientific Nicolet iN10 IR microscope in absorption mode with a liquid-N₂ cooled MCT-A detector.

2.5.3. Fluorescence Spectroscopy

Fluorescence spectroscopy (also known as fluorimetry or spectrofluorometry) is a powerful analytical technique used in biomedical, medical, and chemical research. For example, in biomedical research, fluorescence spectroscopy is used to study biological molecules such as proteins, nucleic acids, and lipids. The technique allows researchers to investigate molecular

interactions, detect specific biomarkers, production or consumption of a certain molecule and explore cellular processes with exceptional sensitivity.

Fluorescence spectroscopy relies on the fundamental principle of fluorescence, a process where certain molecules, known as fluorophores, absorb light at one wavelength and subsequently emit light at a longer wavelength. The mechanism of fluorescence is based on three main steps shown by the Jablonski diagram (**Figure 2-6**)¹⁶. The process begins with the absorption of photons by the fluorophores. When these molecules are exposed to light of a specific wavelength, typically in the ultraviolet or visible range, electrons within the fluorophore absorb the energy and move from the electronic ground state (S_0) to an excited electronic state (commonly S_1 and S_2). The excited electrons may undergo internal conversion, a non-radiative process where energy is released as heat, involving transitions from higher to lower vibrational states within the same electronic state. If the vibrational levels of different electronic states overlap, internal conversion can also lead to a transition from a higher electronic state to a lower one without light emission. After vibrational relaxation to the lowest energy state, the electrons may return to their original, lower energy state (ground state) through the emission of a photon. The released photon has a longer wavelength than the absorbed photon, resulting in fluorescence emission. This emitted light is characteristic of the specific fluorophore and is typically of lower energy (longer wavelength) than the excitation light¹⁷. Another possibility is phosphorescence, which occurs when the electron transitions from the excited singlet state to a triplet state (intersystem crossing) before returning to the ground state. This transition is slower, resulting in delayed emissions.

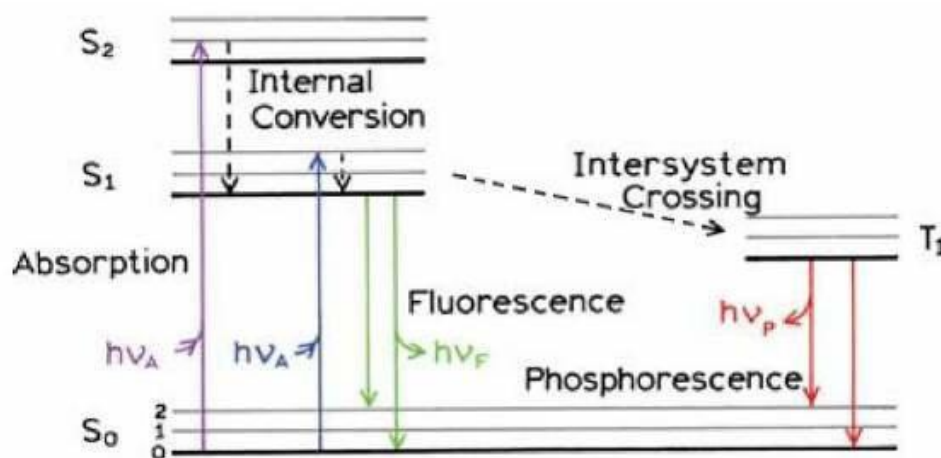


Figure 2-6. Jablonski diagram presenting the mechanism of the fluorescence process. Image reproduced from Lakowicz *et al.*, 2006¹⁶.

A typical fluorescence spectrometer consists of a radiation source like a xenon lamp, monochromators, the sample space, and subsequent photomultiplier detectors. In the end, the software converts the signal into a spectrum.

In this work, single-point fluorescence experiments were performed on a PTI spectrometer equipped with a UXL-75XE USHIO xenon short arc lamp and an 810/814 photomultiplier system. Time-based and multi-sample measurements were implemented via a SpectraFluor Plus microplate reader S4 (Tecan, Grödig, Austria).

2.6. Fluorescence Microscopy and Confocal Microscopy

2.6.1. Fluorescence Microscopy

Fluorescence microscopy is a light microscopy technique that works based on the fluorescence emission of the species. The mechanism of fluorescence has already been discussed in Chapter 2.5.3. Fluorescence microscopy is based on the excitation of a fluorophore with a specific

wavelength and the spatially resolved detection of the emitted photons on a camera system ¹⁸. Some specimens (cells or particles) are intrinsically fluorescent under ultraviolet light since they possess fluorescent substances. If the specimen does not naturally fluoresce, fluorescent markers binding to the sample can be used. Fluorescence microscopy is a powerful technique used in nanoscience to study the interaction between cells and particles. For example, the exact location of nanoparticles relative to cells can be determined by labeling the intended cellular component and nanoparticles with suitable fluorescent molecules, so-called fluorophores.

Figure 2-7 illustrates a schematic of a basic fluorescence microscope ¹⁹. Near-monochromatic and strong light sources are needed to specifically excite the intended fluorophore, not the spectrally neighbouring fluorophores ²⁰. The light passes through the excitation filter, which selects one definite wavelength for the excitation of fluorophores in the sample and removes the non-specific wavelengths. A dichroic mirror reflects the filtered excitation light toward the sample. The fluorophore in the sample absorbs the high-energy excitation ray and emits rays with lower

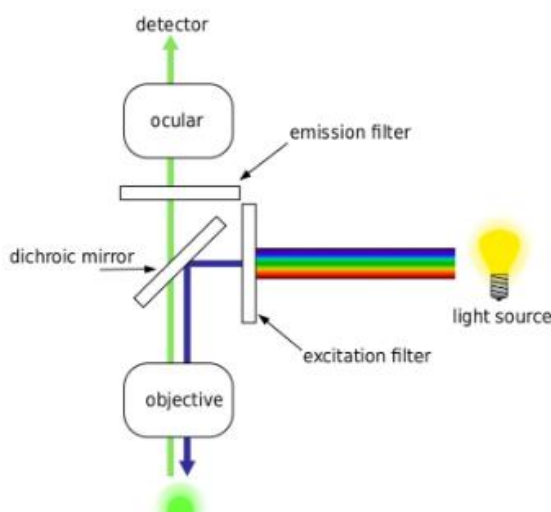


Figure 2-7. The working mechanism of a fluorescence microscope. Image reproduced from Bhakdi *et al.*, 2018 ¹⁹.

energy and longer wavelengths. By efficiently transmitting the longer-wavelength fluorescence light and reflecting the shorter-wavelength excitation light, the dichroic mirror ensures that the emitted fluorescence signals are directed toward the emission filter and detectors.

To further enhance imaging capabilities, high throughput imaging is widely employed in scientific research. This technique involves the automated and rapid acquisition of images from multiple samples, facilitating large-scale analysis and data collection. By enabling the efficient and precise handling of large datasets, high throughput imaging significantly improves the ability to conduct large-scale experiments with high precision and reproducibility. In this study, we utilized high throughput fluorescence imaging by an ImageXPress Micro XLS from Molecular Devices.

2.6.2. Confocal microscopy

Confocal microscopy creates sharp images of a specimen by a pinhole aperture, eliminating most of the light from the specimen that is not from the microscope's focal plane ²¹. **Figure 2-8** shows a schematic of a confocal microscope ²². Unlike conventional light microscopy, where the entire object field is illuminated, confocal microscopy employs an illumination pinhole to illuminate a small, round area of the object. This provides focused light on a specific position in the x, y, and z dimensions, minimizing undesired illumination and improving both contrast and focus. Additionally, a detection pinhole in front of the detector prevents light from lower and higher object planes from reaching the photomultiplier, improving image focus by reducing out-of-focus blur. The heightened resolution achieved through a narrower focus results in imaging a smaller area compared to conventional microscopy. To capture a larger area, the focus is systematically scanned across the sample. The image is assembled pixel by pixel by recording the fluorescence

intensity at each location ²⁰. The obtained image represents a thin cross-section of the specimen, which has better contrast and is less blurred than a conventional microscope image ²¹.

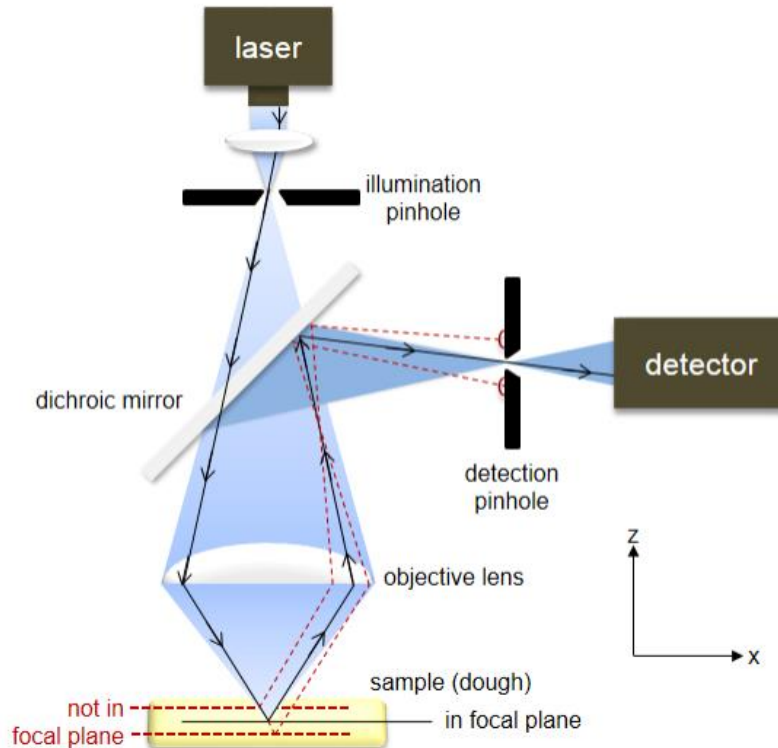


Figure 2-8. Schematic of a standard confocal microscope. The laser beam is directed to a precise region of the sample, where fluorescence is induced. The resulting fluorescent radiation is guided through a dichroic mirror to reach the detector. Any emission originating from planes either below or above the focal plane (illustrated by dashed lines) is considered out of focus, as it cannot traverse the detection pinhole and is consequently excluded from the final image. Image reproduced from Jekle *et al.*, 2015 ²⁹.

To enhance image acquisition speed, multiple scanning points are necessary instead of using a single-point scanner. For this, modern confocal microscopes often use a spinning disc containing multiple pinholes, which allow for scanning multiple spots of the sample concurrently (**Figure 2-9**). This speeds up drastically the image generation ²⁰.

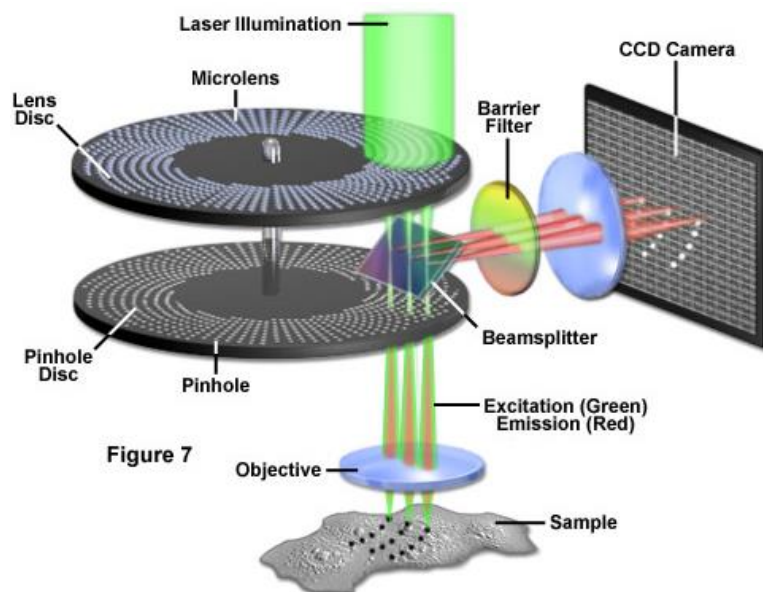


Figure 2-9. Schematic illustration of spinning disc microscope. Image reproduced from Zeiss website ³⁰.

The fluorescence microscope images in this study were taken with a Zeiss Observer SD spinning disk confocal microscope using a Yokogawa CSU-X1 spinning disc unit.

2.7. Flow cytometry (FC)

Flow cytometry (FC) is a widely used technique for simultaneously analyzing multiple physical characteristics of individual cells ²³. This technique is practical for different applications, including cell sorting within heterogeneous suspensions, cell counting, evaluating the size and volume of cells, and assessing the percentage of cells with certain fluorescent markers.

A flow cytometer contains three components: a fluidic, an optical, and an electronic unit (**Figure 2-10**). First, a cell suspension is injected into a flow cytometer chamber, surrounded by a sheath fluid. The sheath fluid hydrodynamically focuses the cell suspension through a small nozzle and

causes the cells to line up in a single-file manner. After this hydrodynamic focusing, thousands of cells are illuminated/excited individually by a laser beam(s) per second. The scattered light or the fluorescence emission is then collected, filtered, and converted to electrical signals (voltage), which are then converted to digital information by an external computer ²⁴.

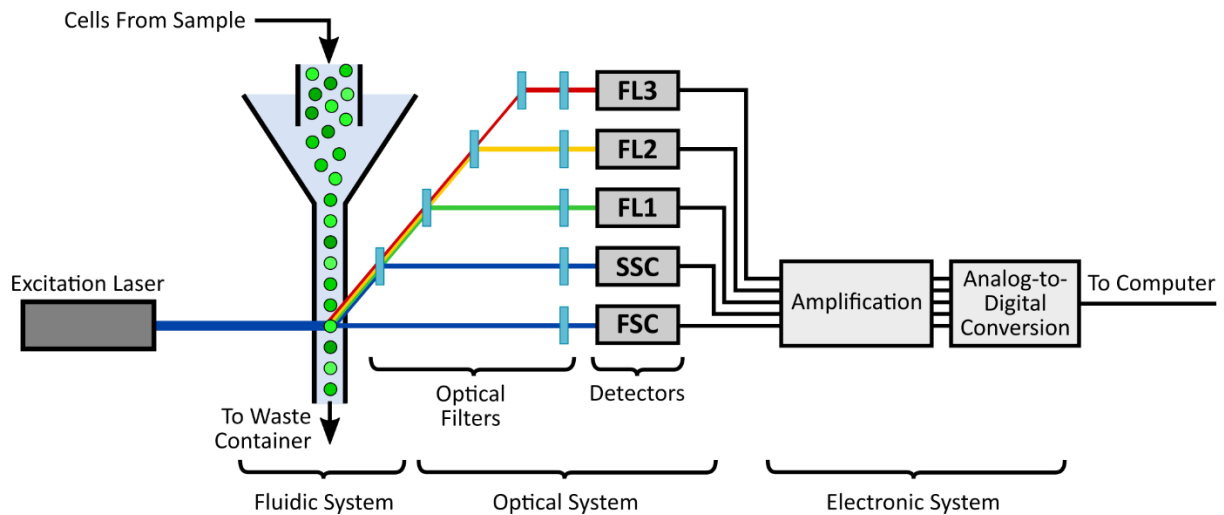


Figure 2-10. Schematic of a common flow cytometer, illustrating the fluidic, optical, and electronic systems. Image reproduced from AAT Bioquest website ³¹.

The fluorescence emission and light scattering after the interaction of the incoming light with cells give information about their properties or population ²⁵. The scattered lights are collected by a photomultiplier tube (PMT) or photodiode at two angles. The light that is scattered in up to 20 degrees offset from the laser beam axis is called a forward scatter channel (FSC) and estimates the cell's size since larger cells refract more light than smaller cells. The light measured approximately at 90 degrees angle to the incident beam axis is called a side scatter channel (SSC) and can be informative about the complexity of the cell (granularity and internal structures). Fluorescence measurements taken at different wavelengths by a flow cytometer can also provide quantitative

and qualitative data about auto-fluorescent cells, fluorescently labeled cellular organelles, and intracellular molecules such as DNA and cytokines ²⁵.

Flow cytometry measurements in this Ph.D. work are implemented by CytoFLEX S, a Beckman Coulter instrument.

2.8. Agarose gel electrophoresis

Electrophoresis through agarose gels is a standard method to separate, identify, and purify nucleic acids. The main principle of electrophoretic separation is to force the molecules to migrate through a gel by applying an electric field ²⁶. An agarose electrophoresis setup (**Figure 2-11**) mainly contains an agarose gel, an electrophoretic buffer, electrodes, and a power supply to produce the electric field ²⁶. The agarose gel is formed by heating up an agarose solution and then cooling it below 40°C, leading to hydrogen bond formation and the gel matrix creation ²⁷. The chambers in an electrophoresis system are filled by the buffer, which commonly contains EDTA and Tris-acetate (TAE) or Tris-borate (TBE), with pH 8 to 8.3 to prevent pH changes and allow for the passage of the current. The passage of the current causes the electrolysis of water at the electrodes and the formation of hydrogen gas and oxygen gas at the cathode (negative side) and anode (positive side), respectively. Under constant voltage, DNA and RNA molecules, which possess a negative charge, migrate toward the anode ²⁷. The molecules' migration in an agarose gel depends on their size and charge, as well as the pore size of the gel. The smaller molecules can pass through the gels faster than the bigger ones, and each molecule creates a band at a specific position on gel ²⁸. The original gels and nucleic acids are intrinsically colorless; thus, the presence of the formed bands can be visualized using specific fluorescent dyes that can bind to nucleic acid. Some of these staining methods use ethidium bromide, while alternatives include Life Technologies' SYBR Gold,

SYBR Green I, SYBR Green II, Biotium's GelRed, or Lonza's GelStar.²⁷ Nucleic acid stains can be introduced into the gel during its preparation or directly added to the nucleic acid samples before electrophoresis. Following electrophoresis, the stained nucleic acid bands formed within the gel can be visualized by exposing the gel to ultraviolet light at a wavelength of 245 nm²⁸.

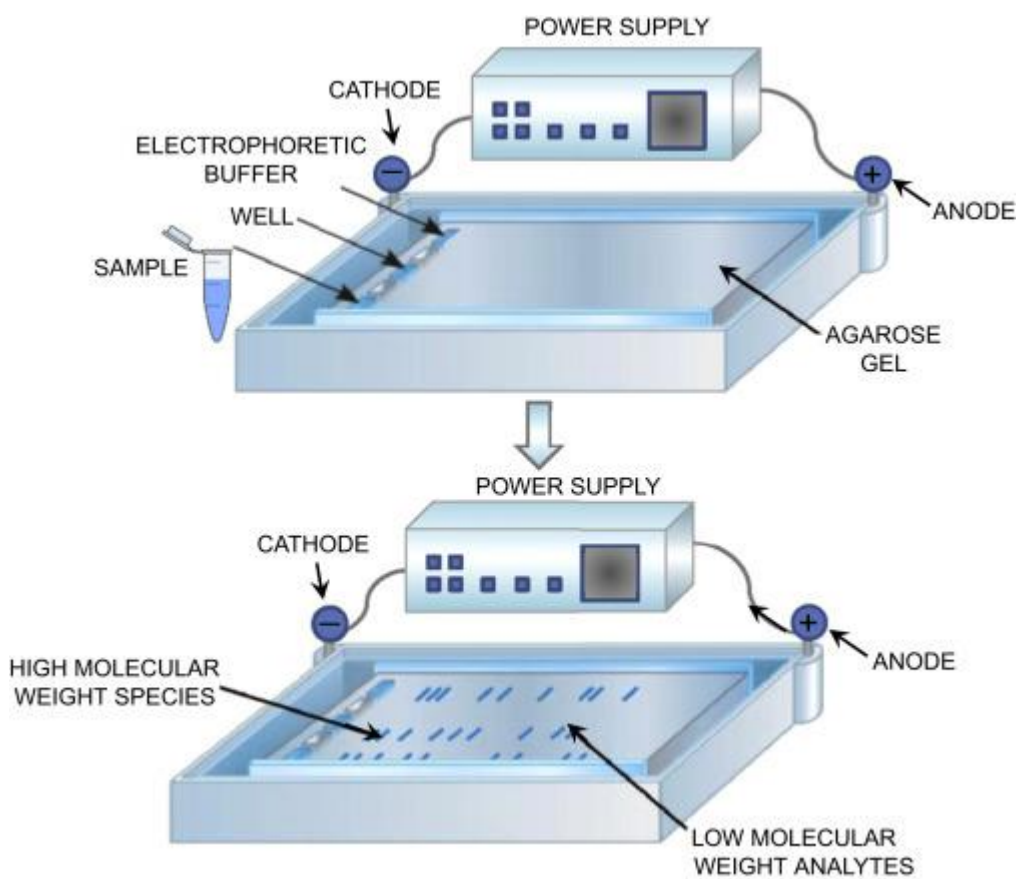


Figure 2-11. Horizontal agarose gel electrophoresis set up. Image reproduced from Drabik *et al.*, 2016²⁶.

2.9. References

1. Pecora, R. Dynamic light scattering measurement of nanometer particles in liquids. *Journal of Nanoparticle Research* (2000) doi:10.1023/A:1010067107182.
2. Malvern & Instruments, M. *Dynamic Light Scattering : An Introduction in 30 Minutes*. Technical Note MRK656-01 (2011).
3. Bhattacharjee, S. DLS and zeta potential - What they are and what they are not? *Journal of Controlled Release* Preprint at <https://doi.org/10.1016/j.jconrel.2016.06.017> (2016).
4. Malvern Instruments. *Zeta potential: An Introduction in 30 minutes*. Zetasizer Nano Serles Technical Note. MRK654-01 (2011).
5. Shnoudeh, A. J. et al. *Synthesis, Characterization, and Applications of Metal Nanoparticles*. in *Biomaterials and Bionanotechnology* (2019). doi:10.1016/B978-0-12-814427-5.00015-9.
6. McNaught, A. D. & Wilkinson, A. IUPAC. *Compendium of Chemical Terminology*, 2nd Ed. (the 'Gold Book'). IUPAC Compendium of Chemical Terminology (1997).
7. Giannini, C. et al. *X-ray Diffraction: A powerful technique for the multiple-length-scale structural analysis of nanomaterials*. *Crystals* Preprint at <https://doi.org/10.3390/cryst6080087> (2016).
8. Kazantsev, R. & Towles, M. *X-ray Crystallography - Chemistry LibreTexts*. *Chemistry LibreTexts* Preprint at (2017).

9. Stanjek, H. & Häusler, W. Basics of X-ray diffraction. *Hyperfine Interact* (2004) doi:10.1023/B:HYPE.0000032028.60546.38.
10. Inkson, B. J. Scanning Electron Microscopy (SEM) and Transmission Electron Microscopy (TEM) for Materials Characterization. in *Materials Characterization Using Nondestructive Evaluation (NDE) Methods* (2016). doi:10.1016/B978-0-08-100040-3.00002-X.
11. Butt, H., Graf, K. & Kappl, M. *Physics and Chemistry of Interfaces*. *Physics and Chemistry of Interfaces* (2003). doi:10.1002/3527602313.
12. Penner, M. H. *Basic Principles of Spectroscopy*. in (2017). doi:10.1007/978-3-319-45776-5_6.
13. Beć, K. B., Grabska, J. & Huck, C. W. Biomolecular and bioanalytical applications of infrared spectroscopy – A review. *Analytica Chimica Acta* Preprint at <https://doi.org/10.1016/j.aca.2020.04.015> (2020).
14. Fleming, I. & Williams, D. *Spectroscopic Methods in Organic Chemistry*. *Spectroscopic Methods in Organic Chemistry* (2019). doi:10.1007/978-3-030-18252-6.
15. Theophanides, T. Introduction to Infrared Spectroscopy. in *Infrared Spectroscopy - Materials Science, Engineering and Technology* (2012). doi:10.5772/49106.
16. Lakowicz, J. R. *Principles of Fluorescence Spectroscopy*. *Principles of Fluorescence Spectroscopy* (2006). doi:10.1007/978-0-387-46312-4.
17. Sauer, M., Hofkens, J. & Enderlein, J. *Basic Principles of Fluorescence Spectroscopy*. in *Handbook of Fluorescence Spectroscopy and Imaging* (2011). doi:10.1002/9783527633500.ch1.

18. Dunst, S. & Tomancak, P. Imaging flies by fluorescence microscopy: Principles, technologies, and applications. *Genetics* (2019) doi:10.1534/genetics.118.300227.
19. Bhakdi, S. C. & Thaicharoen, P. Easy employment and crosstalk-free detection of seven fluorophores in a widefield fluorescence microscope. *Methods Protoc* (2018) doi:10.3390/mps1020020.
20. Sanderson, M. J., Smith, I., Parker, I. & Bootman, M. D. Fluorescence microscopy. *Cold Spring Harb Protoc* (2014) doi:10.1101/pdb.top071795.
21. Rai, V. & Dey, N. The Basics of Confocal Microscopy. in *Laser Scanning, Theory and Applications* (2011). doi:10.5772/16214.
22. Fukuda, D. et al. Confocal Microscopy Imaging with an Optical Transition Edge Sensor. *J Low Temp Phys* (2018) doi:10.1007/s10909-018-1938-8.
23. Marti, G. E., Stetler-Stevenson, M., Bleesing, J. J. H. & Fleisher, T. A. Introduction to flow cytometry. *Seminars in Hematology* Preprint at [https://doi.org/10.1016/S0037-1963\(01\)90043-5](https://doi.org/10.1016/S0037-1963(01)90043-5) (2001).
24. Weaver, J. L. Introduction to flow cytometry. *Methods* Preprint at <https://doi.org/10.1006/meth.2000.1000> (2000).
25. Bio-Rad Laboratories Inc. *Flow Cytometry - Basics Guide*. Bio-Rad Laboratories Inc (2015).

26. Drabik, A., Bodzoń-Kułakowska, A. & Silberring, J. Gel Electrophoresis. in *Proteomic Profiling and Analytical Chemistry: The Crossroads: Second Edition* (2016). doi:10.1016/B978-0-444-63688-1.00007-0.
27. Armstrong, J. A. & Schulz, J. R. Agarose gel electrophoresis. *Current Protocols in Essential Laboratory Techniques* (2015) doi:10.1002/9780470089941.et0702s10.
28. Cai, Y. Analysis on gel electrophoresis in biology. in *E3S Web of Conferences* (2020). doi:10.1051/e3sconf/202014501009.
29. Jekle, M. & Becker, T. Wheat Dough Microstructure: The Relation Between Visual Structure and Mechanical Behavior. *Crit Rev Food Sci Nutr* 55, 369–382 (2015).
30. Zeiss, Spinning disk microscopy schematic. [Online]. Available: <https://zeiss-campus.magnet.fsu.edu/tutorials/spinningdisk/yokogawa/indexflash.html>. Accessed: May 1, 2024.
31. AAT Bioquest, Fundamentals of flow cytometry. [Online]. Available: <https://www.aatbio.com/resources/assaywise/2019-8-1/fundamentals-of-flow-cytometry>. Accessed: May 1, 2024.

CHAPTER 3

Control of Aggregation and Degradation
of Iron-Fumarate Nanoparticles
for Protein Encapsulation
and Intracellular Delivery

3. Control of aggregation and degradation of iron fumarate nanoparticles for protein encapsulation and intracellular delivery

Abstract

The enormous potential and continuously growing portfolio of protein-based applications in biotechnology and biomedicine increases the demand for techniques to deliver proteins into cells. Hybrid metal-organic nanoparticles are a promising avenue for such protein delivery systems since they can encapsulate, protect, and deliver their cargo. Biomimetic mineralization of the nanoparticles around the proteins allows for the accommodation of large proteins if performed under protein-preserving synthesis conditions. Adaptation of synthesis protocols to protein-preserving conditions requires a careful analysis of particle size, agglomeration, and degradation in order to achieve cellular uptake of the nanoparticles and release of their cargo into the cytosol. Here, we report on the influence of synthesis conditions, solvents, modulators, and coatings on the size, aggregation, and degradation of iron-fumarate nanoparticles synthesized via a protein-preserving biomimetic mineralization technique. We find conditions that allow for colloidally stable iron-fumarate nanoparticles, which incorporate proteins and are readily internalized by cells. Further, we can induce the release of their cargo into the cytosol with glucose shock. Thus, the resulting synthesis conditions render iron-fumarate nanoparticles a promising means for protein delivery into cells.

3.1. Introduction

Hybrid metal-organic nanoparticles show great potential for applications in biomedicine due to their tunability, their unique properties depending on the particular metal and organic building blocks, and their ability to encapsulate and protect various cargoes¹⁻³. Crystalline metal-organic framework nanoparticles (MOF) have, therefore, been used for drug delivery⁴, bio-imaging⁵, and even as an inherent pyroptosis-inducer without the addition of drugs as cargo⁶. The small pore size limits post-synthetic loading to small drugs that fit into the pores. To overcome this limitation and facilitate MOF-mediated delivery of large biomolecules, such as proteins, a biomimetic mineralization technique has been introduced. This technique encapsulates the desired biomolecular cargo by synthesizing the nanoparticle around the cargo⁷. To this end, MOF synthesis had to be re-evaluated to avoid potentially toxic solvents, degrading pH values, high temperatures, and other protein-degrading conditions. This led to applications using mostly ZIF-8, which can be synthesized under protein-preserving conditions⁷⁻⁹. Also, a few other MOF structures with synthesis protocols that were or could be adapted to be protein-preserving were used¹⁰⁻¹². Here, we develop the synthesis of iron-fumarate nanoparticles (Fe-fum) based on the concept of biomimetic mineralization under protein-preserving conditions for the delivery of proteins to cells. The particles are the amorphous counterpart of MIL-88A, which has been shown to facilitate the delivery of small molecules into cells¹³. The amorphous character of Fe-fums allows them to incorporate proteins at comparatively high loading efficiencies.

For the successful application of nanoparticles in protein delivery, the nanoparticles have to be colloiddally stable and exhibit a size of several 10-100 nm^{14, 15}. Additionally, after cellular uptake, they should degrade readily in the endolysosome and facilitate the endosomal release of the

transported protein ¹⁶. Thus, a detailed understanding and control of synthesis parameters that influence size, aggregation, and degradation is essential for such applications and needs to be re-evaluated after the adaptation of synthesis protocols to protein-preserving conditions ¹⁷.

Here, we show a careful analysis of a range of synthesis conditions on Fe-fum size, aggregation, and degradation. This understanding enables us to find conditions that lead to Fe-fums that are colloiddally stable, have a size suitable for cellular uptake, and allow us to trigger the endosomal release of the protein cargo with a glucose shock.

3.2. Results

3.2.1. Size control

Synthesis of Fe-fum particles was performed by the addition of iron ions into an aqueous fumaric acid solution at pH 4.8. The pH was optimized to preserve proteins and, at the same time, allow for the reaction of fumaric acid with the iron ions. Simultaneous introduction of iron ions into the fumaric acid solution at this pH resulted in large particles with sizes in the micrometer range with a high polydispersity index (PDI) as measured by Dynamic Light Scattering (DLS). This occurrence could stem from particle aggregation or continuous growth, rendering the particles unsuitable for drug delivery applications in either case.

The gradual addition of reactants under continuous stirring ensures a uniform distribution of reactants and better homogeneity in the reaction mixture. Moreover, slower addition can provide more time for nucleation to occur in a controlled manner and reduce the chance of uncontrolled aggregation. Consequently, this approach can yield smaller and more uniformly sized nanoparticles ^{18,19}.

Therefore, we adopted a gradual, stepwise approach to introducing the iron and assessed its potential in effectively regulating the size of the resulting Fe-fum NPs. Two strategies were applied for adding the same amount of iron to the fumaric acid solution: the first one was to add iron in twenty steps and 5-second intervals, and the second one was to add it in 5 steps at 20-second intervals. The size of the obtained NPs was compared via DLS measurements. The results are displayed in **Figure 3-1a**, which shows that the stepwise addition of iron was able to reduce the size of Fe-fum to the nanoscale. There was no noticeable difference with respect to particle size

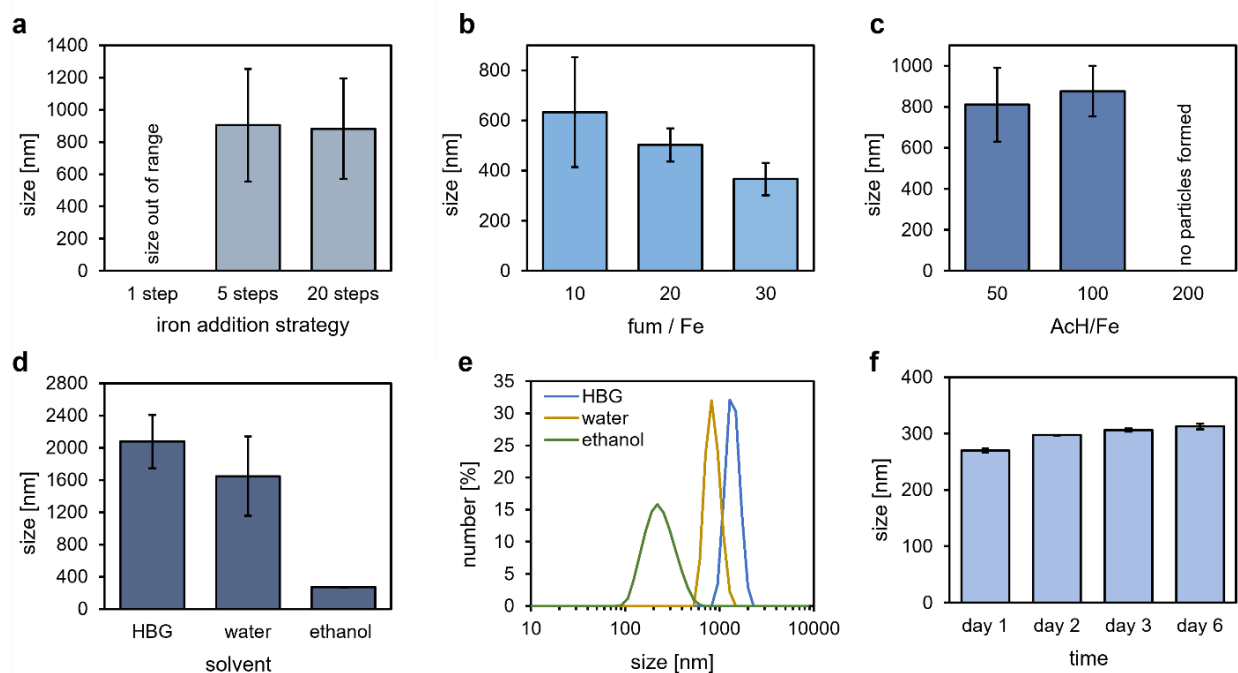


Figure 3-1. Influence of synthesis parameters on the size and stability of iron fumarate nanoparticles (Fe-fum NPs). (a) The impact of different strategies for iron addition on the size of Fe-fum NPs. (b) Effect of fumaric acid to iron molar ratios on the size of Fe-fum NPs. (c) The size of the Fe-fum NPs synthesized in the presence of acetic acid as a modulator. (d) and (e) The size and size distribution of NPs after being washed with different reagents. (f) The average size of the redispersed Fe-fum NPs in ethanol over time, demonstrating the stability of the size.

between the two strategies of stepwise addition. Thus, to minimize handling efforts, we continued the synthesis with the 5-step addition.

While the stepwise iron addition effectively reduced particle size to the nanometer range, it was still too large for applications in drug delivery. We, therefore, tested alternative methods to reduce size. Another important parameter in the formation process of metal-organic nanoparticles is the ratio of linker and metal ion^{20,21}. More linker molecules will reduce size and aggregation, but also synthesis yield²². To study the influence of the ratio of fumaric acid to iron on Fe-fum size, we increased the molar ratio of fumaric acid to iron from 10 to 20 and 30. DLS measurements of the resulting particles are shown in **Figure 3-1b** and reveal a decrease in particle size with an increasing ratio of fumaric acid to iron. However, the synthesis yield was strongly reduced at a molar ratio of 30, and the particle size was still too large for drug delivery applications. Therefore, the molar ratio of 10 was maintained, and other approaches for size control were tested.

The use of modulators and additives is a well-known method to control the size, morphology, and agglomeration of metal-organic nanoparticles²³. Modulators can be categorized into two types: deprotonated and coordinated. Deprotonated modulators accelerate nanoparticle formation by facilitating the attachment of linkers to metallic clusters through linker molecule deprotonation. Conversely, coordinated modulators hinder particle growth by competing with organic linkers²⁴. In this study, two monocarboxylic acids, formic acid, and acetic acid, were employed as coordinated modulators to control the growth of Fe-fum nanoparticles. These molecules can bind unoccupied coordination sites of the iron, leading to the consumption of these vacant sites, and thus, they compete with fumaric acid for these coordination sites. This terminates the growth

process²⁵. Ghalati *et al.* controlled the particle size of iron fumarate nanoparticles successfully with acetic acid as a modulator²⁶.

To comprehensively evaluate the impact of the modulator on the generation of Fe-fum nanoparticles, uniform conditions were maintained for the synthesis process, including consistent temperature, reaction time, and initial concentration of reactants. The ratio of fumaric acid to iron was kept at 10, and the modulator was added in increasing amounts. Formic acid was added up to a ratio of 150 compared to iron ions, and acetic acid was added up to a ratio of 200. In both cases, the highest ratio led to a decrease in particle size to the desired size as measured by DLS. However, at the same time, the amounts of modulator that decreased the particle size sufficiently also reduced the yield of the reaction strongly and, more importantly, decreased the pH of the reaction solution to values that are degrading proteins.

To maintain the pH at 4.8, we therefore used acetate buffer at pH 4.8 to introduce acetic acid into the reaction. We tested molar ratios of acetic acid to iron ions of 50, 100, and 200. As shown in **Figure 3-1c**, the lower ratios of 50 and 100 did not change the particle size measured via DLS, and the highest ratio of 200 caused inhibition of Fe-fum formation. Thus, the two mono-carboxylic acids investigated here did not yield effective size control of Fe-fum nanoparticles synthesized via the protein-preserving protocol at pH 4.8.

Another strategy to control the size of nanoparticles is to prevent their agglomeration after synthesis. Choosing an appropriate reagent for washing and dispersing the nanoparticles can enhance the uniformity of particle size distribution by effectively moderating the occurrence of agglomeration²⁷. Scanning electron microscopy (SEM) images (**Figure S 3-1**) of Fe-fum

synthesized, as described above, show that the particles have the desired physical size. Thus, the large sizes measured via DLS most likely stem from agglomeration and may be controlled by choosing the appropriate solvent. We, therefore, tested whether dispersing the particles after synthesis in HBG buffer (a buffer containing glucose) or ethanol instead of water affects the particle size distribution as measured by DLS. The resulting particle sizes are displayed in **Figure 3-1d**, and number-based size distributions are in **Figure 3-1e**. They suggest that Fe-fum exhibits signs of agglomeration in water and HBG buffer with large mean sizes and PDI values. In ethanol, they show the desired size distribution with low PDI values and a mean size of approximately 250 nm. Moreover, the size distribution of Fe-fum in ethanol was stable over a duration of six days with only a minimal increase in average size and consistently low PDI values (**Figure 3-1f**). Ethanol has been used to stabilize the size of MOF nanoparticles formed via microfluidics ²⁸. According to our experiments, it also stabilizes the size of Fe-fum nanoparticles and can be used for storage of Fe-fums.

While ethanol has been proven to stabilize the size of Fe-fum, preventing their agglomeration, it may serve storage purposes but needs to be removed for the application of the nanoparticles to cells or animals. Liposome coatings are able to facilitate cellular uptake of metal-organic nanoparticles, and as a surface coating of nanoparticles, they may modify the surface properties of the nanoparticles to reduce their mutual attraction and thus their agglomeration ^{27,29}. Three strategies for stabilizing the size of Fe-fum with liposomes were tested. The first strategy employed an *in-situ* particle formation in liposomes as nanoreactors. To this end, lipids (1,2-dioleoyl-sn-glycero-3-phosphocholine, DOPC) were dissolved in fumaric acid, iron was added, and the mixture was extruded at alkaline pH to prevent particle formation and obtain liposomes filled with

iron and fumaric acid. Particle formation was then supposedly triggered by a reduction of the pH. However, the addition of iron to the mixture of lipids and fumaric acid led to the formation of aggregates and blocked extrusion. Therefore, a second coating method was tested based on the addition of the liposomes to the reaction mixture of Fe-fum during synthesis. However, while the DLS results displayed a promising size distribution, SEM images reveal that no particles are formed, and the DLS most likely measures the liposome distribution (**Figure 3-2**). Finally, a third coating strategy was used employing fusion of DOPC-liposomes with Fe-fum that were stored in ethanol and centrifuged to remove the ethanol. This coating method yielded Fe-fum of an average size of approximately 250 nm and an acceptable PDI value. SEM images confirm a spherical morphology (**Figure 3-2c**). Thus, coating Fe-fum with DOPC-liposomes via fusion is a promising strategy to obtain small, mono-disperse nanoparticles that can be readily applied to cell experiments.

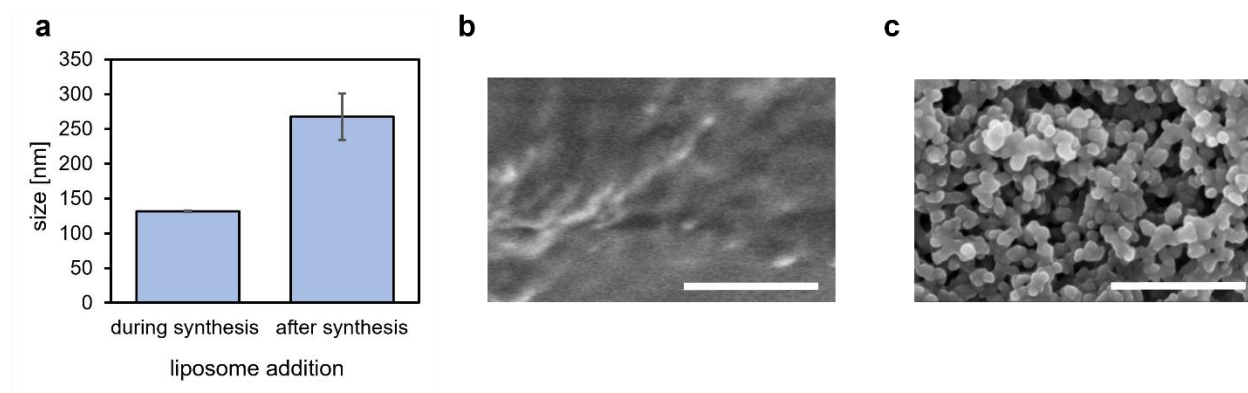


Figure 3-2. Size and morphology of iron fumarate nanoparticles (Fe₀fum NPs) with liposome addition. (a) DLS measurements indicating the size of the Fe-fum NPs with liposome added during or after synthesis. (b) and (c) SEM images illustrating the morphology of Fe-fum NPs with liposome added during and after synthesis, respectively. The scale bar is 400 nm.

3.2.2. Protein encapsulation

The experiments on size control described above were performed under protein-preserving conditions in water, at pH 4.8 and at room temperature. They did not contain proteins yet, though. To make use of the optimized synthesis under protein-preserving conditions, we next encapsulated proteins into the optimized Fe-fum. Adapting a biomimetic mineralization technique as described previously, we added bovine serum albumin labeled with fluorescein isothiocyanate (FITC-labeled BSA) as a fluorescent model protein to the fumaric acid and added iron ions according to the optimized conditions described above. Fluorescence of the obtained BSA@Fe-fum confirmed the successful incorporation of the proteins. DLS measurements and SEM images (**Figure 3-3**) indicated that the presence of BSA did not have a significant effect on the size and morphology of the Fe-fum. After liposome coating, the BSA@Fe-fum also retain their spherical morphology and exhibit an acceptable size distribution, similarly to the Fe-fum without incorporated proteins.

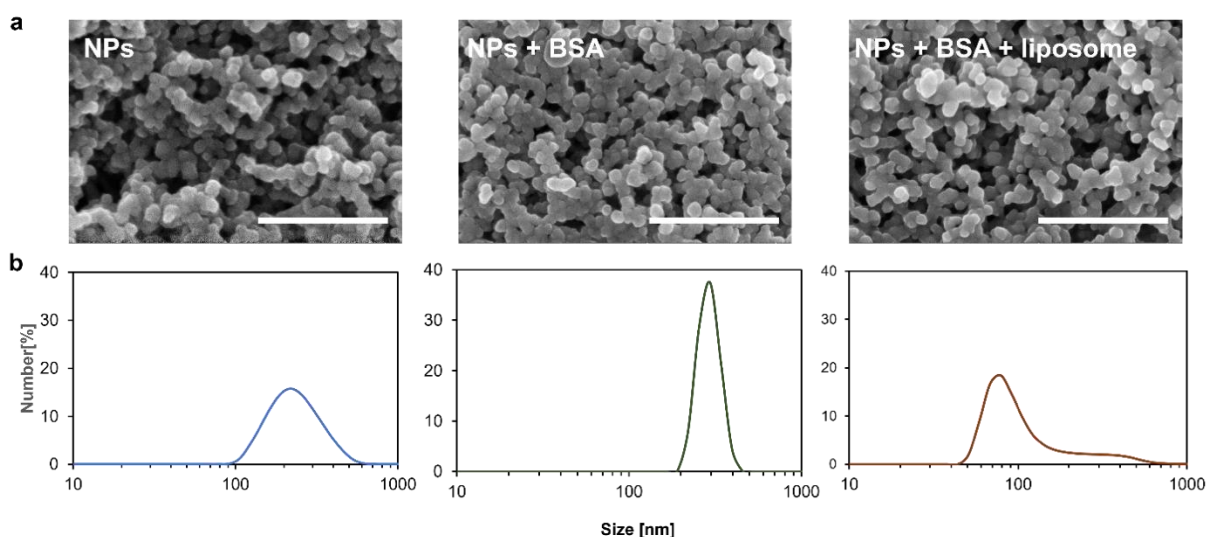


Figure 3-3. Size and morphology of Fe-fum nanoparticles with and without protein loading. (a) SEM images and (b) size distribution obtained via DLS measurements of Fe-fum NPs, BSA loaded Fe-fum, and lipid-coated BSA loaded Fe-fum. The scale bar is 400 nm.

3.2.3. Cytosolic release

In order to assess the ability of Fe-fum to deliver their cargo and release it into cells, we next incubated *HeLa* cells with lipid-coated Fe-fum loaded with calcein (as a fluorescent model for a small molecule cargo) after synthesis or lipid-coated BSA@Fe-fum (as a model for a biomacromolecular protein cargo) with FITC-BSA incorporated during the synthesis. Cellular uptake and release of the cargo were subsequently studied via fluorescence microscopy. After three days of incubation, most cells displayed green dots, which might result from Fe-fum that were taken up by the cell but did not release their cargo efficiently enough to be detected via fluorescence. This was independent of the cargo. For both cargos, we also found a few cells with a wide-spread green signal indicating successful uptake of Fe-fum and release of their cargo into the cytosol of the cells (**Figure S 3-3**). However, their number was very limited and not sufficient for applications.

Next, we therefore tested various methods to enhance the endosomal escape: acidic shock, DMSO, and hypertonic glucose shock. For simplicity, calcein release from lipid-coated, calcein-loaded Fe-fum was used as a marker for endosomal release.

Acidic shock is known to generate stress in cells, which in turn has been reported to increase endosomal escape³⁰. However, in our experiments, it induced stress in cells but no endosomal escape of the cargo (**Figure 3-4**).

The highly polar and amphiphilic solvent DMSO has been suggested to enhance membrane permeability while traversing them³¹. It has been used as an efficient trigger for endosomal escape of proteins delivered by silica nanoparticles into cells³⁰. Indeed, fluorescence microscopy of Fe-

fum incubated on *HeLa* cells revealed an elevated number of cells with calcein release after a brief incubation with 7% DMSO. After an extension of the incubation time with DMSO to 1 hour, calcein release was observed in almost all cells. The long incubation time with DMSO induced a lot of stress on cells, though, as apparent from the image in **Figure 3-4**.

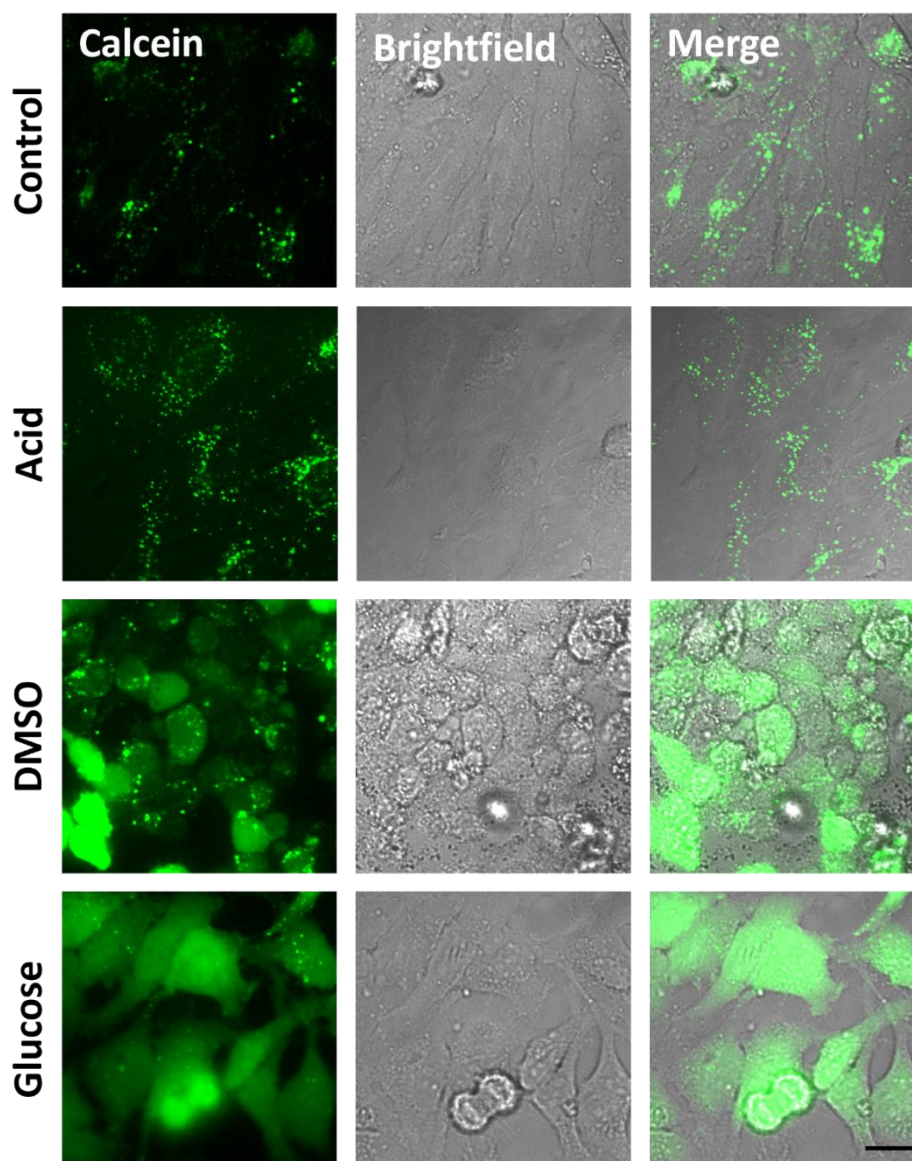


Figure 3-4. Comparison of different endosomal release triggers for calcein delivery with iron fumarate nanoparticles. Live cell confocal images of intracellular calcein delivery in non-treated (control), acid, DMSO, and hypertonic glucose-treated *HeLa* cells. Scale bar is 10 μm .

The third extracellular trigger for endosomal release that we studied was the application of a hypertonic solution of glucose. The proposed mechanism is that glucose induces an alteration of the intracellular osmotic pressure, which in turn destabilizes the endosomal membrane, facilitating the escape of the entrapped cargo from the endosome³². In our study, brief exposure of *HeLa* cells to a 1 M glucose solution efficiently promotes the release of calcein delivered via Fe-fum from endosomes in most of the cells. The glucose shock resulted in cellular shrinkage, yet subsequent removal of glucose and replacement with fresh medium mediated the recovery of cells (**Figure 3-4**). Thus, of all three tested strategies, glucose shock was the most effective in inducing endosomal release while generating the least stress on the cells.

Glucose shock as an external release trigger allows for very good temporal control of the release, which is an advantage in certain biochemical and biotechnological settings. However, in many cases, especially in settings that target therapeutic applications, an external trigger is not suitable. Hence, we next investigated options to trigger release with an internal, on-board trigger that is loaded into the Fe-fum. Since the crystalline version of Fe-fum, MIL-88A nanoparticles, degrade in the endolysosome and thereby induce the release of their cargo into the cytosol, overcoming endosomal entrapment^{13,29}, we reasoned that changing the degradation kinetics and efficiency of Fe-fum may increase the number of cells showing endosomal release. As a degrading agent, we used histidine, which contains an imidazole ring (with a pK_a of 6) that can interact with the iron atoms of the Fe-fum nanoparticle and thereby degrade the nanoparticle in the acidic endosome^{33,34}. Another reason why we chose histidine is that it has been discussed as an agent that facilitates endosomal escape by indirectly destabilizing the endosomal membrane³⁵.

To assess the ability of histidine to serve as an onboard trigger of endosomal escape, we collected the synthesized Fe-fum NPs via centrifugation and redispersed the pellet in histidine solutions of various concentrations (0, 10, 20, 50, and 100 mM) prior to calcein loading and liposome coating. Incubation with histidine led to partial degradation of Fe-fum. The degree of degradation correlated with the concentration of histidine. At the highest concentrations of 50 and 100 mM, degradation was too severe to allow for further experiments. The Fe-fum incubated with 10 and 20 mM histidine were loaded with calcein as a model drug and coated with liposomes. Then, they were incubated on *HeLa* cells, and the cytosolic release of calcein was measured and compared to that of Fe-fum without histidine. While loading in 10 mM histidine did not alter the release efficiency notably, 20 mM histidine led to a significant increase of cells exhibiting calcein release (Figure 3-5 and Figure S 3-4).

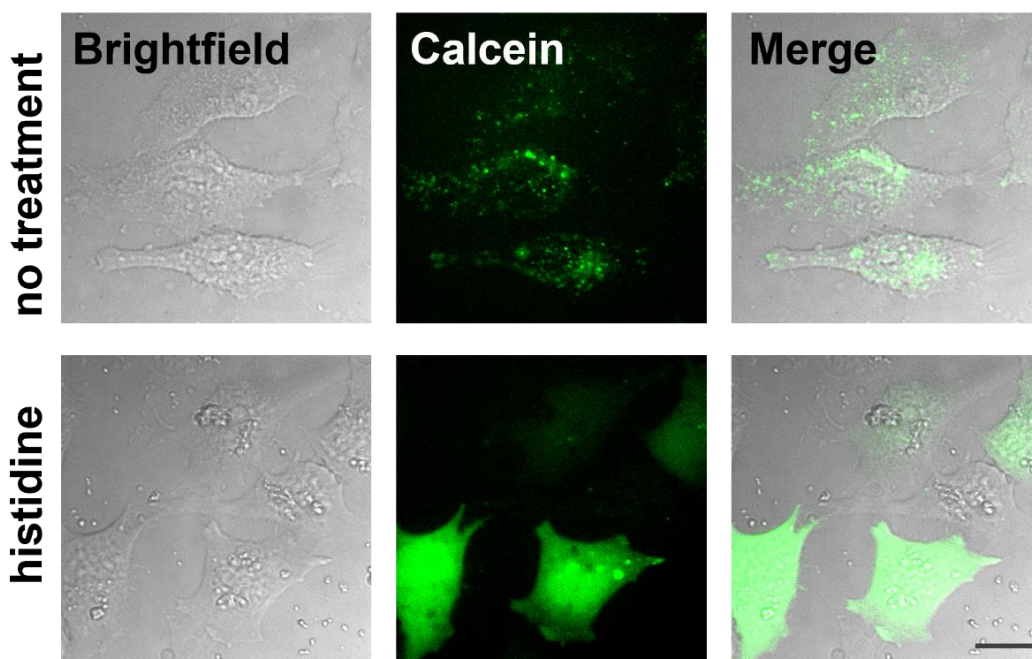


Figure 3-5. Confocal images of *HeLa* cells 3 days after treatment with calcein loaded iron fumarate nanoparticles with or without histidine loading. The scalebar is 10 μm .

Upon treatment of *HeLa* cells with concentrations of 32 and 65 $\mu\text{g}/\text{mL}$ of Fe-fum in the culture medium, we determined that approximately 4.6% and 8.9% of cells exhibited release, respectively. **(Figure S 3-5).**

Finally, we used BSA@Fe-fum to assess its potential of delivering proteins to cells. Again, we applied a glucose shock after 3d incubation of BSA@Fe-fum. Similarly to calcein-loaded Fe-fum, we did not observe significant release before glucose shock. Upon glucose shock, most cells displayed uniformly spread FITC-BSA in cells resulting from successful endosomal release **(Figure S 3-6)**. We also tested 20 mM histidine as an internal trigger for the endosomal release of BSA. However, in contrast to the endosomal release of the small molecule cargo calcein, histidine did not induce the release of BSA. Further experiments are necessary to find an internal trigger for protein release.

3.3. Conclusion

All in all, we present a detailed analysis of the influence of a variety of synthesis parameters on nanoparticle size and aggregation. We showed that stepwise synthesis at a Fe:fum ratio of 1:10 and subsequent washing and dispersion in ethanol leads to monodisperse nanoparticles at sizes suitable for intracellular delivery. Liposome coating stabilizes the size of Fe-fum in aqueous buffer to allow for cellular applications. Proteins can be readily incorporated into Fe-fum and do not significantly change the size distribution or morphology of the nanoparticles. Furthermore, lipid-coated Fe-fum are internalized by cells, and intracellular release of proteins and loaded small molecules can be triggered externally via glucose shock. Small cargo molecules can even be released from the endosome with the internal on-board trigger histidine. While an internal trigger

for the endosomal release of proteins still remains to be found in the future, Fe-fum promises the potential for applications in biochemical and biotechnological settings.

3.4. Material and methods

3.4.1. Synthesis

Chemicals

If not stated otherwise, chemicals were purchased from Sigma Aldrich (St. Louis, MO, USA).

Initial Fe-fum Synthesis

A 10 mM solution of fumaric acid in deionized water was prepared, and the pH of the solution was adjusted to 4.8 by adding NaOH (10 mM). A separate solution of iron 10 mM was prepared by dissolving $\text{FeCl}_3 \cdot 6\text{H}_2\text{O}$ in water. The iron solution was added in one step to fumaric acid at a molar ratio of 1:10 under magnetic stirring (800 rpm). After 2 minutes, the particles were collected via centrifugation (7179 RCF, 20 minutes) and redispersed in water. Centrifugation and subsequent redispersion in water were repeated three times.

Stepwise iron addition

Instead of adding the iron solution in one step to fumaric acid, a total amount of 2 mL of iron was added to 20 mL of fumaric acid either in 20 steps (20 x 100 μL , 5-second intervals) or 5 steps (5 x 400 μL , 20-second intervals). Afterward, the particles were collected and washed via three rounds of centrifugation and redispersion in water.

Molar ratio of fumaric acid to iron

While maintaining a constant volume of fumaric acid at 10 mM, we introduced varying volumes of the iron solution (10 mM), resulting in molar ratios of fumaric acid to iron of 10, 20, and 30. The total amount of iron solution in each experiment was divided and added in 5 steps and 20-second intervals. After 2 minutes, the particles were collected and washed via three rounds of centrifugation and redispersion in water.

Modulators

1) Formic acid: Different volumes (0, 22, 52, or 113 μL) of formic acid 98% were added to 20 mL of fumaric acid (10 mM), resulting in fumaric acid with 0, 0.6, 1.4, and 3 mmol of formic acid, respectively. Subsequently, 2 mL of iron solution (0.02 mmol) was added in 5 steps to each solution. After 2 minutes, the particles were centrifuged and redispersed in water three times.

2) Acetic acid: A stock of acetate buffer 3 M with pH 4.8 was prepared (14.52 g sodium acetate + 10 mL acetic acid + 100 mL water). The iron solution was introduced to the fumaric acid in a 1:10 ratio, and subsequently, varying volumes of 3M acetate buffer were added to achieve final molar ratios of acetic acid to iron at 50, 100, and 200. The obtained particles were collected via a threefold centrifugation and redispersion in water.

Washing and dispersants

Particles were synthesized in three different containers by adding iron solution in 5 steps to fumaric acid at a molar ratio of iron to fumaric acid of 1:10. After 2 minutes of incubation, the obtained particles were collected via centrifugation at 7179 RCF for 20 minutes and redispersed in water,

HBG buffer (HEPES buffered glucose solution; 20 mM HEPES, 5% glucose, pH 7.4), or ethanol. The cycles of centrifugation and redispersion in the respective solvents were repeated three times.

Liposome coating

1) Liposome coating after Fe-fum synthesis: The liposome coating solution was prepared by extruding a 1 mg/mL PBS solution of DOPC (1,2-dioleoyl-sn-glycero-3-phosphocholine, Avanti) through an extruder with a 100 nm pore-sized membrane 11 times. 1 mg of as-synthesized Fe-fum NPs were collected via centrifugation (14000 rpm, 5 minutes). The pellet of the nanoparticles was redispersed in 500 μ L of liposome solution, followed by the addition of 500 μ L of deionized water and incubation for 2 hours. The particles were then centrifuged (14000 rpm, 5 minutes) and redispersed in PBS.

2) Liposome coating during NPs' synthesis: The liposome coating solution was prepared by extruding a 1 mg/mL solution of DOPC in acetate buffer (0.1 M, pH 4.8) through an extruder with a 100 nm pore-sized membrane 11 times. 5 mL of fumaric acid (10 mM, pH 4.8) was added to a container, and subsequently, the 500 μ L of iron solution 10 mM, as well as 2 mL of the prepared liposomes, were added to the reaction under stirring at 800 rpm. After 2 minutes, the particles were collected and washed via three rounds of centrifugation and redispersion in water.

3) Liposomes as nanoreactors for NPs' formation: DOPC was dissolved in an aqueous solution of fumaric acid (10 mM) to reach a concentration of 1 mg/mL. Then, the mixture's pH was adjusted to around 8.5 to temporarily reduce the reactivity of the fumaric acid with iron molecules. 500 μ L of 10 mM iron solution was added to 5 mL of the DOPC-containing fumaric acid. The whole combination was then subjected to extrusion through a 100 nm pore-sized membrane.

Protein encapsulation

150 µg bovine serum albumin (BSA) was dissolved in 5 mL fumaric acid (10 mM, pH 4.8) and incubated for 10 minutes. Next, the 500 µL of iron solution 10 mM was added stepwise to the mixture of fumaric acid and BSA. After 2 minutes, the particles were collected and washed via three rounds of centrifugation and redispersion in ethanol.

Histidine modification

A 20 mM solution of histidine was prepared in HBG buffer (HEPES buffered glucose solution; 20 mM HEPES, 5% glucose, pH 7.4). 1 mg of Fe-fum NPs were centrifuged (14000 rpm, 5 minutes), and the pellet was redispersed in 1 mL of histidine solution and incubated for 1 hour. After 1 hour, the histidine-loaded NPs were collected via centrifugation for the subsequent calcein loading step.

Calcein loading

A 1 mM solution of calcein in deionized water was prepared. 1 mg of Fe-fum NPs (with or without histidine modification) were redispersed in 1 mL of the calcein solution. The mixture was then incubated overnight at 700 rpm, shaking for loading. Then, the nanoparticles were centrifuged for 5 min at 14000 rpm, and the supernatant was discarded to collect the Fe-fum NPs for liposome coating. Bleached calcein was employed to prevent fluorescence overlap during experiments with FITC-BSA, ensuring accurate measurement of FITC-BSA fluorescence. This approach enhances the specificity and reliability of fluorescence data in the study.

Extracellular modifications for inducing endosomal escape

HeLa cells were treated with liposome-coated and calcein-loaded Fe-fum NPs. After three days the cells were treated with three different endosomal triggers (as described below) and imaged via confocal microscopy to follow the intracellular release of calcein.

1) Acid shock: 5 μ L of HCl 1M was added to NP-treated cells (each well containing 300 μ L medium) 1 hour before imaging the cells.

2) DMSO: NP-treated cells were incubated with 7% DMSO in DMEM for 10 minutes or 1 hour before imaging the cells.

3) Glucose shock: NP-treated cells were incubated with 1M glucose in DMEM for 6 minutes. Then, the cells were washed twice with PBS to remove the glucose completely and treated with fresh DMEM.

Release efficiency

To evaluate cellular release efficiency, we employed a cell counting-based technique. For this, initially, *HeLa* cells were seeded in ibidi 8-well plates and allowed to adhere overnight. Subsequently, 10 or 20 μ g of the calcein-loaded Fe-fum NPs, with or without histidine loading, were added to the 300 μ L cell culture medium, resulting in concentrations of 32 and 65 μ L, respectively. Following three days of incubation, cells were stained with Hoechst dye to visualize cell nuclei and imaged using fluorescence microscopy. Cells exhibiting a widespread green fluorescence signal, indicative of drug release, were manually identified and counted. The release efficiency was calculated as the ratio of the number of cells with a widespread signal to the total

number of cells per image, expressed as a percentage. Between 8 to 20 images were analyzed for each condition. Statistical analysis was performed using one-way ANOVA in Excel.

3.4.2. Characterization methods

Dynamic Light Scattering (DLS)

DLS measurements were performed with a Zetasizer Nano Series (Nano-ZS, Malvern) equipped with a laser of wavelength $\lambda = 633$ nm. The measurements were performed at 25 °C and in PMMA cuvettes.

X-ray diffraction (XRD)

XRD experiments were performed with dried Fe-fum NPs. The samples were measured on a STOE Diffractometer System STADI P operating in transmission mode. The setup is using Cu $K\alpha_1$ -radiation with a wavelength $\lambda = 0.15418$ nm.

Scanning Electron microscopy (SEM)

SEM micrographs were obtained using a Helios NanoLab G3UC (FEI) operating at 5 kV. To prepare the samples, the Fe-fum NP dispersion was first dried overnight on a carbon film located on an aluminum sample holder. Subsequently, carbon sputtering was performed before conducting the measurements.

Confocal microscopy

Fluorescence microscope images were captured using a Zeiss Observer SD spinning disk confocal microscope equipped with a Yokogawa CSU-X1 spinning disc unit and a 63x oil immersion

objective (1.40 N.A.). A 488 nm laser was used for excitation, and the emission light was filtered using a BP 525/50 filter.

Cell culture

HeLa cells, a human cervical carcinoma cell line, were cultured in Dulbecco's modified Eagle's medium (DMEM, Gibco, USA) supplemented with 10% (v/v) fetal bovine serum (FBS, Gibco, USA) and 1% (v/v) penicillin-streptomycin (Gibco, USA). The cell cultures were maintained in a cell culture incubator (Hera Cell) at a temperature of 37°C with a 5% carbon dioxide atmosphere. For microscopy experiments, cells were seeded into an 8-well μ -slide (ibiTreat, ibidi GmbH).

3.5. References

1. Gao, X., Hai, X., Baigude, H., Guan, W. & Liu, Z. Fabrication of functional hollow microspheres constructed from MOF shells: Promising drug delivery systems with high loading capacity and targeted transport. *Sci Rep* 6, (2016).
2. Moharramnejad, M. et al. MOF as nanoscale drug delivery devices: Synthesis and recent progress in biomedical applications. *J Drug Deliv Sci Technol* 81, 104285 (2023).
3. Sun, Z. et al. Nanoscale MOFs in nanomedicine applications: from drug delivery to therapeutic agents. *Journal of Materials Chemistry B* vol. 11 3273–3294 Preprint at <https://doi.org/10.1039/d3tb00027c> (2023).
4. Rabiee, N. Sustainable metal-organic frameworks (MOFs) for drug delivery systems. *Mater Today Commun* 35, 106244 (2023).
5. Nguyen, N. T. T. et al. Recent progress and challenges of MOF-based nanocomposites in bioimaging, biosensing and biocarriers for drug delivery. *Nanoscale Advances* Preprint at <https://doi.org/10.1039/d3na01075a> (2024).
6. Ploetz, E. et al. Metal–Organic Framework Nanoparticles Induce Pyroptosis in Cells Controlled by the Extracellular pH. *Advanced Materials* 32, (2020).
7. Liang, K. et al. Biomimetic mineralization of metal-organic frameworks as protective coatings for biomacromolecules. *Nat Commun* (2015) doi:10.1038/ncomms8240.

8. Chen, T. T., Yi, J. T., Zhao, Y. Y. & Chu, X. Biomaterialized Metal-Organic Framework Nanoparticles Enable Intracellular Delivery and Endo-Lysosomal Release of Native Active Proteins. *J Am Chem Soc* (2018) doi:10.1021/jacs.8b04457.
9. Chen, W. H. et al. Glucose-responsive metal-organic-framework nanoparticles act as ‘smart’ sense-and-treat carriers. *ACS Nano* 12, 7538–7545 (2018).
10. Li, P. et al. Nanosizing a Metal-Organic Framework Enzyme Carrier for Accelerating Nerve Agent Hydrolysis. *ACS Nano* 10, 9174–9182 (2016).
11. Lian, X. et al. Enzyme-MOF Nanoreactor Activates Nontoxic Paracetamol for Cancer Therapy. *Angewandte Chemie* 130, 5827–5832 (2018).
12. Shieh, F.-K. et al. Imparting Functionality to Biocatalysts via Embedding Enzymes into Nanoporous Materials by a de Novo Approach: Size-Selective Sheltering of Catalase in Metal–Organic Framework Microcrystals. *J Am Chem Soc* 137, 4276–4279 (2015).
13. Illes, B. et al. Exosome-coated metal-organic framework nanoparticles: An efficient drug delivery platform. *Chemistry of Materials* (2017) doi:10.1021/acs.chemmater.7b02358.
14. Horcajada, P. et al. Metal-organic frameworks in biomedicine. *Chemical Reviews Preprint* at <https://doi.org/10.1021/cr200256v> (2012).
15. Mitchell, M. J. et al. Engineering precision nanoparticles for drug delivery. *Nature Reviews Drug Discovery* vol. 20 101–124 Preprint at <https://doi.org/10.1038/s41573-020-0090-8> (2021).
16. Yu, M., Wu, J., Shi, J. & Farokhzad, O. C. Nanotechnology for protein delivery: Overview and perspectives. *Journal of Controlled Release* 240, 24–37 (2016).

17. Ahmadi, M. et al. An investigation of affecting factors on MOF characteristics for biomedical applications: A systematic review. *Heliyon* vol. 7 Preprint at <https://doi.org/10.1016/j.heliyon.2021.e06914> (2021).
18. Shimogaki, T. et al. Morphology control of microporous silica particles obtained by gradual injection of reactants. *J Solgel Sci Technol* 76, 156–163 (2015).
19. Vreeland, E. C. et al. Enhanced Nanoparticle Size Control by Extending LaMer's Mechanism. *Chemistry of Materials* 27, 6059–6066 (2015).
20. Wang, X. G., Cheng, Q., Yu, Y. & Zhang, X. Z. Controlled Nucleation and Controlled Growth for Size Predictable Synthesis of Nanoscale Metal–Organic Frameworks (MOFs): A General and Scalable Approach. *Angewandte Chemie - International Edition* 57, 7836–7840 (2018).
21. Hidalgo, T. et al. Biocompatible iron(iii) carboxylate metal-organic frameworks as promising RNA nanocarriers. *Nanoscale* 12, 4839–4845 (2020).
22. Zhong, M. et al. Recent Progress of Nanoscale Metal–Organic Frameworks in Synthesis and Battery Applications. *Advanced Science* vol. 8 Preprint at <https://doi.org/10.1002/advs.202001980> (2021).
23. Marshall, C. R., Staudhammer, S. A. & Brozek, C. K. Size control over metal-organic framework porous nanocrystals. *Chemical Science* vol. 10 9396–9408 Preprint at <https://doi.org/10.1039/c9sc03802g> (2019).

24. Wißmann, G. et al. Modulated synthesis of Zr-fumarate MOF. *Microporous and Mesoporous Materials* 152, 64–70 (2012).
25. Bagherzadeh, E., Zebarjad, S. M. & Hosseini, H. R. M. Morphology modification of the iron fumarate MIL-88A metal–organic framework using formic acid and acetic acid as modulators. *Eur J Inorg Chem* 2018, 1909–1915 (2018).
26. Chalati, T., Horcajada, P., Gref, R., Couvreur, P. & Serre, C. Optimisation of the synthesis of MOF nanoparticles made of flexible porous iron fumarate MIL-88A. *J Mater Chem* 21, 2220–2227 (2011).
27. Shrestha, S., Wang, B. & Dutta, P. Nanoparticle processing: Understanding and controlling aggregation. *Advances in Colloid and Interface Science* vol. 279 Preprint at <https://doi.org/10.1016/j.cis.2020.102162> (2020).
28. Carraro, F. et al. Continuous-Flow Synthesis of ZIF-8 Biocomposites with Tunable Particle Size. *Angewandte Chemie - International Edition* (2020) doi:10.1002/anie.202000678.
29. Illes, B., Wuttke, S. & Engelke, H. Liposome-Coated Iron Fumarate Metal-Organic Framework Nanoparticles for Combination Therapy. *Nanomaterials* (2017) doi:10.3390/nano7110351.
30. Chiu, H. Y. et al. Intracellular chromobody delivery by mesoporous silica nanoparticles for antigen targeting and visualization in real time. *Sci Rep* 6, (2016).

31. Lin, J., Novak, B. & Moldovan, D. Molecular dynamics simulation study of the effect of DMSO on structural and permeation properties of DMPC lipid bilayers. *Journal of Physical Chemistry B* 116, 1299–1308 (2012).
32. Wang, S. & Wu, S. Endosomal explosion induced by hypertonicity. doi:10.1101/730648.
33. Chang, K. L., Higuchi, Y., Kawakami, S., Yamashita, F. & Hashida, M. Efficient gene transfection by histidine-modified chitosan through enhancement of endosomal escape. *Bioconjug Chem* 21, 1087–1095 (2010).
34. He, J., Xu, S. & James Mixson, A. The multifaceted histidine-based carriers for nucleic acid delivery: Advances and challenges. *Pharmaceutics* vol. 12 1–31 Preprint at <https://doi.org/10.3390/pharmaceutics12080774> (2020).
35. Erazo-Oliveras, A., Muthukrishnan, N., Baker, R., Wang, T. Y. & Pellois, J. P. Improving the endosomal escape of cell-penetrating peptides and their cargos: Strategies and challenges. *Pharmaceutics* vol. 5 1177–1209 Preprint at <https://doi.org/10.3390/ph5111177> (2012).

3.6. Supplementary figures

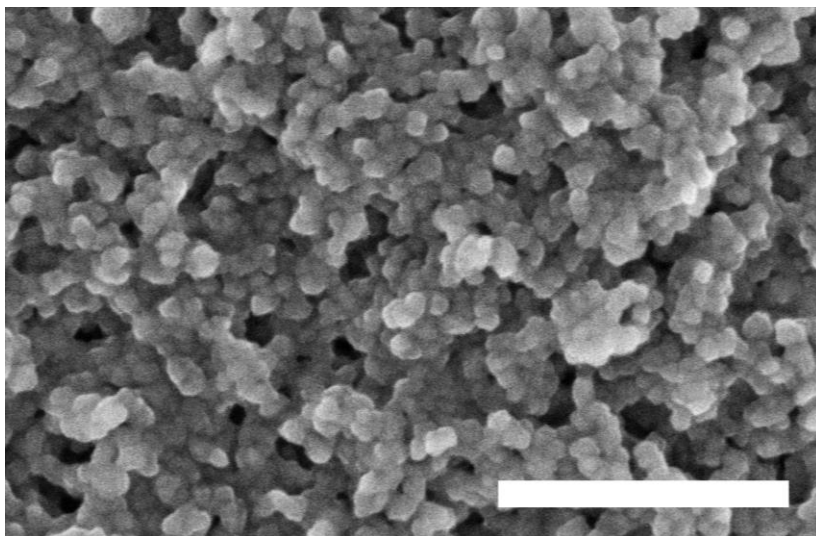


Figure S 3-1. SEM micrograph of Fe-fum NPs synthesized by 5-step iron addition and washed and redispersed in water. The scale bar is 500 nm.

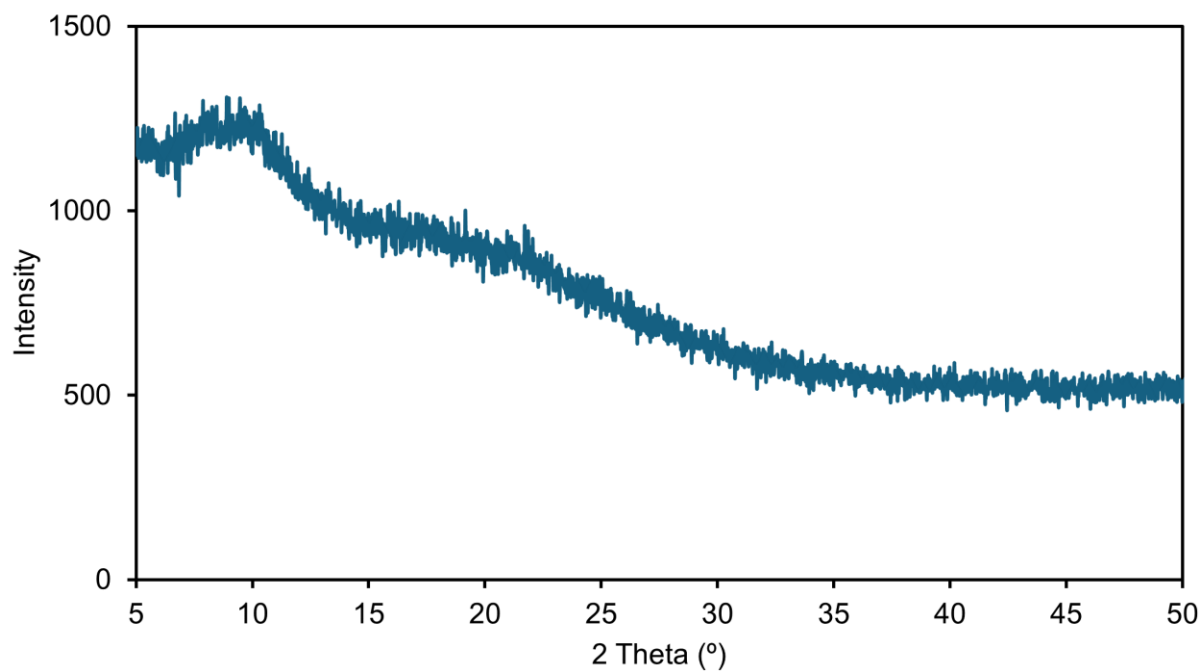


Figure S 3-2. XRD measurements of Fe-fum NPs synthesized in protein-preserving conditions.

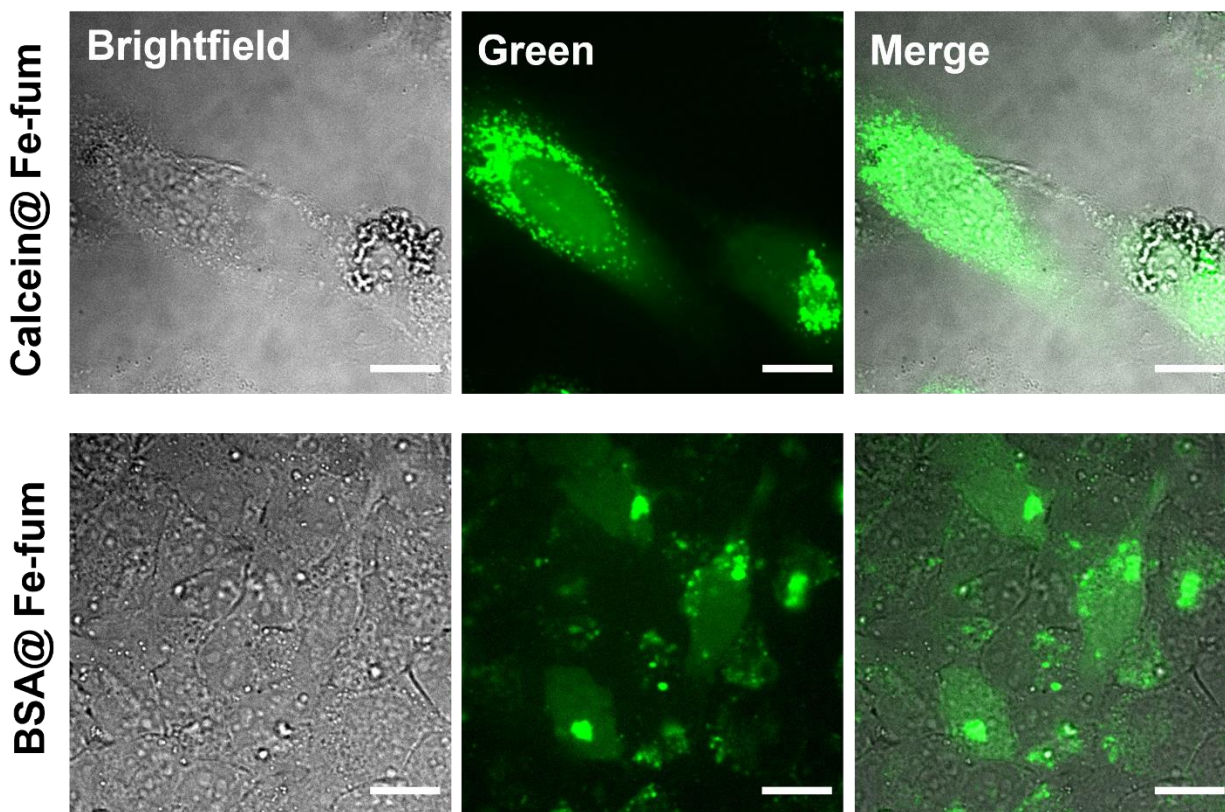


Figure S 3-3. Confocal images of *HeLa* cells incubated with lipid-coated, calcein-loaded or FITC-BSA@Fe-fum for 3 days. The widespread green signal represents the cytosolic release of calcein or FITC-BSA without further treatments. The scale bar is 20 μm .

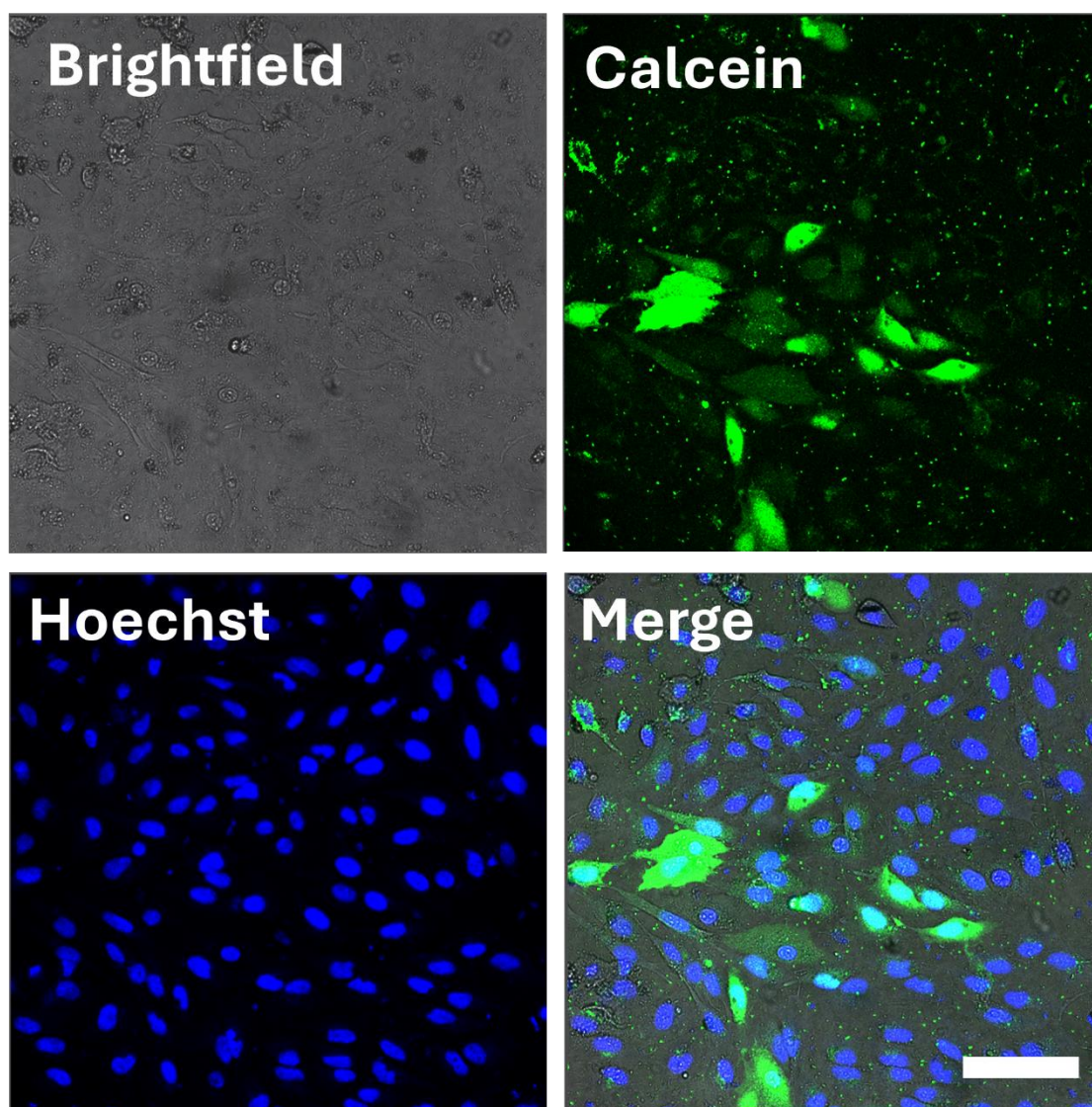


Figure S 3-4. Fluorescence microscope images of *HeLa* cells incubated with lipid-coated, histidine, and calcein-loaded Fe-fum for 3 days. The widespread green signal represents the cytosolic release of calcein without further treatments. The scale bar is 100 μm .

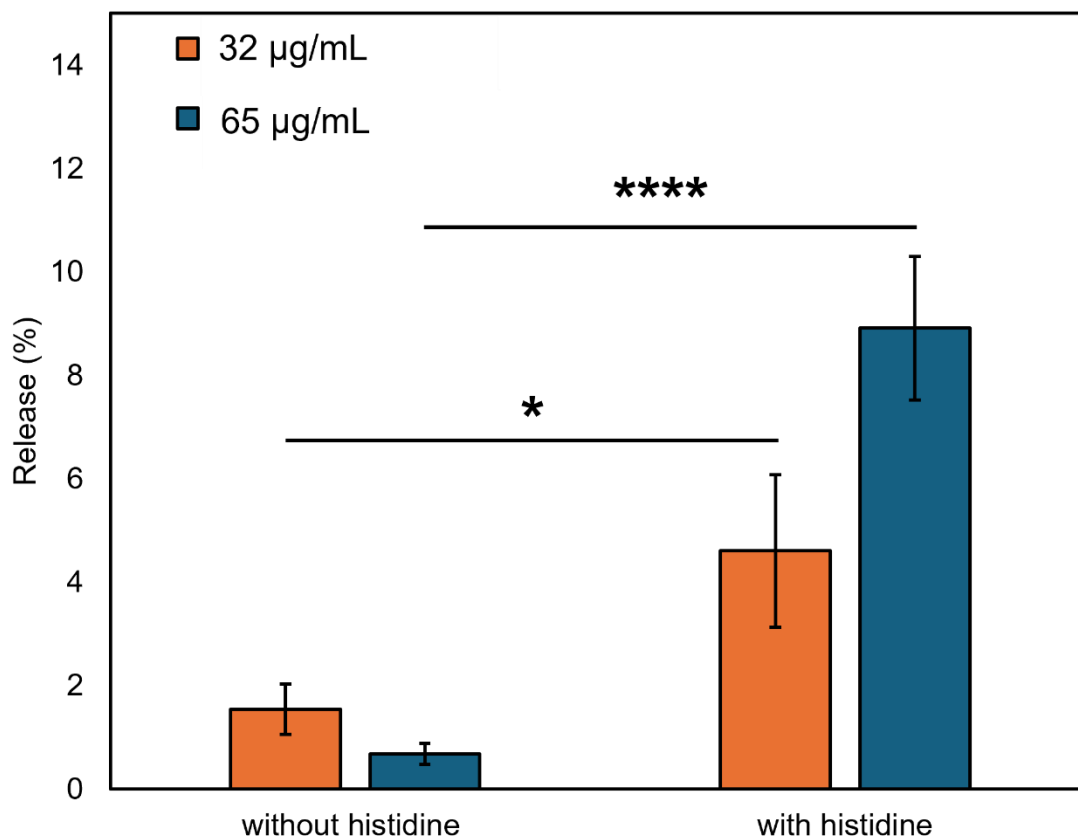


Figure S 3-5. A comparison between the release efficiency of the Fe-fum nanoparticles with and without histidine. *HeLa* cells were incubated with 32 or 65 µg/mL of Fe-fum loaded with and without histidine, and the cells with calcein release were counted after three days. The release efficiency was calculated by dividing the number of cells with calcein release by the total cells per image. Error bars represent standard error of the mean (SEM); n=8-20 images including 2000-4000 cells per experimental condition; statistical analysis performed using one-way ANOVA; *p<0.05, ****p<0.0001.

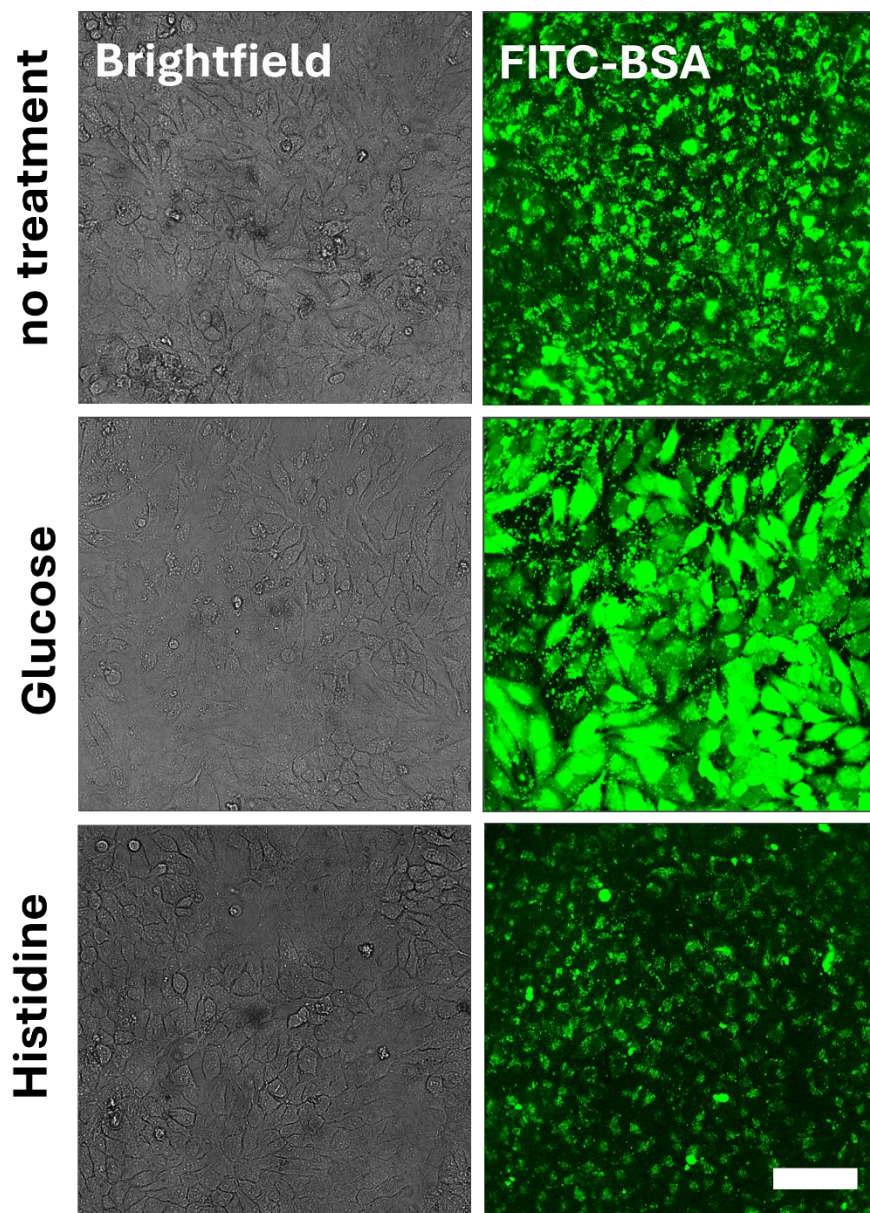
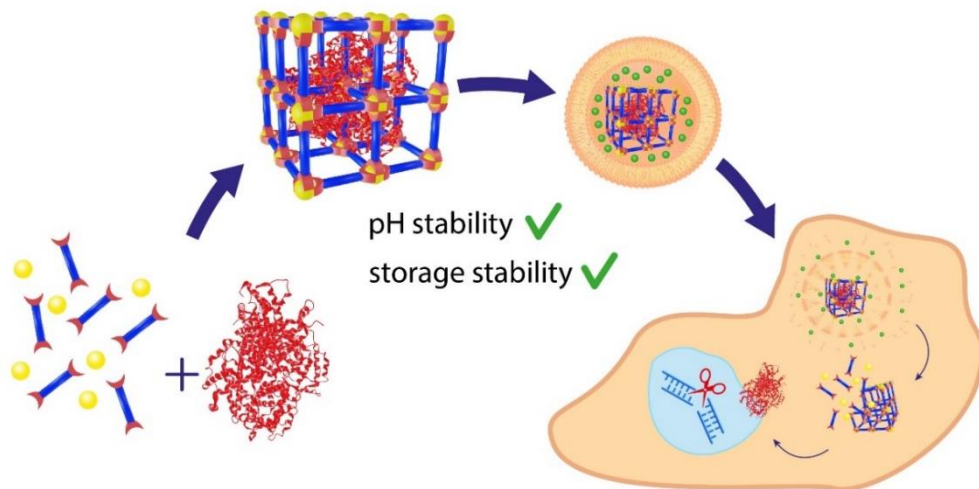


Figure S 3-6. Intracellular delivery of BSA facilitated by lipid-coated Fe-fum nanoparticles in *HeLa* cells following a 3-day incubation with lipid-coated BSA-loaded Fe-fum. Glucose shock and histidine were employed as external and internal endosomal triggers, respectively. The widespread green signal indicates the cytosolic release of FITC-labeled BSA. Scale bar: 100

CHAPTER 4

Biomimetic Mineralization of Iron-Fumarate Nanoparticles for Protective Encapsulation and Intracellular Delivery of Proteins



4. Biomimetic Mineralization of Iron-Fumarate Nanoparticles for Protective Encapsulation and Intracellular Delivery of Proteins

This chapter was published as:

Negar Mirzazadeh Dizaji, Yi Lin, Thomas Bein, Ernst Wagner, Stefan Wuttke, Ulrich Lächelt, and Hanna Engelke

Chemistry of Materials 2022 34 (19), 8684-8693

DOI: 10.1021/acs.chemmater.2c01736

Abstract

Biomimetic mineralization of proteins and nucleic acids into hybrid metal-organic nanoparticles allows for protection and cellular delivery of these sensitive and generally membrane-impermeable biomolecules. Although the concept is not necessarily restricted to zeolitic imidazolate frameworks (ZIFs), so far reports about intracellular delivery of functional proteins have focused on ZIF structures. Here, we present a green room-temperature synthesis of amorphous iron-fumarate nanoparticles under mildly acidic conditions in water to encapsulate bovine serum albumin (BSA), horse radish peroxidase (HRP), green fluorescent protein (GFP), and Cas9/sgrRNA ribonucleoproteins (RNPs).

The synthesis conditions preserve the activity of enzymatic model proteins and the resulting nanoparticles deliver functional HRP and Cas9 RNPs into cells. Incorporation into the iron-fumarate nanoparticles preserves and protects the activity of RNPs composed of the acid-sensitive

Cas9 protein and hydrolytically labile RNA even during exposure to pH 3.5 and storage for two months at 4 °C, which are conditions that strongly impair the functionality of un-protected RNPs. Thus, the biomimetic mineralization into iron-fumarate nanoparticles presents a versatile platform for the delivery of biomolecules and protects them from degradation during storage under challenging conditions.

4.1. Introduction

Biomacromolecules such as RNA and proteins are of great importance for a wide range of applications in the life sciences. Their utilization and the exploitation of their potential, however, faces several challenges, particularly with respect to their stability and delivery into cells. Unlike many small molecules, they are not readily internalized by cells and most of them have to be delivered— including in in-vitro settings¹. Thus, even for in vitro applications, suitable carrier systems have to be designed. Furthermore, the large size of many biomacromolecules impedes loading into the small pores of most common porous nanomaterials. Additionally, most of the employed biomolecules are fragile and need to be protected from harsh conditions as well as hydrolytic, enzymatic, or other degradation mechanisms. The accommodation of biomolecules in larger pores of inorganic nanoparticles or in polymeric nanoparticles has been achieved^{2,3}. Similarly, delivery of various proteins and nucleic acids has been achieved via lipid⁴ or polymer-nanoparticles⁵, large-pore inorganic^{6,7} or hybrid nanoparticles^{8,9}, as well as by addition of cell-penetrating peptides^{10,11} and other modifications that facilitate intracellular delivery. However, protection of the sensitive cargo from degradation still remains a major challenge.

A seminal work on the biomimetic mineralization of proteins into metal-organic framework (MOF) nanoparticles has revealed a solution for protecting biomolecules from very harsh conditions^{12,13}. In this approach, MOFs are synthesized in presence of the protein, incorporating it into the structure and releasing it upon MOF degradation^{12,14}. Incorporation into the MOF structure protects the proteins from heat and other harsh conditions¹². This technique of MOF-based biomimetic mineralization has been successfully applied to generate nano-biocomposites, which deliver a variety of proteins into cells, such as antibodies¹⁵, caspases¹⁶, and Cas9^{14,17}.

These applications were mainly based on the zinc imidazolate framework (ZIF) materials ZIF-8 and ZIF-90, which consist of Zn and imidazole derivatives¹⁸. A reason for selecting these ZIF structures is that they can be synthesized under aqueous conditions, at room temperature, and physiological pH. The imidazoles within the ZIF structures get protonated at slightly acidic pH¹⁹, which is favorable for disassembly and cargo release within endo- and lysosomes¹⁴. However, the characteristic of being readily degradable can cause issues for storage. Furthermore, Zn ions are important signaling messengers and can be very toxic to cells²⁰. Therefore, nanoparticles alternative to ZIF-8 and ZIF-90 are needed for biomimetic mineralization under conditions that preserve proteins and their function.

Iron-fumarate nanoparticles, such as MIL-88A, have shown great promise for drug delivery^{21,22}. They can be imaged via MRI^{23,24} and have been used to deliver small molecules to cells^{21,25}. Both building blocks – fumaric acid and iron – are naturally present in the human body and therefore relatively well tolerated^{26,27}. A study on cytotoxicity of MOF nanoparticles based on Fe, Zn and Zr showed that Fe-based MOFs were less toxic to *HeLa* and J774 cells than Zn and Zr MOFs²⁸. Iron-fumarate nanoparticles can be synthesized via biomimetic mineralization to include BSA¹². However, so far, the synthesis procedure was performed at acidic pH 2.5 that is not tolerated by many proteins. For example, Cas9, which receives much attention as a highly flexible gene editing tool, has been reported to irreversibly lose its bioactivity upon exposure to acidic pH < 4²⁹. Here, we introduce a biomimetic mineralization of proteins with iron-fumarate nanoparticles at pH 4.8, which preserves and shields pH-sensitive protein structures. We show that iron-fumarate nanoparticles can be used as an alternative to ZIF nanoparticles for delivery of proteins, such as Cas9. Importantly, the iron-fumarate platform preserves protein functionality during synthesis,

delivery, release, and even under harsh conditions such as storage at acidic pH or in ethanol (Figure 4-1).

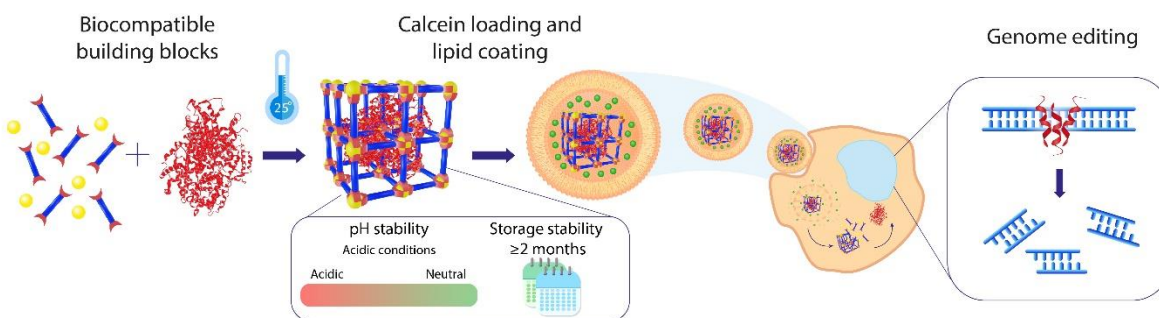


Figure 4-1. Overview of synthesis and protective properties of Fe-fum nanoparticles, as well as their use for intracellular delivery of functional proteins, such as Cas9/sgRNA RNPs for genome editing.

4.2. Results

4.2.1. Synthesis and Characterization of Biomimetically Mineralized Iron-fumarate Nanoparticles

In previous protocols, spherical iron-fumarate nanoparticles were synthesized via room temperature precipitation from water-based solutions of fumaric acid and iron chloride^{21,25,26}. Due to the fumaric acid, this occurs at a pH of 2.5. To accommodate proteins and preserve their structure and function, we developed a synthesis protocol at less acidic pH. Increasing the pH decreases protonation of fumaric acid and thus its reactivity with iron and subsequent nanoparticle formation. Therefore, the pH had to be balanced to preserve protein function and at the same time allow for nanoparticle formation, yielding pH 4.8 as best compromise. To compensate for the reduced reactivity of fumaric acid, the molar ratio of fumaric acid to iron was increased from 1:1

to 10:1. Briefly, nanoparticle formation was initiated by incubation of proteins with fumaric acid at pH 4.8, followed by addition of iron chloride (**Figure 4-2a**). Subsequently, the resulting iron-fumarate nanoparticles (Fe-fum NPs) were washed with ethanol. For cell experiments, the particles were loaded with calcein and coated with a lipid layer via a fusion method as described previously²¹. The co-encapsulated calcein enabled visualization by fluorescence microscopy and additionally stabilized the lipid layer³⁰. As observed previously, lipid coating facilitates cellular uptake of iron-fumarate-based nanoparticles and thereby contributes to successful delivery²¹. To confirm that Fe-fum NPs can serve as a versatile platform for protective encapsulation and intracellular delivery of proteins, different proteins were encapsulated: bovine serum albumin (BSA), horse radish peroxidase (HRP), green fluorescent protein (GFP), and Cas9/sgRNA ribonucleoproteins (RNPs).

A detailed materials characterization was carried out with BSA biomimetically mineralized into Fe-fum NPs (BSA@Fe-fum). Scanning electron microscopy (SEM) reveals a spherical morphology and an average size of 30 nm (**Figure 4-2b, Figure S 4-1**). As displayed in the SEM images in **Figure 4-2b**, morphology and size of Fe-fum NPs did not change upon incorporation of BSA nor upon lipid coating. Dynamic light scattering (DLS, **Figure 4-2c**) of the Fe-fum NPs without incorporated proteins shows a homogeneous size distribution around a hydrodynamic diameter of 220 nm, which is within a suitable range for drug delivery purposes. After incorporation of BSA, the majority of Fe-fum NPs showed a size distribution around 200 nm. However, a second population with larger sizes appeared, indicating a certain degree of aggregation. DLS of lipid coated Fe-fum NPs resulted in a size distribution of the main fraction of nanoparticles around 70 nm. All lipid-coated Fe-fum NPs exhibited a negative zeta potential. The

zeta potential of lipid-coated Fe-fum NPs without protein was -33 mV, which was slightly increased upon incorporation of proteins as displayed in **Figure 4-2d**.

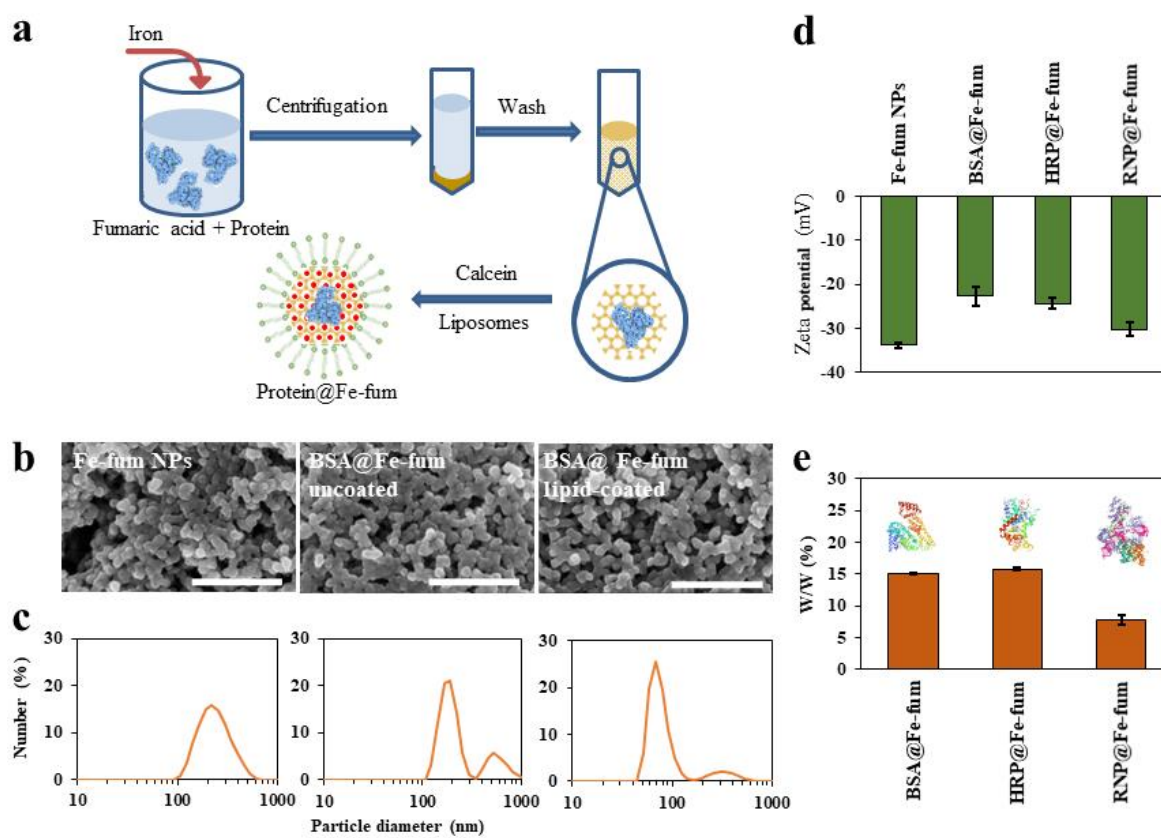


Figure 4-2. Preparation and characterization of Fe-fum NPs and protein@Fe-fum. (a) Schematic of biomimetic synthesis of Fe-fum NPs; BSA is used as model protein. (b) SEM images (scale bar: 400 nm), and (c) size distribution obtained via DLS measurements of Fe-fum NPs, BSA@Fe-fum without lipid-coating and lipid-coated BSA@Fe-fum, respectively. (d) Zeta potential of Fe-fum NPs and protein@Fe-fum; proteins include BSA, HRP and Cas9/sgRNA RNP dispersed in water. (e) Quantification of encapsulated proteins (BSA, HRP and Cas9/sgRNA RNP) assessed by disintegration of uncoated NPs and a subsequent BCA assay.

X-ray diffraction (XRD, **Figure S 4-2**) and infrared spectroscopy (IR) data (**Figure S 4-3**) are consistent with data found in the literature for other iron-fumarate nanoparticles²⁶. Particularly, the amorphous nature revealed by XRD has been described for iron (III) fumarate nanoparticles with

similarly spherical shape²⁶. IR was further used to assess the incorporation of HRP and Cas9 RNP into the Fe-fum NPs. In the IR spectra, the peak in the range of 1600-1710 cm⁻¹ represents a typical protein signal (corresponding to the amide I band, mainly from C=O stretching vibrations)³¹. It is present in the spectra of Fe-fum NPs incorporating HRP and Cas9 RNP and it is absent in the spectrum of Fe-fum NPs without incorporated proteins. This confirms that HRP and Cas9 RNP were successfully incorporated in the Fe-fum NPs (SI, **Figure S 4-3**).

Protein encapsulation was further quantified with a BCA (bicinchoninic acid) assay of Fe-fum NPs degraded with citrate buffer. The protein loading efficiency was calculated as the percentage of protein incorporated in Fe-fum NPs relative to the total initial protein provided during synthesis, and the protein loading capacity was quantified as the weight percentage of the incorporated protein per mg Fe-fum NPs. For BSA and HRP, loading efficiencies of 84% and 86%, respectively, and loading capacities of 15% and 15.7%, respectively, were obtained. The same initial concentration of Cas9 RNP yielded a lower loading efficiency of 38% and lower loading capacity of 7.8% (**Figure 4-2e**). The reduced loading efficiencies and capacities for Cas9 may be attributed to its physical and chemical characteristics, which differ from BSA and HRP. Most likely, it is a result of its much larger size (160 kDa) compared to BSA (69 kDa) and HRP (44 kDa), which might lead to steric effects reducing the packing efficiency. Nevertheless, compared to Cas9 loading into ZIF nanoparticles reported in the literature (1.2 %) ¹⁴, the loading capacity of 7.8% that we achieve with Fe-fum NPs is considerably higher.

To assess whether Fe-fum NP synthesis preserves protein function, we initially used GFP fluorescence as marker. While GFP fluorescence was strongly reduced during synthesis at pH 2.5, the synthesis at pH 4.8 described here preserved GFP fluorescence (**Figure S 4-4**).

4.2.2. Intracellular Delivery of BSA

Next, we studied the potential of the Fe-fum NPs to deliver proteins into cells using three different proteins of increasing complexity. First, we used BSA fluorescently labeled with Atto633 as a model protein to assess intracellular release and effects on cell viability. The metabolic activity of *HeLa* cells was determined by MTT assay after 48 h incubation with various amounts of lipid-coated, calcein-loaded BSA@Fe-fum (0-240 $\mu\text{g}/\text{mL}$). Up to a concentration of 30 $\mu\text{g}/\text{mL}$ BSA@Fe-fum, no obvious reduction of cell viability could be observed compared to untreated controls. Even at the highest dose of 240 $\mu\text{g}/\text{mL}$, the effect on cell viability was less than 50 % (Figure 4-3a). We then used fluorescence microscopy to monitor the intracellular localization and release of the fluorescent cargos calcein and Atto633-BSA. To observe significant intracellular release, we applied a brief osmotic shock by exposing the cells to 1 M glucose for 6 mins followed

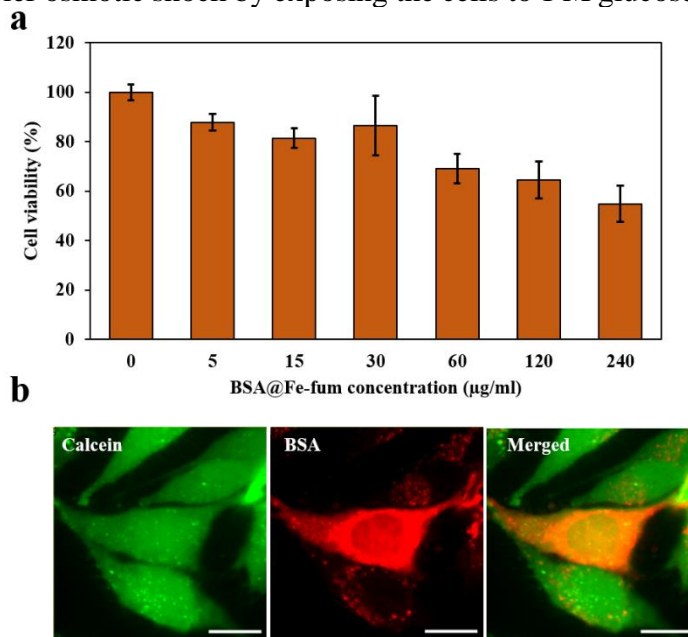


Figure 4-3. Cell viability and release of BSA@Fe-fum. a) Viability of *HeLa* cells treated with lipid-coated, calcein-loaded BSA@Fe-fum for 48 hours measured with an MTT assay. b) Confocal images of *HeLa* cells incubated with lipid-coated, calcein-loaded Atto633-BSA@Fe-fum for 3 days. Green: calcein, Red: Atto-633 labelled BSA. Scale bar: 10 μm .

by replacement with fresh medium. While glucose shock may be a limitation for therapeutic applications, it also provides the advantage of temporal control of endosomal release and intracellular activity for applications in biotechnology or research on cell biology. The homogenous distribution of both calcein and Atto633-BSA in the cells after glucose shock suggests intracellular degradation of the Fe-fum NPs and release of the contained fluorescent cargos (**Figure 4-3b**).

4.2.3. Intracellular Delivery and Activity of HRP

To observe protein function after intracellular delivery, we investigated the delivery of horse radish peroxidase (HRP). HRP is a widely used enzyme that catalyzes the oxidation of a variety of organic substrates by means of hydrogen peroxide. To assess the functionality of HRP, we therefore used Amplex UltraRed as substrate, which is a non-fluorescent molecule that is converted to fluorescent resorufin upon HRP-catalyzed oxidation by hydrogen peroxide (**Figure 4-4a**)^{32,33}. Prior to cell experiments, we tested the activity of HRP after incorporation into the Fe-fum NPs. To this end, Fe-fum NPs with biomimetically incorporated HRP (HRP@Fe-fum) were disintegrated by incubation in citrate buffer. Subsequently, the disintegrated HRP@Fe-fum were incubated in a solution of Amplex UltraRed and hydrogen peroxide. As shown in **Figure 4-4b**, fluorescence emission was detected in the disintegrated HRP@Fe-fum, but not in controls of Fe-fum NPs without HRP. Comparing the enzyme kinetics between HRP released from degraded HRP@Fe-fum and free HRP added to degraded Fe-fum NPs, we found that the Michaelis-Menten constant K_M , i.e. the substrate-enzyme binding rates, are comparable within errors (182 \pm 73 μ M for free HRP and 127 \pm 39 μ M for HRP from HRP@Fe-fum). These values are similar to K_M values for HRP reported in literature³⁴. However, the catalytic rate of the enzyme k_{cat} is reduced in HRP

released from degraded HRP@Fe-fum to about 2.5% of the value of free HRP. This is in accordance with reports in the literature on interactions of carboxylic acids with the heme-group of the active site of horseradish peroxidase, which lead to a reduction of the enzyme activity rate to a similar extent as we observe for HRP released from Fe-fum NPs³⁵. Thus, the activity of HRP was reduced, but still clearly detectable after synthesis, encapsulation and release. Therefore, we next studied its enzymatic activity after intracellular delivery using the same assay of Amplex UltraRed oxidation to fluorescent resorufin. *HeLa* cells were incubated with lipid-coated, calcein-loaded HRP@Fe-fum and treated with hydrogen peroxide and Amplex UltraRed. The widespread green fluorescent signal in **Figure 4-4c** suggests efficient release of calcein after glucose shock.

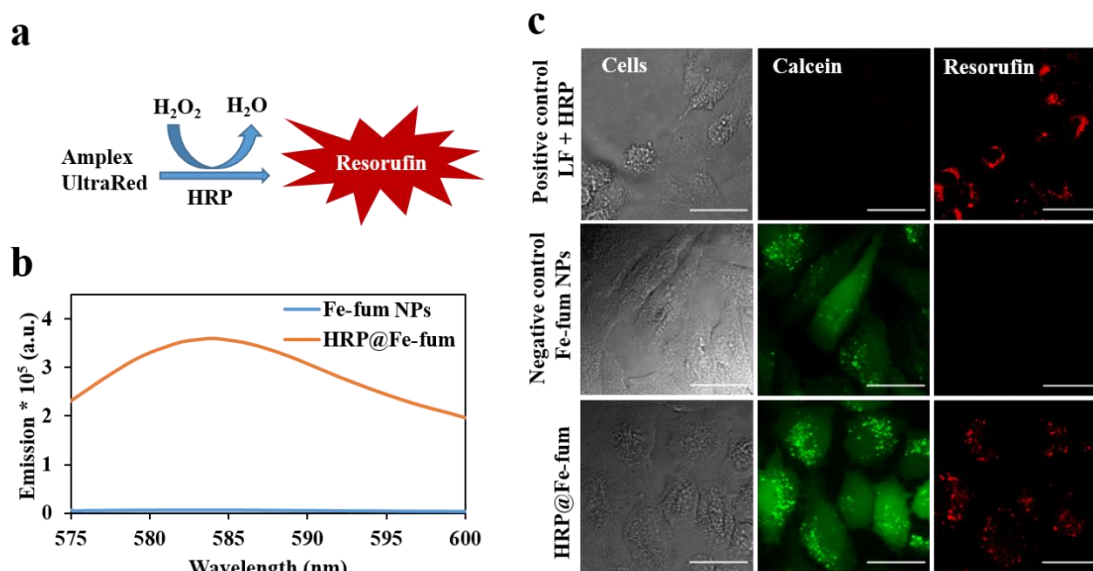


Figure 4-4. Intracellular activity of HRP delivered by HRP@Fe-fum. **(a)** Catalytic reaction of HRP with Amplex UltraRed resulting in the formation of fluorescent resorufin. **(b)** Fluorescence emission after exposure of Amplex UltraRed to disintegrated Fe-fum NPs and HRP@Fe-fum shows activity of HRP after release from HRP@Fe-fum (orange), while controls without HRP do not show activity (blue). **(c)** Confocal microscopy images of *HeLa* cells after incubation with lipofectamine (LF) and HRP as positive control for HRP-induced Amplex UltraRed fluorescence signal, lipid-coated, calcein-loaded Fe-fum NPs without HRP as a negative control, and lipid-coated, calcein-loaded HRP@Fe-fum showing that HRP@Fe-fum NPs release calcein (green channel) and deliver active HRP inducing formation of fluorescent resorufin (red channel). Scale bar: 20 μm.

Importantly, we observed a red fluorescent signal resulting from resorufin formation in cells incubated with HRP@Fe-fum, but not in control cells treated with Fe-fum NPs without HRP. The resorufin-signal was also observed in positive controls employing HRP transfected with lipofectamine. Cell morphology changed in cells incubated with HRP and in positive controls, but not in negative controls without HRP. Lipid oxidation is known to induce such morphology and can ultimately lead to cell death. The morphology changes may thus result from HRP-catalyzed oxidation of lipids or other important cell constituents. All in all, the observed fluorescence signal and cell morphology suggest active HRP to be successfully delivered into cells with HRP@Fe-fum.

4.2.4. Intracellular Delivery, Activity, and Preservation of Cas9/sgRNA RNPs

CRISPR/Cas technology is emerging as a key tool for applications in therapy and biotechnology^{36,37}. For this technology to work, ribonucleoprotein complexes (RNPs) of Cas9 protein and single guide RNA (sgRNA) have to act in concert inside cells³⁸. Within this complex, Cas9 is a programmable endonuclease, which cleaves DNA at a target site as guided by the sgRNA. Cas9/sgRNA RNPs³⁹, however, are very sensitive to pH and hydrolysis, complicating storage and thus their application. Therefore, we next tested the potential of Fe-fum NPs to protect and deliver active Cas9/sgRNA RNPs into cells. As for the investigations with HRP, we assessed the preservation of RNP activity during Fe-fum NP synthesis, encapsulation and release prior to cell experiments. To this end, an *in vitro* cleavage assay was carried out, which allows for the determination of the sequence-specific nuclease activity of Cas9/sgRNA RNPs (**Figure 4-5a**). Briefly, in this assay, a linearized plasmid containing the EGFP gene (pEGFP_{Luc}) was incubated with the RNP containing Cas 9 and an EGFP specific sgRNA (sgGFP). In case of active RNPs,

the endonuclease Cas9 cleaves the plasmid into two fragments (SI, **Figure S 4-5a**), which can be separated and detected by gel electrophoresis. The relative band intensities of the linearized plasmid versus the resulting fragments can be used as a measure of RNP activity. As shown in **Figure S 4-5b**, incubation in fumaric acid at pH values down to pH 4.8 – a pH that is not tolerated by Cas9 RNPs in absence of fumaric acid - did not reduce RNP activity suggesting that fumaric acid protected the RNP complex from pH-induced deactivation. Incubation of Cas9/sgRNA RNPs with degraded Fe-fum NPs slightly reduced activity of RNP, but nevertheless showed very high activity (**Figure S 4-6**). Also the cleavage assay of degraded Fe-fum NPs containing biomimetically incorporated Cas9/sgRNA RNPs (RNP@Fe-fum) revealed cleavage of the substrate (**Figure 4-5b**), however, cleavage efficiency was reduced compared to free RNP controls. This reduction in cleavage efficiency may result from the conditions used for degradation of the Fe-fum NPs. In particular, the cysteine used for degradation of Fe-fum NPs can reduce RNP activity, as shown by the control of free RNPs directly incubated with cysteine (**Figure S 4-6**, for details on degradation by cysteine see **Figure S 4-7** and **Figure S 4-8**). Even though we cannot fully exclude that the observed reduction in activity occurs during synthesis or during degradation of the loaded RNP@Fe-fum NPs in the cell, the observed activity encourages further experiments on intracellular delivery. Therefore, we next analyzed the efficiency of the biomimetically mineralized RNP@Fe-fum to mediate gene knockout in cells. To this end, we incubated *HeLa* cells expressing GFP-tubulin (*HeLa* GFP-tub) with lipid-coated, calcein-loaded RNP@Fe-fum that contained the same sgRNA targeting the GFP coding region used in the in vitro cleavage assay. In case of successful intracellular delivery, cleavage of the GFP gene leads to gene knockout and loss of fluorescence. This is depicted in **Figure 4-5c**, which shows a cell with GFP-tubulin

and a cell without fluorescence upon GFP knockout. The knockout efficiency after cellular treatments was quantified by flow cytometry. To exclude artifacts due to co-delivered calcein, which has a fluorescence spectrum overlapping with GFP, the cells were passaged twice and re-grown for two days after each passage (**Figure S 4-9**). After treatment with lipid-coated, calcein-loaded RNP@Fe-fum at concentrations corresponding to 75 and 110 nM Cas9 RNP, knockout efficiencies amounted to 16 and 30%, respectively (**Figure 4-5d**). Lipofectamine CRISPRMAX (LF CM), which was used as a commercially available benchmark reagent, yielded knockout efficiencies of 22 and 23% at the same concentrations of 75 and 110 nM Cas9 RNP. Hence, RNP@Fe-fum mediated higher knockout levels at 110 nM RNP compared to LF CM. In contrast, negative controls of Fe-fum NPs without RNP and Fe-fum or LF with a control sgRNA, without target sequence in the genome, did not show GFP knockout (**Figure S 4-10, 11 and 12**). With these knockout efficiencies, biomimetically mineralized iron-fumarate nanoparticles may represent a good alternative for the delivery of Cas9/sgRNA RNPs into cells.

Next, we studied the ability of biomimetically mineralized Fe-fum NPs to protect Cas9/sgRNA RNPs from degradation under challenging conditions. Importantly, all RNP@Fe-fum are washed and stored in ethanol after synthesis and before lipid coating. Thus, the knockout efficiencies obtained above already show that Fe-fum NPs successfully protect RNPs from potential negative impact of ethanol. RNPs and many other proteins lose their activity under acidic conditions^{29,40}. Therefore, we assessed the ability of biomimetically mineralized Fe-fum NPs to protect RNPs from acidic pH. The experiments shown above on the protection of RNP by fumaric acid at pH 4.8, which otherwise inactivates RNPs, already suggest that RNPs might also be protected in the Fe-fum NPs.

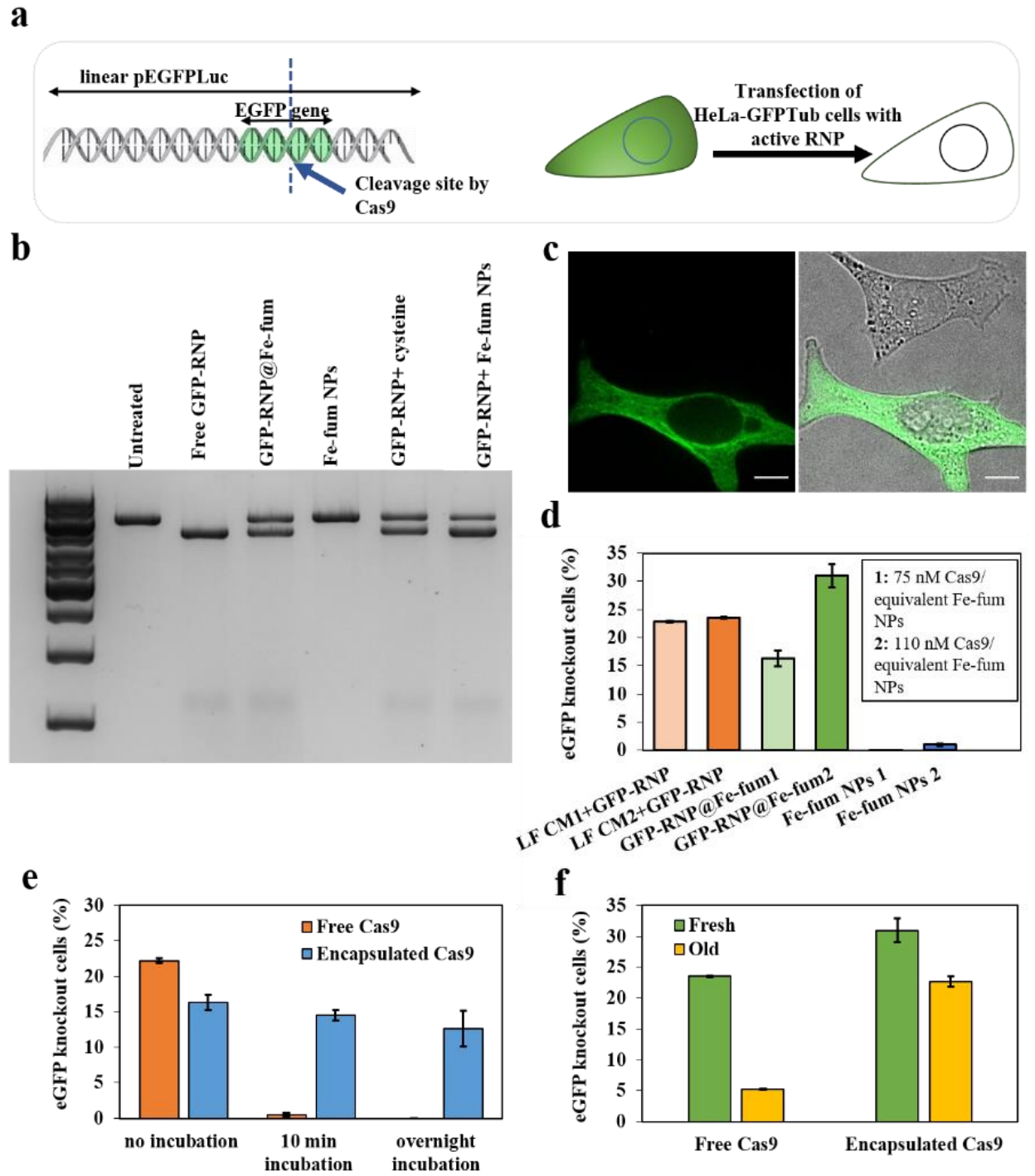


Figure 4-5. In vitro and intracellular activity of Cas9 RNP. **a)** Schematic of the cleavage of the EGFP gene, and cellular knockout caused by Cas9/sgGFP RNP. **b)** Agarose gel electrophoresis of cleavage assay confirming RNP-activity after RNP@Fe-fum synthesis. The samples were an untreated control, free RNP, degraded RNP@Fe-fum, degraded Fe-fum NPs without RNP, RNP added to degraded Fe-fum NPs after NP degradation, RNP exposed to 80 mM cysteine (concentration used for Fe-fum NP degradation). **c)** Microscopy images of a cell with GFP-tubulin expression (bottom) and knocked out GFP (top). The left image represents the GFP channel, the right image the overlay with brightfield. Scale bar: 10 μ m **d)** Knockout efficiency of lipid-coated, calcein-loaded RNP@Fe-fum corresponding to two different concentrations of RNP: 75 nM (RNP@Fe-fum 1) and 110 nM Cas9 RNP (RNP@Fe-fum 2). The corresponding amounts of Fe-fum NPs without RNP served as negative controls. As positive control, cells were transfected with the same concentrations of Cas9/sgGFP RNP using Lipofectamine CRISPRMAX (LF CM). LF CM1 and LF CM2 contain 75 nM and 110 nM Cas9, respectively. The impact of acidic conditions **(e)** and a two-month storage at 4 °C **(f)** on the knockout efficiency of encapsulated and free RNP. Free RNP was delivered into the cells via lipofectamine. Data are presented as mean \pm SD (n = 3).

To further investigate the potential protection from acidic conditions, we exposed lipid-coated, calcein-loaded RNP@Fe-fum to an acidic environment (pH 3.5) for a short-term (10 min) and a long-term (overnight) incubation. The stability of Fe-fum NPs was confirmed by UV/VIS spectrometry (**Figure S 4-13**) and subsequently, the RNP activity was measured via cellular gene knockout efficiency. While a control of free and unprotected RNP, which was incubated under the same conditions and subsequently transfected with lipofectamine, lost its activity already after 10 min incubation at pH 3.5, RNPs incorporated into Fe-fum NPs retained their activity and achieved similar knockout levels even after overnight incubation at acidic pH (**Figure 4-5e**). In addition to the protective properties against acidic conditions, we also evaluated the ability of biomimetically mineralized Fe-fum nanoparticles to facilitate long-term storage. Again, free RNP stored for two months at 4 °C and transfected with lipofectamine, lost almost all its cellular knockout efficiency. In contrast, RNP@Fe-fum stored for the same time at 4 °C, achieved almost the same knockout levels as the fresh RNP@Fe-fum (**Figure 4-5f**). Thus, the biomimetically mineralized Fe-fum NPs provide good protection of incorporated Cas9/sgRNA RNPs and are a promising storage form.

4.3. Conclusion

In conclusion, we have developed a synthesis protocol for biomimetically mineralized iron-fumarate nanoparticles that preserves proteins and their function. The resulting Fe-fum NPs had comparably high loading efficiency of proteins and successfully delivered them into cells preserving protein activity. Delivery of Cas9/sgRNA RNPs showed efficient gene knockout in *HeLa* cells. While other efficient delivery systems for proteins exist ⁵, generic strategies for flexible encapsulation of different proteins and their protection from degrading conditions are still challenges. The biomineralization approach presented here is a versatile platform as shown by the four different encapsulated model proteins (BSA, eGFP, HRP, Cas9/sgRNA RNPs). Furthermore, the biomimetically mineralized Fe-fum NPs provide very good protection of Cas9/sgRNA RNPs against acidic pH and allowed for storage over two months at 4 °C. They do not show efficient release without glucose shock, which demands further research for on-board release triggers for therapeutic applications. Yet, the glucose shock allows for temporal control of release in applications in biotechnology and cell biology research. Thus, the Fe-fum NPs present a valuable alternative to existing ZIF or polymer delivery systems, specifically when protein protection or temporal control of release is necessary.

4.4. Material and methods

4.4.1. Synthesis

Chemicals

Chemicals were purchased from Sigma Aldrich (St. Louis, MO, USA), if not stated otherwise.

Biomimetic mineralization of protein@Fe-fum

20 mL of a 10 mM solution of fumaric acid in deionized water was prepared and the pH of the solution was adjusted to 4.8 by adding NaOH. Proteins were added into the solution of fumaric acid in the concentration range of 30-150 µg/ml. The mixture was incubated for 10 min at room temperature and 750 rpm stirring. A separate solution of iron chloride in deionized water (10 mM, 2 mL) was prepared. Then, the iron chloride solution was added to the fumaric acid and protein mixture in 5 steps at 20 s intervals. The resulting protein@Fe-fum were washed three times by centrifugation at 7179 RCF for 20 min and subsequent redispersion in ethanol.

Production and purification of Cas9 protein

Production and purification of Cas9 protein were performed as previously reported⁵. pET28a/Cas9-Cys was a gift from Hyongbum Kim⁴¹ (Addgene plasmid # 53261; <http://n2t.net/addgene:53261>; RRID:Addgene_53261). In brief, the plasmid pET28a/Cas9-Cys was transformed into Rosetta BL21 (DE3) pLysS competent cells (Merck Millipore, Germany). A monoclonal culture of the bacteria was cultivated in LB medium (34 µg/mL chloramphenicol and 50 µg/mL kanamycin) under shaking (250 rpm) at 37 °C until an optical density at 600 nm of 0.7 was reached. Subsequently, 1 mM isopropyl β-D-1-thiogalactopyranoside (IPTG) was added to induce Cas9 protein expression. Bacteria were then harvested and lysed. Purification of Cas9 protein was conducted by nickel chromatography (HisTrap HP column, GE Healthcare, Sweden) using a gradient from the binding buffer (20 mM trizma-base, 0.5 M NaCl, pH 7.4, 20 mM imidazole) to elution buffer (20 mM trizma-base, 0.5 M NaCl, pH 7.4, 0.5 M imidazole). The fractions containing Cas9 were collected and further purified by size exclusion chromatography on an Äkta purifier system using the storage buffer (20 mM HEPES, 200 mM KCl, 10 mM MgCl₂, and 1 mM DTT) as the mobile phase. The fractions containing Cas9 were combined, and the

concentration of Cas9 was measured using a Nanodrop photometer (Thermo Scientific, USA). The Cas9 solution was aliquoted and stored at -80 °C before use.

Preparing ribonucleoprotein (RNP) complexes

Cas9/sgGFP RNP complexes were formed by mixing Cas9 protein with sgGFP (spacer sequence: GACCAGGAUGGGCACCACCC) or control sgRNA (space sequence: GGGTAACCGTGCGGTCGTAC) at a molar ratio of 1:1 at room temperature (RT) for 15 min. The obtained RNP complexes were diluted in HEPES buffer (20 mM, pH 7.4) to a final concentration of 1.5 µg/µL RNP and directly used for in vitro cleavage assay or preparation of nanoparticles.

Preparing labeled proteins (Atto-BSA and Atto-HRP)

BSA or HRP in solution (3 mg/mL) was labeled with ATTO633-NHS ester fluorescence dye (ATTO-TEC, Siegen, Germany) based on the manufacturer's instruction. In brief, the pH of the protein solution was adjusted to 8.3 with a 0.2 M sodium bicarbonate solution and then incubated with dye at room temperature for 1 hour in the dark. The unbound dye was removed with Bio-Spin 6 size exclusion spin columns (Bio-Rad Laboratories).

Biomimetic mineralization of RNP@Fe-fum

RNP was mixed with a fumaric acid solution (10 mM, 5 mL, pH 4.8) to yield a concentration of 30 µg/mL RNP. The mixture was incubated at room temperature for 10 min and 750 rpm. 500 µl of iron chloride solution (10 mM) was added to the mixture of fumaric acid and RNP in 5 steps at 20 s intervals. The resulting RNP@Fe-fum were washed three times via centrifugation and re-dispersion in ethanol.

Preparation of the calcein-loaded and liposome-coated Fe-fum NPs

A 1 mM solution of calcein in deionized water was prepared. 1 mg of Fe-fum NPs or protein@Fe-fum were redispersed in 1 mL of calcein solution. The mixture was then incubated overnight and at 700 rpm shaking for loading. In the case of protein@Fe-fum, the incubation was performed at 4 °C. Then, the Fe-fum NPs were centrifuged for 5 min at 14000 rpm and the supernatant was discarded to collect the Fe-fum NPs for liposome coating.

The liposome coating of the Fe-fum NPs was performed via a fusion method reported by Illes et al.²¹. In this approach, first, a liposome coating solution was prepared by extruding a 1 mg/mL PBS solution of DOPC (1,2-dioleoyl-sn-glycero-3-phosphocholine, Avanti) through an extruder with a 100 nm pore sized membrane 11 times.

Then, the pellet of the calcein-loaded Fe-fum NPs or calcein-loaded protein@Fe-fum was redispersed in 500 µl of liposome solution, followed by the addition of 500 µl of deionized water and incubation for 2 hours. The particles were then centrifuged (5 min at 14000 rpm) and redispersed in PBS. All cell experiments were performed with lipid-coated, calcein-loaded nanoparticles.

4.4.2. Characterization methods

Dynamic Light Scattering (DLS)

DLS and zeta potential measurements were performed by applying a Zetasizer Nano Series (Nano-ZS, Malvern) equipped with a laser with the wavelength $\lambda = 633$ nm. DLS measurements were performed at 25 °C and PMMA cuvettes were used. Samples for DLS measurements were prepared by diluting the freshly produced NPs or liposome-coated NPs in ethanol or PBS, respectively.

Samples in water were used for the single-point measurements of the NPs' zeta potential by using DTS107 cuvettes. For auto-titration measurements, the additional Zetasizer titration system (MPT-2) based on diluted NaOH and HCl as titrants was used. Samples for this purpose were prepared by diluting the Fe-fum NPs to the concentration of 0.1 mg/mL in water.

Scanning Electron microscopy (SEM)

All SEM micrographs were recorded with a Helios NanoLab G3UC (FEI) operating at 5 kV. For sample preparation, the Fe-fum NP dispersion was dried overnight on a carbon film placed on an aluminum sample holder followed by carbon sputtering before the measurement. For evaluation of the SEM micrographs, the software ImageJ v1.49. was used.

X-ray diffraction (XRD)

XRD experiments were performed on dried Fe-fum NPs or atto-BSA@Fe-fum (before calcein loading). The samples were measured on a STOE Diffractometer System STADI P operating in transmission mode. The setup is using Cu K α 1-radiation with a wavelength $\lambda = 0.15418$ nm.

Infrared spectroscopy (IR)

Infrared spectra of dried sample powder were recorded on a Thermo Scientific Nicolet iN10 IR microscope in reflection-absorption mode with a liquid-N₂ cooled MCT-A detector.

UV absorbance

Fe-fum NP stability in acidic conditions was studied by means of UV-Vis measurements performed with the Thermo Scientific Nanodrop 2000c spectrometer. Before measurements, Fe-

fum NPs were treated with HCl to reach the pH 3.5, and after 10 min the pH was neutralized by adding NaOH.

The bicinchoninic acid assay (BCA assay)

To estimate the protein loading efficiency in the protein@Fe-fum, the encapsulated proteins in the protein@Fe-fum were released by disintegrating the uncoated protein@Fe-fum. To this end, ethanolic suspension of protein@Fe-fum was centrifuged at 16900 RCF for 5 min. The pellet was then re-dispersed in citrate buffer (10 mM) to the same volume as before to allow for the complete dissociation of protein@Fe-fum. Afterward, to quantify the protein loading in protein@Fe-fum, a BCA assay was performed according to the protocol provided by the manufacturer (Pierce™ BCA Protein Assay Kit, Thermo, USA). The albumin standard (BSA), provided in the kit, was diluted sequentially to concentrations between 0-250 µg/mL in citrate buffer or fumaric acid to obtain the standard curve for quantifying the concentration of encapsulated protein and initial protein, respectively. The absorption at 562 nm was measured using a SpectraFluor™ Plus microplate reader S4 (Tecan, Groeding, Austria).

Confocal microscopy

The fluorescence microscope images were taken with a Zeiss Observer SD spinning disk confocal microscope using a Yokogawa CSU-X1 spinning disc unit and an oil objective with 63x or 100x magnification (1.40 N.A.) and BP 525/50 (green channel) and LP 690/50 filters (red channel). For excitation, a 488 nm and a 639 nm laser were used. The images were processed with the ImageJ v2.35 software.

Cell culture

HeLa cells (a human cervical carcinoma cell line) and *HeLa* GFPTub cells (*HeLa* cells stably expressing eGFP-tubulin) were cultivated in Dulbecco's modified Eagle's medium (DMEM, Gibco, USA) with 10% (v/v) fetal bovine serum (FBS, Gibco, USA) and 1% (v/v) penicillin-streptomycin (Gibco, USA). Cells were grown in a cell culture incubator (Hera Cell) at 37 °C with 5% carbon dioxide.

Cell viability assay (MTT assay)

The cytotoxicity of the lipid-coated, calcein-loaded BSA@Fe-fum was studied using an MTT assay (Thermo Fisher, USA). *HeLa* cells were seeded onto 96-well plates with a density of 5000 cells per well 24 h prior to treatment. The cells were then treated with different concentrations of lipid-coated, calcein-loaded BSA@Fe-fum (0 to 240 µg/mL) and each concentration in triplicate. Cells without treatment were used as a control group. After 48 h, the MTT assay was performed. For this, cells were washed twice with PBS and then incubated for 2 hours in DMEM containing 500 µg/mL MTT (3-(4,5-dimethylthiazol-2-yl)-2,5-diphenyltetrazolium bromide) in the incubator (37 °C, 5% carbon dioxide). Subsequently, the supernatant was removed, and the cells were lysed by incubating the plate at -80 °C for at least 20 min. Next, the resulting purple crystals were dissolved in 100 µl of DMSO per well and the absorption at 590 nm was measured using a SpectraFluor™ Plus microplate reader S4 (Tecan, Groeding, Austria). Cell viability was calculated as the ratio of the absorption of wells with treated cells relative to wells with untreated control cells.

In vitro activity assay of HRP

For the in vitro HRP enzymatic activity assay, the Fe-fum NPs and HRP@Fe-fum were centrifuged at 16900 RCF for 5 min. Subsequently, the pellet was re-dispersed in citrate buffer to disintegrate the NPs and release the encapsulated HRP. Then, the decomposed NPs at a volume corresponding to 4 μg HRP were added to 1.5 mL of an aqueous solution containing 2500 μM H_2O_2 and Amplex UltraRed (final concentration 50 μM). The enzyme activity was determined by monitoring the mixtures' fluorescence at an excitation/emission of 571/584 nm. Spectra were recorded with an MD-5020 setup from PTI Photon Technology International. HRP kinetics was performed using free HRP (at a concentration of 0,03 and 0,06 ng/ml) in presence of degraded Fe-fum NPs or degraded HRP@Fe-fum (at a concentration of 30 and 60 ng/ml) and 2500 μM H_2O_2 and Amplex UltraRed concentrations between 0 and 100 μM . The resulting fluorescence intensity was measured at different time points with a SpectraFluorTM Plus microplate reader S4 (Tecan, Groeding, Austria) and 535/590 excitation/emission filters. K_M and k_{cat} were determined via a fit to v_0/E_0 vs. Amplex UltraRed concentration according to the Michaelis-Menten equation as described in literature ³⁴.

Inducing protein release in the cytosol (glucose shock)

To induce protein release from the endosome into the cytosol, a glucose shock was applied. For this purpose, the cell medium was removed, and cells were exposed to a 1 M solution of glucose in DMEM for 6 min. The cells were then washed twice with PBS to remove the glucose completely before fresh DMEM or fluorobrite DMEM (in case of imaging) was added to the cells.

Intracellular activity of HRP

HeLa cells were seeded on ibidi 8-well plates with a density of 5000 cells per well. The next day, cells were treated with lipid-coated, calcein-loaded HRP@Fe-fum and lipid-coated, calcein-loaded Fe-fum NPs as the negative control. After 3 days, the supernatant was removed, and a glucose shock was applied as described above. After 6 min, the cells were incubated with 200 μ l DMEM containing 2500 μ M H₂O₂ and 50 μ M Amplex UltraRed for 30 min at room temperature. Then, the cells were washed with PBS and imaged.

Degradation studies

To study degradation of the Fe-fum NPs, 90 μ g of uncoated HRP@Fe-fum with Atto633-labeled HRP were centrifuged and dissolved in either water at the indicated pH, 10 mM citrate buffer, or cysteine at the indicated concentration in water. If not stated otherwise, the NPs were centrifuged after 7 min and the absorption spectrum of the supernatant was measured using a Thermo Scientific Nanodrop 2000c spectrometer. For analysis, the absorption at 633 nm was used. For kinetics studies, 1 ml of a 20 mM cysteine solution was used to dissolve 900 μ g of HRP@Fe-fum. After the indicated time intervals, 100 μ l samples were taken, centrifuged and the supernatant analyzed with respect to the absorption at 633 nm using a Thermo Scientific Nanodrop 2000c spectrometer.

Compatibility of NPs' synthesis process with RNP (In vitro cleavage assay)

To confirm the compatibility of the fumaric acid (at different pH) as well as the Fe-fum NP synthesis with the RNP, an in vitro cleavage assay was applied. Briefly, a linearized plasmid containing the EGFP gene (linear pEGFPLuc) was incubated with the RNP and the activity of the RNP was visualized via the existence of bands resulting from cleaved plasmid in a 2% agarose

gel. To study the effect of fumaric acid on the activity of RNP, initially the RNP was incubated with fumaric acid for 10 min. Then, the pEGFP_{Luc} was treated with RNPs in 1X Cas9 nuclease reaction buffer (New England Biolabs, NEB) for 1 h. The activity of the RNPs was compared via the amount of cleaved pEGFP_{Luc} in the agarose gel.

To investigate the compatibility of the Fe-fum NP synthesis with RNP, the RNP@Fe-fum were first decomposed by re-dispersing the NP pellet in cysteine (80 mM, pH 5) overnight. Then the pEGFP_{Luc} was treated with the decomposed Fe-fum NPs containing the released RNP. Next, samples were incubated with EDTA 5 mM for 10 min to chelate the free iron ions, which interfere with electrophoresis. Then, activity was measured using electrophoresis as described above.

RNP genome-editing efficiency study (cellular knockout experiments)

HeLa GFPTub cells (GFP-expressing *HeLa* cells) were used as an RNP-transfection cell model. 24 h before treatment, cells were seeded at a density of 5000 cells per well onto 96-well plates in 100 μ l of DMEM. The next day, cells were treated with lipid-coated, calcein-loaded RNP@Fe-fum containing 75 or 110 nM Cas9. Cells treated with corresponding concentrations of Fe-fum NPs without RNP, with control RNP that does not target a genome sequence, as well as cells treated only with HEPES buffer served as negative controls. As the positive control, the RNP complex formulated with Lipofectamine CRISPRMAX was applied. All treatments were performed in triplicate. After 48 h, glucose shock was performed in case of the cells treated with Fe-fum NPs, as described above. Then, every 48 hours, the cells were trypsinized and passaged into a new plate. After two passages, the fluorescence signal resulting from the co-loaded calcein disappeared allowing for analysis of GFP-expression without artifacts. 48 hours after the second

passaging, cells were harvested, and the knockout efficiency was determined by flow cytometry (CytoFLEX S, Beckmann Coulter, USA) as the percentage of GFP negative cells after subtraction of unspecific GFP negative population in HEPES treated cells (gating strategy, see **Figure S 4-11**). The GFP knockout was visualized by imaging using an image XPress Micro XLS (Molecular Devices) with a 40x objective and a GFP filter. The resulting images were evaluated with the ImageJ v2.35 software.

Protective feature of NPs against the acidic condition

To study the capability of Fe-fum NPs to protect RNP from acidic conditions, the encapsulated RNP in the lipid-coated, calcein-loaded RNP@Fe-fum, as well as free RNP (both containing 75 nM Cas9), were exposed to a low pH environment by addition of HCl (final pH was 3.5). After a 10-min or overnight incubation, the pH of the environment was neutralized with NaOH. Then, the activity of acid-treated free RNP (transfected with Lipofectamine CRISPRMAX) and encapsulated RNP, as well as a non-treated group of samples, were compared by performing a cellular knockout efficiency experiment as described above.

Stability of encapsulated RNP over time

Lipid-coated, calcein-loaded RNP@Fe-fum and free RNP (both containing 110 nM Cas9) were stored at 4°C for two months. The intracellular activity of old free RNP transfected with Lipofectamine CRISPRMAX and encapsulated RNP were compared with fresh samples by performing a cellular knockout efficiency experiment as described above.

4.5. References

1. Mitragotri, S., Burke, P. A. & Langer, R. Overcoming the challenges in administering biopharmaceuticals: Formulation and delivery strategies. *Nature Reviews Drug Discovery* Preprint at <https://doi.org/10.1038/nrd4363> (2014).
2. Stevens, C. A., Kaur, K. & Klok, H. A. Self-assembly of protein-polymer conjugates for drug delivery. *Advanced Drug Delivery Reviews* Preprint at <https://doi.org/10.1016/j.addr.2021.05.002> (2021).
3. Panta, P. et al. Protein Drug-Loaded Polymeric Nanoparticles. *Journal of Biomedical Science and Engineering* (2014) doi:10.4236/jbise.2014.710082.
4. Cheng, Q. et al. Selective organ targeting (SORT) nanoparticles for tissue-specific mRNA delivery and CRISPR–Cas gene editing. *Nature Nanotechnology* (2020) doi:10.1038/s41565-020-0669-6.
5. Kuhn, J. et al. Delivery of Cas9/sgRNA Ribonucleoprotein Complexes via Hydroxystearyl Oligoamino Amides. *Bioconjugate Chemistry* (2020) doi:10.1021/acs.bioconjchem.9b00853.
6. Gößl, D. et al. Highly active enzymes immobilized in large pore colloidal mesoporous silica nanoparticles. *New Journal of Chemistry* (2019) doi:10.1039/c8nj04585b.
7. Chiu, H. Y. et al. Intracellular chromobody delivery by mesoporous silica nanoparticles for antigen targeting and visualization in real time. *Scientific Reports* (2016) doi:10.1038/srep25019.
8. Möller, K. et al. Highly efficient siRNA delivery from core-shell mesoporous silica nanoparticles with multifunctional polymer caps. *Nanoscale* (2016) doi:10.1039/c5nr06246b.

9. Nouredine, A. et al. Engineering of monosized lipid-coated mesoporous silica nanoparticles for CRISPR delivery. *Acta Biomaterialia* (2020) doi:10.1016/j.actbio.2020.07.027.
10. Endoh, T. & Ohtsuki, T. Cellular siRNA delivery using cell-penetrating peptides modified for endosomal escape. *Advanced Drug Delivery Reviews* Preprint at <https://doi.org/10.1016/j.addr.2009.04.005> (2009).
11. Patel, S. G. et al. Cell-penetrating peptide sequence and modification dependent uptake and subcellular distribution of green fluorescent protein in different cell lines. *Scientific Reports* (2019) doi:10.1038/s41598-019-42456-8.
12. Liang, K. et al. Biomimetic mineralization of metal-organic frameworks as protective coatings for biomacromolecules. *Nature Communications* (2015) doi:10.1038/ncomms8240.
13. Liang, W. et al. Metal-Organic Framework-Based Enzyme Biocomposites. *Chemical Reviews* Preprint at <https://doi.org/10.1021/acs.chemrev.0c01029> (2021).
14. Alsaïari, S. K. et al. Endosomal Escape and Delivery of CRISPR/Cas9 Genome Editing Machinery Enabled by Nanoscale Zeolitic Imidazolate Framework. *Journal of the American Chemical Society* 140, 143–146 (2018).
15. Feng, Y. et al. Antibodies@MOFs: An In Vitro Protective Coating for Preparation and Storage of Biopharmaceuticals. *Advanced Materials* (2019) doi:10.1002/adma.201805148.
16. Chen, T.-T., Yi, J.-T., Zhao, Y.-Y. & Chu, X. Biom mineralized Metal–Organic Framework Nanoparticles Enable Intracellular Delivery and Endo-Lysosomal Release of Native Active Proteins. *J Am Chem Soc* 140, 9912–9920 (2018).

17. Yang, X. et al. Nanoscale ATP-Responsive Zeolitic Imidazole Framework-90 as a General Platform for Cytosolic Protein Delivery and Genome Editing. *J Am Chem Soc* (2019) doi:10.1021/jacs.8b11996.
18. Phan, A. et al. Synthesis, structure, and carbon dioxide capture properties of zeolitic imidazolate frameworks. *Accounts of Chemical Research* (2010) doi:10.1021/ar900116g.
19. Gao, S. et al. Improving the Acidic Stability of Zeolitic Imidazolate Frameworks by Biofunctional Molecules. *Chem* (2019) doi:10.1016/j.chempr.2019.03.025.
20. Yamasaki, S. et al. Zinc is a novel intracellular second messenger. *Journal of Cell Biology* (2007) doi:10.1083/jcb.200702081.
21. Illes, B., Wuttke, S. & Engelke, H. Liposome-Coated Iron Fumarate Metal-Organic Framework Nanoparticles for Combination Therapy. *Nanomaterials* 7, 351 (2017).
22. Ploetz, E., Engelke, H., Lächelt, U. & Wuttke, S. The Chemistry of Reticular Framework Nanoparticles: MOF, ZIF, and COF Materials. *Advanced Functional Materials Preprint at* <https://doi.org/10.1002/adfm.201909062> (2020).
23. Horcajada, P. et al. Porous metal-organic-framework nanoscale carriers as a potential platform for drug delivery and imaging. *Nat Mater* (2010) doi:10.1038/nmat2608.
24. Peller, M., Lanza, A. & Wuttke, S. MRI-Active Metal-Organic Frameworks: Concepts for the Translation from Lab to Clinic. *Advanced Therapeutics* (2021) doi:10.1002/adtp.202100067.
25. Illes, B. et al. Exosome-coated metal-organic framework nanoparticles: An efficient drug delivery platform. *Chemistry of Materials* (2017) doi:10.1021/acs.chemmater.7b02358.

26. Hirschle, P. et al. Tuning the Morphological Appearance of Iron(III) Fumarate: Impact on Material Characteristics and Biocompatibility. *Chemistry of Materials* (2020) doi:10.1021/acs.chemmater.9b03662.
27. Ettliger, R. et al. Toxicity of metal-organic framework nanoparticles: From essential analyses to potential applications. *Chemical Society Reviews* Preprint at <https://doi.org/10.1039/d1cs00918d> (2022).
28. Tamames-Tabar, C. et al. Cytotoxicity of nanoscaled metal-organic frameworks. *Journal of Materials Chemistry B* (2014) doi:10.1039/c3tb20832j.
29. Wei, T., Cheng, Q., Min, Y. L., Olson, E. N. & Siegwart, D. J. Systemic nanoparticle delivery of CRISPR-Cas9 ribonucleoproteins for effective tissue specific genome editing. *Nature Communications* (2020) doi:10.1038/s41467-020-17029-3.
30. von Schirnding, C. et al. Synergistic Combination of Calcium and Citrate in Mesoporous Nanoparticles Targets Pleural Tumors. *Chem* (2021) doi:10.1016/j.chempr.2020.11.021.
31. Carraro, F. et al. Continuous-Flow Synthesis of ZIF-8 Biocomposites with Tunable Particle Size. *Angewandte Chemie - International Edition* (2020) doi:10.1002/anie.202000678.
32. Zhang, S. & Cheng, Y. Boronic acid-engineered gold nanoparticles for cytosolic protein delivery. *Biomaterials science* (2020) doi:10.1039/d0bm00679c.
33. Zhu, A., Romero, R. & Petty, H. R. Amplex UltraRed enhances the sensitivity of fluorimetric pyruvate detection. *Analytical Biochemistry* (2010) doi:10.1016/j.ab.2010.04.008.

34. Fruk, L., Müller, J. & Niemeyer, C. M. Kinetic analysis of semisynthetic peroxidase enzymes containing a covalent DNA-heme adduct as the cofactor. *Chemistry - A European Journal* (2006) doi:10.1002/chem.200501613.
35. Huang, L., Colas, C. & Ortiz De Montellano, P. R. Oxidation of carboxylic acids by horseradish peroxidase results in prosthetic heme modification and inactivation. *Journal of the American Chemical Society* (2004) doi:10.1021/ja046455w.
36. Cong, L. et al. Multiplex genome engineering using CRISPR/Cas systems. *Science* (2013) doi:10.1126/science.1231143.
37. Mali, P. et al. RNA-guided human genome engineering via Cas9. *Science* (2013) doi:10.1126/science.1232033.
38. Kim, S., Kim, D., Cho, S. W., Kim, J. & Kim, J. S. Highly efficient RNA-guided genome editing in human cells via delivery of purified Cas9 ribonucleoproteins. *Genome Research* (2014) doi:10.1101/gr.171322.113.
39. Lin, Y., Wagner, E. & Lächelt, U. Non-viral delivery of the CRISPR/Cas system: DNA versus RNA versus RNP. *Biomaterials Science Preprint* at <https://doi.org/10.1039/d1bm01658j> (2022).
40. Wang, L. et al. Improving the protein activity and stability under acidic conditions via site-specific conjugation of a pH-responsive polyelectrolyte. *Journal of Materials Chemistry B* (2015) doi:10.1039/c4tb01741b.

41. Ramakrishna, S. et al. Gene disruption by cell-penetrating peptide-mediated delivery of Cas9 protein and guide RNA. *Genome Research* (2014) doi:10.1101/gr.171264.113.

4.6. Supplementary figures

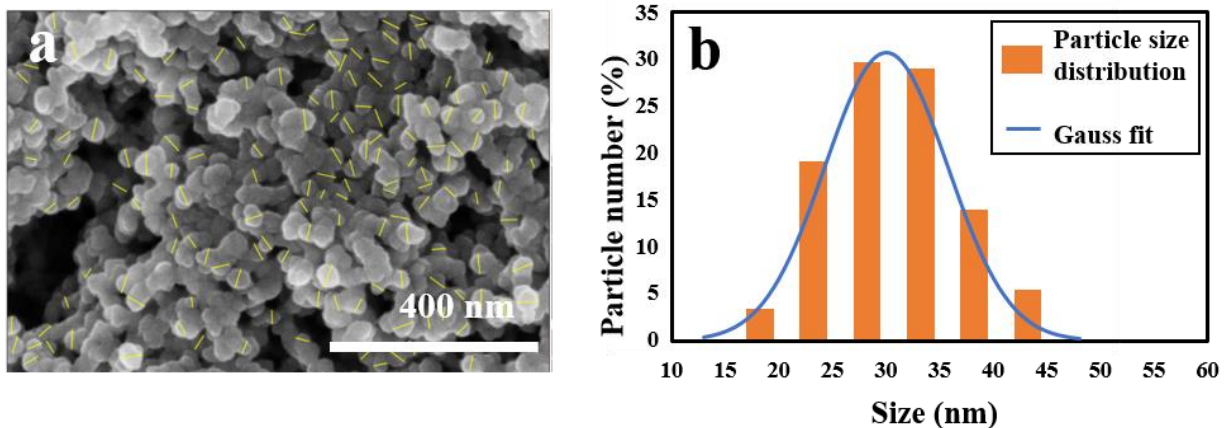


Figure S 4-1. SEM micrograph of Fe-fum NPs (a) and size distribution of Fe-fum NPs obtained from SEM micrographs (b). The particle size distribution was determined by manually measuring the diameter of 152 particles (a, yellow lines). This results in an average particle diameter of ~ 30 nm with a standard deviation of 5.7 nm.

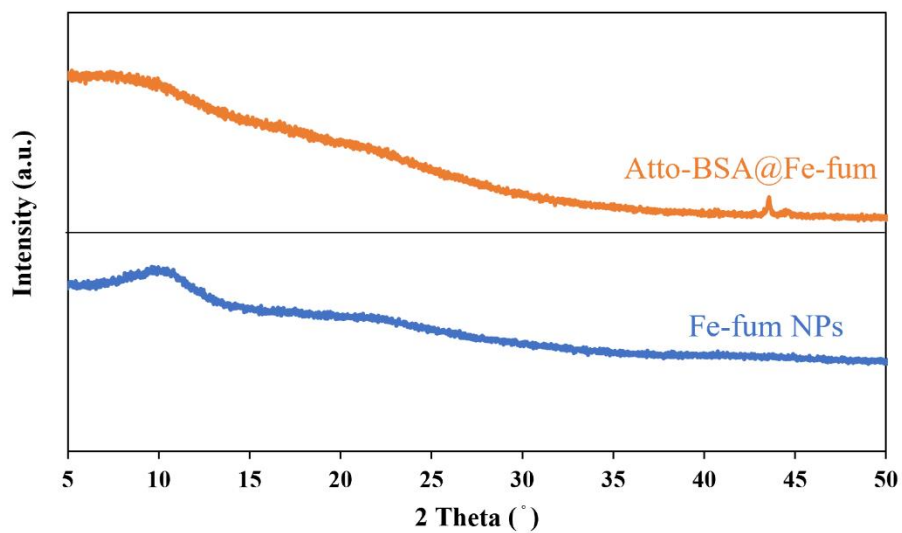


Figure S 4-2. XRD measurements of Fe-fum NPs (blue) and fluorescently labelled BSA biomimetically mineralized into Fe-fum NPs (atto-BSA@Fe-fum; orange).

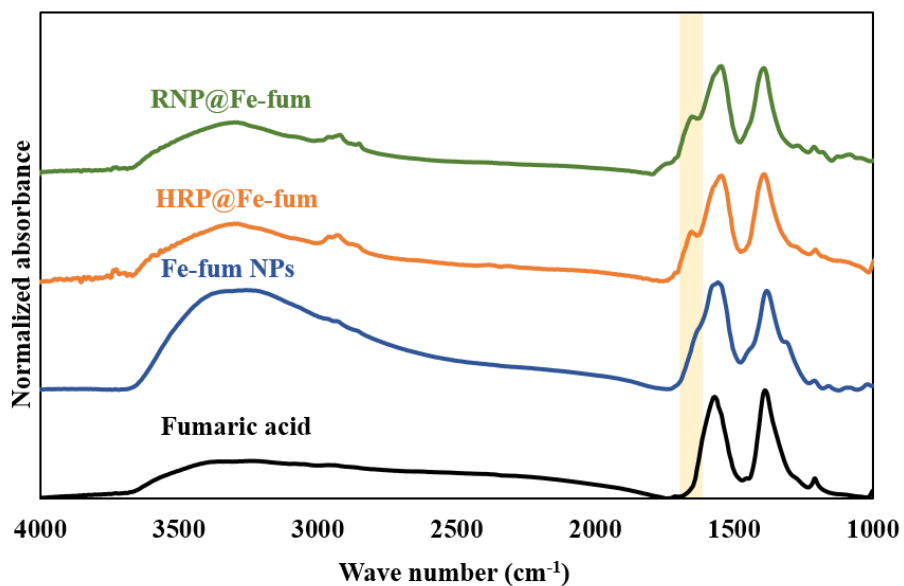


Figure S 4-3. IR spectra of fumaric acid (black), Fe-fum NPs (blue), HRP@Fe-fum (orange) and RNP@Fe-fum (green). Appearance of a peak (marked in yellow) in the range of 1640-1660 cm⁻¹ (corresponding to the amide I band, mainly from C=O stretching vibrations) in the spectra of HRP@Fe-fum and RNP@Fe-fum confirms the successful incorporation of HRP and RNP in the Fe-fum NPs.

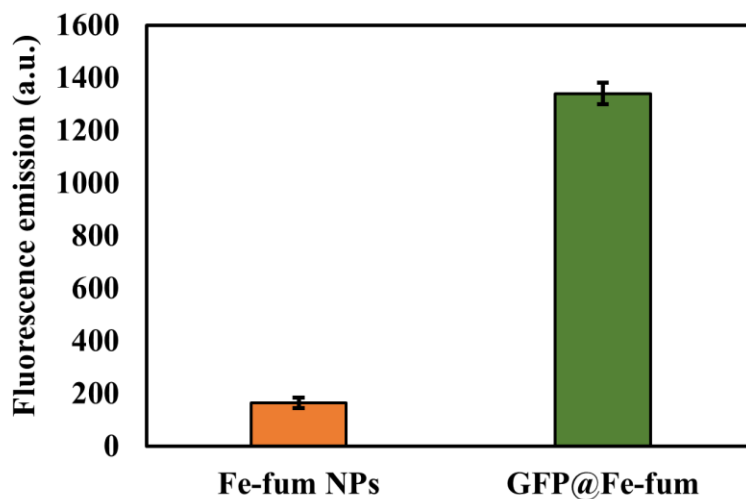


Figure S 4-4. GFP fluorescence emission of degraded Fe-fum NPs synthesized with (green) and without (orange) GFP. GFP fluorescence is preserved during the NP synthesis and ethanol washing steps.

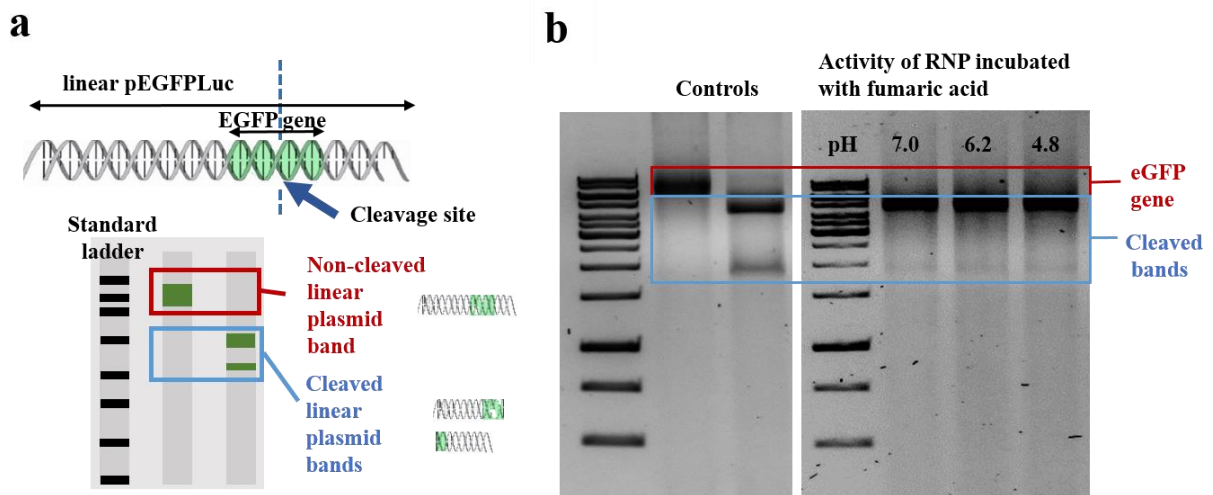


Figure S 4-5. (a) Schematic of the *in vitro* cleavage assay and (b) the bands of the pEGFPLuc plasmid and fragments resulting from cleavage by RNP in an agarose gel.

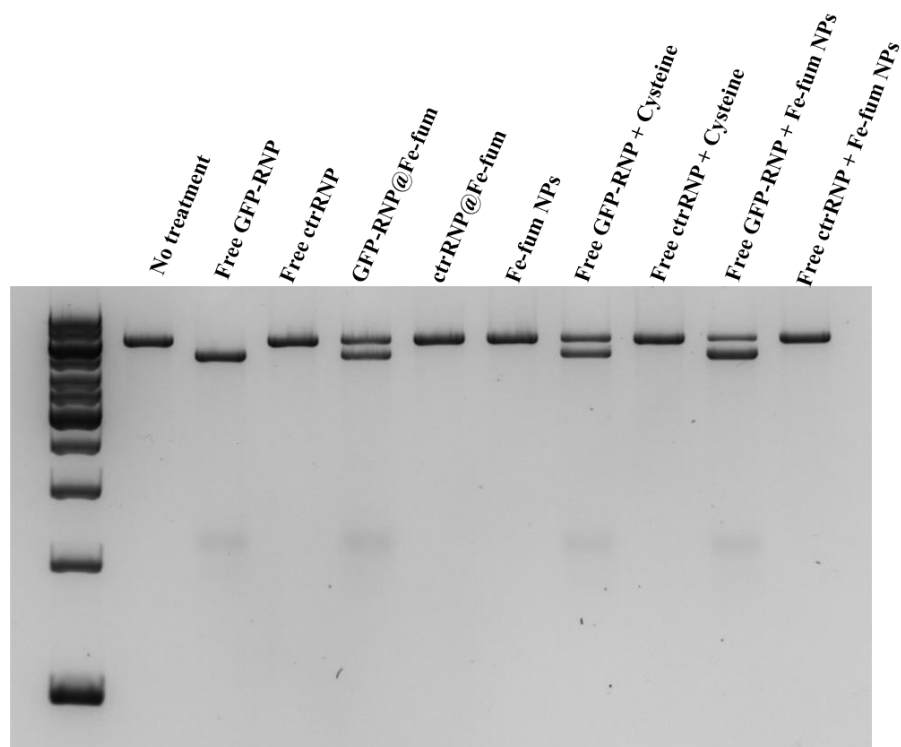


Figure S 4-6. In vitro cleavage assay confirming RNP-activity after Fe-fum NP synthesis. The linear plasmid was treated with free RNP as positive control and with RNP@Fe-fum and Fe-fum NPs both decomposed by a 10 min incubation with cysteine. The effect of cysteine and Fe-fum NPs' ingredients on the activity of RNP was studied by incubation of free RNP with cysteine and decomposed NPs before performing the cleavage assay. As an additional negative control, RNP with control RNA without target sequence in the genome (ctrRNP) was used for each RNP treatment.

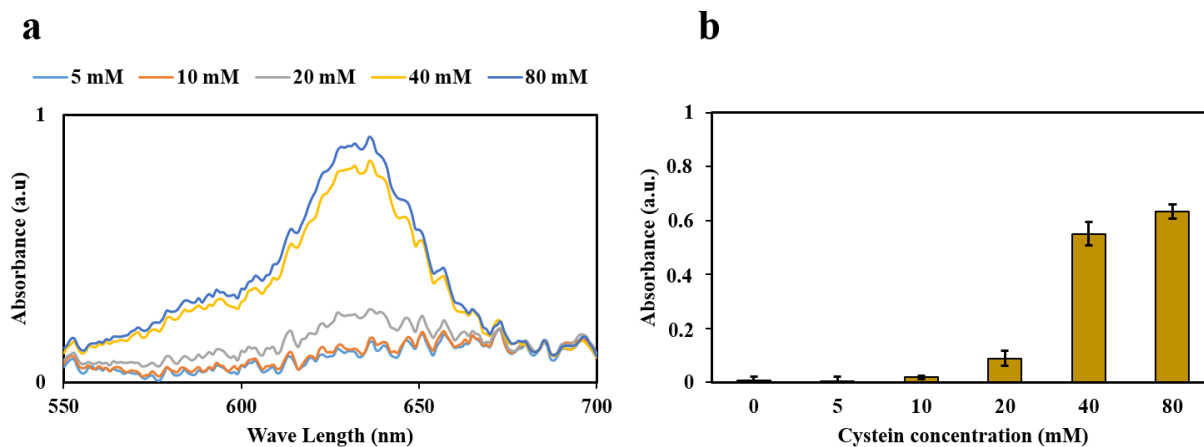


Figure S 4-7. Concentration dependent degradation of Atto633-labeled-HRP@Fe-fum. **(a)** Absorbance spectra of Atto633-labeled-HRP@Fe-fum (supernatant) after treatment with increasing concentrations of cysteine, as indicated by the color code. The absorbance of the supernatant at 633 nm is increasing due to the Atto633-labeled HRP released from the increasingly degraded nanoparticles **(b)** Quantification of the absorbance at 633 nm confirms the increasing degradation with increasing concentration of cysteine.

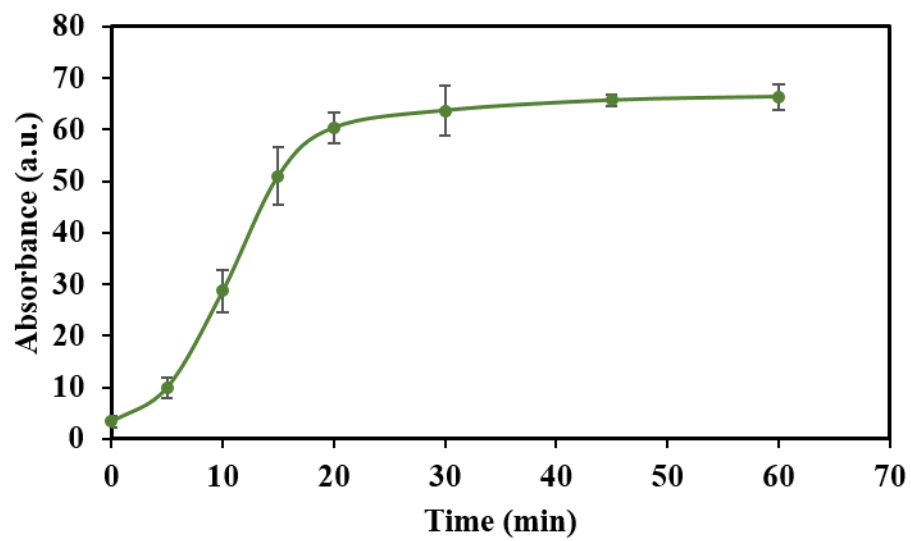


Figure S 4-8. Degradation kinetics of Atto633-labeled HRP@Fe-fum in 20 mM cysteine.

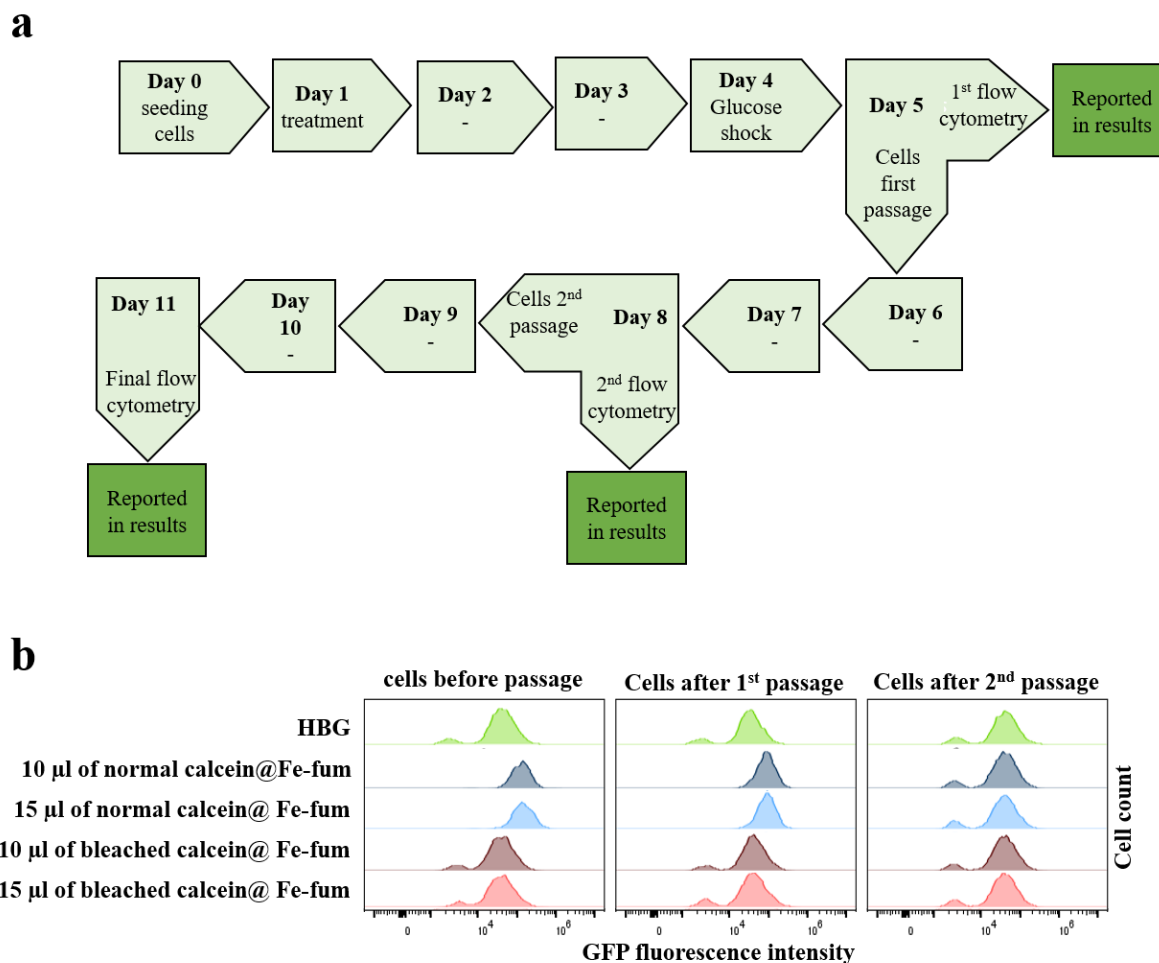


Figure S 4-9. a) Schematic of the steps applied for studying the knockout efficiencies as well as the exclusion of interference with calcein in the GFP channel. **b)** Flow cytometry analysis of GFP fluorescence and calcein interference in *HeLa* cells after sequential splitting of the cells. Stably GFP expressing *HeLa* cells (*HeLa* GFPTub cells) were incubated with lipid-coated Fe-fum NPs loaded with (normal or bleached) calcein (calcein@Fe-fum) and the GFP fluorescence of cells was measured after 5 days (before passage), 8 days (after first passage) and 11 days (after second passage). Cells incubated with HBG buffer only (HBG) served as control. Flow cytometry results confirm that the calcein interference with the GFP signal is negligible after the second splitting.

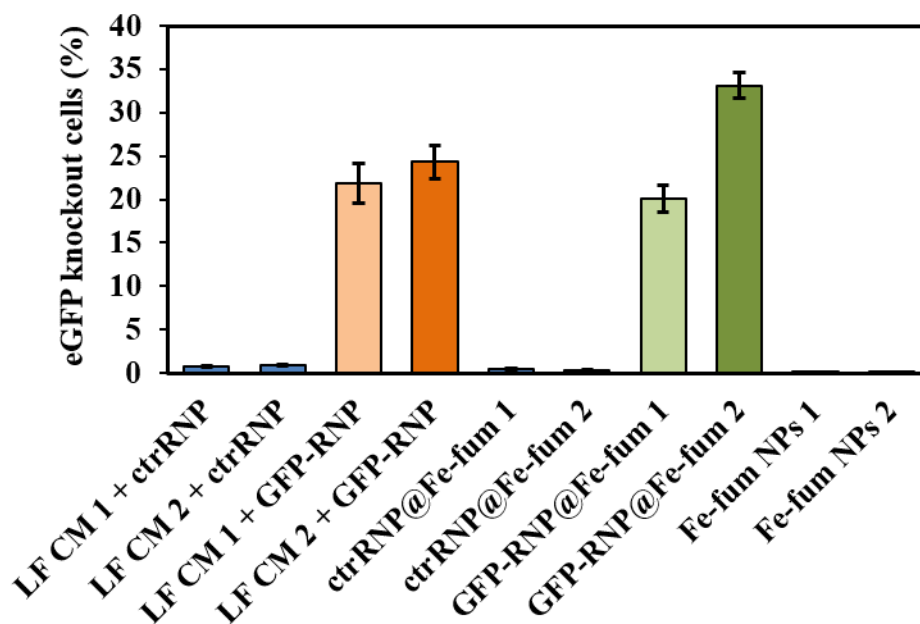


Figure S 4-10. One additional experiment on the knockout efficiency of lipid-coated, calcein-loaded RNP@Fe-fum or Lipofectamine CRISPRMAX (LF CM) containing a control guide RNA without target in the genome (ctrRNP) or GFP-specific guide RNA (GFP-RNP). LF CM1 and Fe-fum 1 correspond to a concentration of 75 nM RNP, LF CM2 and Fe-fum 2 to a concentration of 110 nM RNP. The experiment confirms the specificity of the GFP knockout.

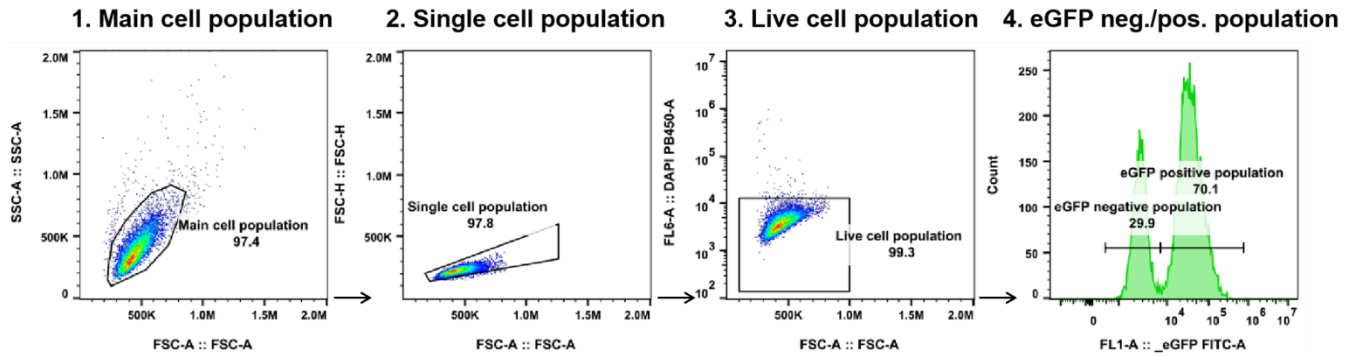


Figure S 4-11. FACS gating strategy for experiments shown in Fig. 5 and Fig. S10. Briefly, 1) Forward versus side scatter (FSC-A vs SSC-A) gating is used to identify cell population of interest and exclude cell debris. (2) A forward scatter height (FSC-H) vs. forward scatter area (FSC-A) density plot is used to exclude doublet cells. (3) A forward scatter area (FSC-A) vs. DAPI area (DAPI-A) density plot is used to identify live cells. (4) eGFP single parameter histogram is used for identifying eGFP negative and positive cell population.

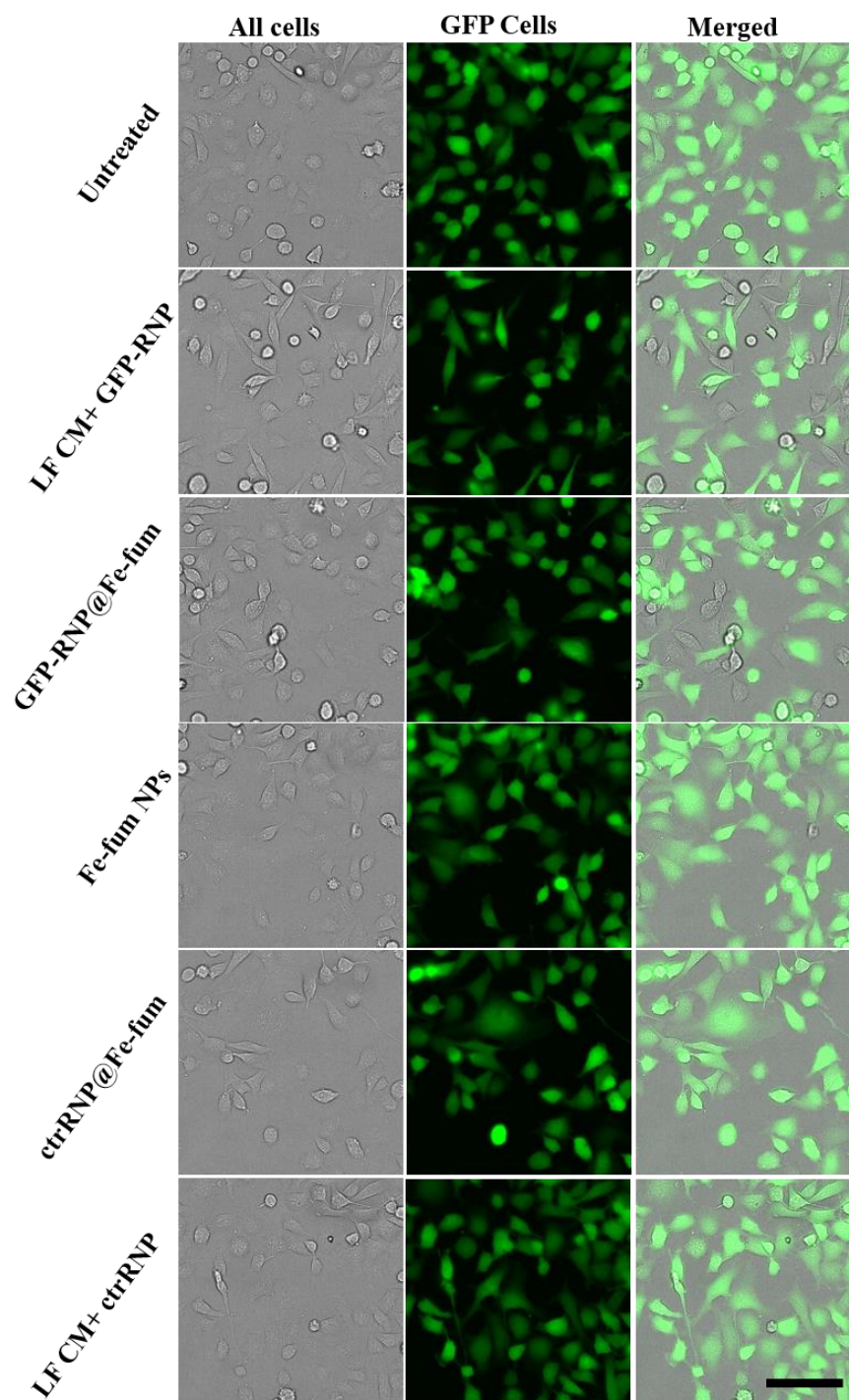


Figure S 4-12. Fluorescence and brightfield high-content microscopy of *HeLa* GFPTub cells after treatment with GFP-RNP@Fe-fum, LF CM+GFP-RNP or controls. The experiment confirms the specific GFP knockout as determined by FACS in Fig. S10. Scale bar: 100 μ m.

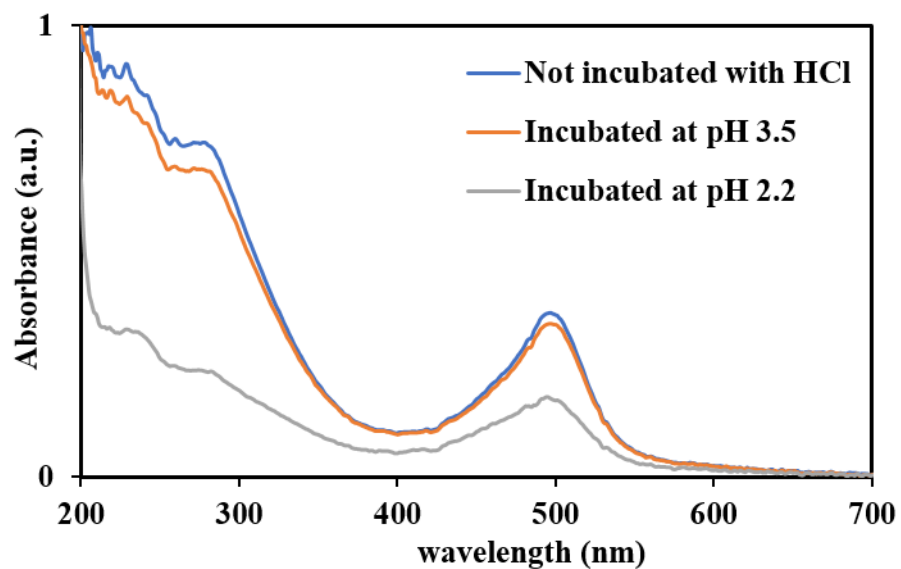


Figure S 4-13. Absorbance of lipid-coated Fe-fum NPs after incubation at pH 2.2 and 3.5 overnight. The similarity of the spectra of Fe-fum NPs incubated at pH 3.5 and of Fe-fum NPs that were not incubated with HCl confirms the stability of Fe-fum NPs in acidic condition down to pH 3.5. The intensity changes in the spectrum of Fe-fum NPs incubated at pH 2.2 suggest their partial degradation at this low pH.

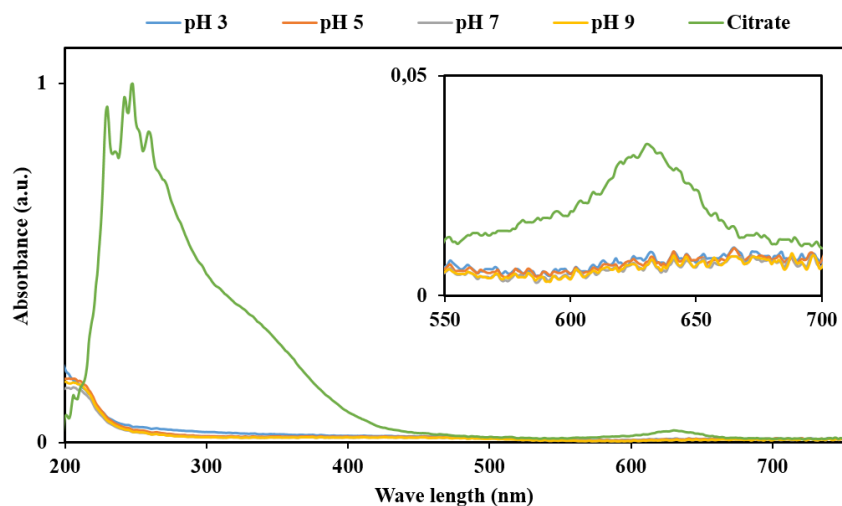


Figure S 4-14. Absorbance of the supernatant of Atto633-HRP@Fe-fum NPs after incubation at the indicated pH values, as well as in citrate solution. No increase in absorbance at 633 nm is detected after incubation within the range between pH 3-9 indicating that the NPs do not degrade and release Atto633-labeled HRP into the supernatant. In the case of citrate, NPs are degraded and release Atto633-labeled HRP into the supernatant leading to an increase in absorbance at 633 nm.

CHAPTER 5

Intracellular Delivery of mRNA

by Iron-Fumarate Nanoparticles

5. Intracellular delivery of mRNA by iron-fumarate nanoparticles

Abstract

In the rapidly progressing landscape of medicine and biotechnology, RNA technologies have emerged as transformative tools, offering new avenues for therapeutic and research applications. However, significant challenges hinder the effective delivery of such biomolecules into target cells, underscoring the critical need for the development of carrier systems that safeguard RNA from degradation and promote efficient cellular uptake.

In this study, we explored the use of iron fumarate nanoparticles (Fe-fum NPs) as potential carriers for RNA, particularly mRNA delivery. By applying a biomineralization technique for synthesis, our results demonstrated the successful incorporation of RNA molecules into the NPs, followed by efficient delivery into cells. To induce endosomal escape, we applied a glucose shock strategy. Furthermore, the effectiveness of our approach was validated using mCherry-encoding mRNA as model RNA, which resulted in the successful production of mCherry protein within the cells, indicating successful delivery of intact mRNA and translation.

These findings underscore the potential of Fe-fum NPs as an effective carrier for RNA molecules, contributing to the advancement of RNA-based therapeutic and biotechnological applications.

5.1. Introduction

Recent major breakthroughs have started to reveal the enormous potential of RNA-based therapeutics. The basis for this success was a very good understanding of mRNA biology and the development of suitable delivery systems¹⁻³. RNA is a fragile biomolecule that is prone to degradation via hydrolysis and enzymes⁴⁻⁶. Furthermore, its cellular internalization is not sufficiently efficient for therapeutic and biotechnological applications^{7,8}. An RNA-delivery system, therefore, has to 1) show high encapsulation efficiency of the RNA, 2) protect RNA from degradation, 3) internalize it efficiently into the targeted cells, and 4) escape endosomal entrapment and release the RNA into the cytosol⁹⁻¹¹.

Current delivery systems are mainly based on lipid nanoparticles, which fulfill these criteria¹¹⁻¹³. However, their protection of RNA is limited^{14,15}. This leads to complicated storage processes, e.g., deep freezing, with high environmental impact and the necessity of molecular stabilization of the RNA^{16,17}. However, not all therapeutic RNA can be sufficiently stabilized. Other types of nanoparticles have also been suggested for RNA delivery systems, including polymer-based nanoparticles like chitosan¹⁸⁻²⁰, inorganic materials such as gold and silica nanoparticles^{21,22}, and metal-organic frameworks²³⁻²⁵. Most of these systems are limited in their ability to protect RNA, though, since the RNA is still accessible for nucleases and hydrolysis²⁶. Furthermore, due to the large size of RNA, and specifically mRNA, compared to the pore size of the nanoparticles, the loading efficiency of porous nanoparticles is limited – sometimes even to adsorption on the particle surface only³. Hence, the efficacy of mRNA delivery hinges on technologies capable of effectively encapsulating large polynucleotides for transporting to the cytoplasm²⁷.

Recently, a biomimetic mineralization technique has been introduced to overcome the limits of loading efficiency and protection²⁸. In this approach, nanoparticles are synthesized around the biomolecule to overcome the limitations of pore size²⁹. They also show very good protective properties, preventing degradation in harsh conditions, such as organic solvents and boiling temperatures³⁰. While this strategy has been designed for the synthesis of crystalline metal-organic-framework nanoparticles, we recently introduced amorphous iron-fumarate nanoparticles synthesized at room temperature under biomolecule-preserving conditions via this technique. We could show that it allows for comparatively high loading capacities, delivery, and efficient protection of proteins and complexes of protein and RNA, namely Cas9/sgRNA complexes³¹. Here, we employ the biomimetic mineralization technique to integrate mRNA into iron-fumarate nanoparticles. Our findings demonstrate their capability to facilitate intracellular mRNA delivery and subsequent protein expression.

5.2. Results

We prepared mRNA-loaded iron-fumarate nanoparticles (RNA@Fe-fum) via our previously introduced synthesis³¹. Briefly, RNA was incubated with fumaric acid at pH 4.8, which was verified not to degrade the RNA³². Subsequent addition of iron chloride induces nanoparticle formation around the RNA molecules. The obtained nanoparticles were observed by scanning electron microscopy (SEM) and confirmed to have a spherical morphology (**Figure S 5-1**). There was no visible difference in SEM images of RNA@Fe-fum and iron-fumarate nanoparticles without mRNA (Fe-fum). Dynamic light scattering (DLS) results show a bimodal distribution, which is very similar for mRNA@Fe-fum and Fe-fum (**Figure 5-1a**). The hydrodynamic radius of the main fraction is approximately 90 nm. The second fraction with a hydrodynamic radius of

ca. 400 nm might arise from partial aggregation of the nanoparticles. The zeta potential of mRNA@Fe-fum and Fe-fum is also very similar, approximately 14 mV, as measured in water (pH 6) and shown in **Figure 5-1b**. This suggests that the mRNA-loading does not influence the properties of the nanoparticle and that it is not merely adsorbed to their surface since that would change the zeta potential.

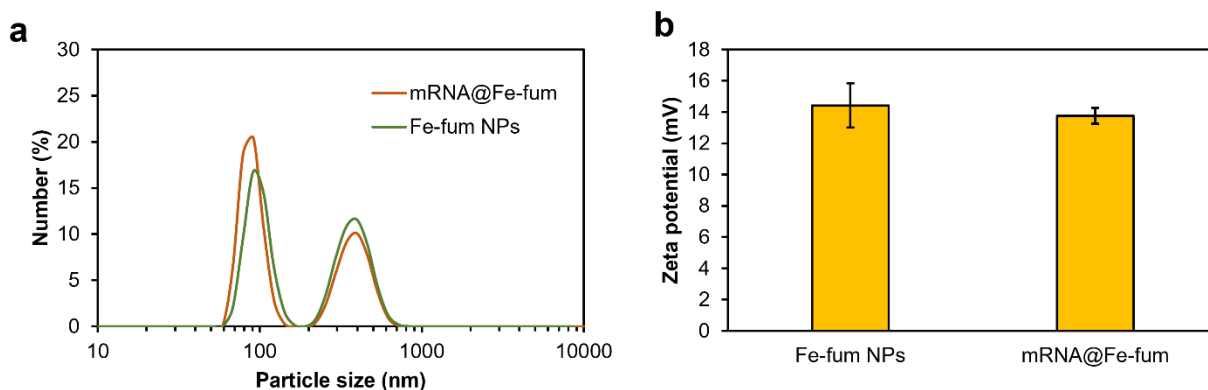


Figure 5-1. Characterization of the iron fumarate nanoparticles (Fe-fum NPs) and mRNA loaded Fe-fum (mRNA@Fe-fum). (a) Size distribution obtained via dynamic light scattering (DLS) measurements. (b) ζ potential of nanoparticles dispersed in water. The measurements were performed before any modification.

The effect of the synthesis on the RNA was tested after each step via gel electrophoresis. The RNA was intact after each synthesis step of the nanoparticles, as shown by its distinct band in **Figure 5-2**.

Gel electrophoresis of mRNA@Fe-fum degraded with EDTA was also used to calculate the amount of intact mRNA incorporated into the nanoparticles. The loading efficiency was calculated

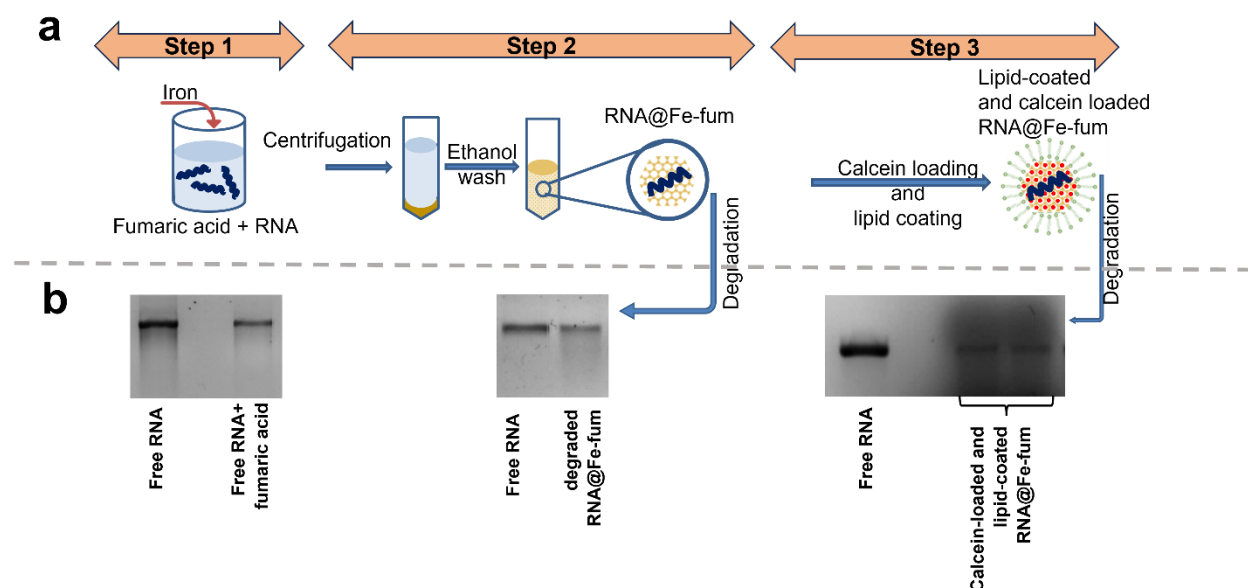


Figure 5-2. Compatibility of iron fumarate nanoparticles (Fe-fum NPs) synthesis process with RNA. (a) Schematic of Fe-fum NPs' synthesis in the presence of RNA and the subsequent calcein loading and lipid coating processes. (b) gel electrophoresis images showing the structural integrity of RNA molecules in different steps of Fe-fum NPs' synthesis. Free RNA is used as a control. The appearance of the RNA band at the same position as free RNA confirms the preservation of the structural integrity of the incorporated RNA.

as the percentage of mRNA incorporated in mRNA@Fe-fum relative to the total initial mRNA used for the synthesis. For the initial amounts of mRNA used in 5.5 mL of synthesis reaction volume, the loading efficiency was approximately 14% for 2 μ g of mRNA and increased to around 50% for 4 and 8 μ g of mRNA. The loading capacity was calculated as the weight ratio of the encapsulated mRNA over the mRNA@Fe-fum. It increased with an increasing amount of mRNA from 0.04% for 2 μ g mRNA to 0.66 % for 8 μ g mRNA (Figure S 5-3). A recent study by Lawson et al. reported around 6% loading capacity of GFP-mRNA using ZIF-8 nanoparticles with a synthesis reaction volume containing 100 μ g of mRNA per mL. Compared to these findings, the Fe-fum system shows a lower loading capacity for mRNA, which could be attributed to differences

in the structural and chemical characteristics of the carriers, as well as the considerably lower mRNA concentration used in our experiments. Interestingly, our previous work with ribonucleoproteins (RNPs) showed a higher loading capacity in Fe-fum compared to ZIF-8, indicating that while Fe-fum is highly effective for ribonucleoproteins, the encapsulation of mRNA might require further optimization. The observed increase in loading capacity with higher mRNA amounts in our study suggests the potential for improvement, possibly through adjustments in the formulation process of Fe-fum NPs, to enhance the loading capacity for mRNA. The table below highlights the relative loading capacities and efficiencies of different nanoparticle systems for mRNA delivery.

Table 5-1. Comparison of Loading Capacities of Different Nanoparticles for mRNA

Nanoparticle system	Loading Capacity	Loading Efficiency	Reference
mRNA@Fe-fum	0.04% - 0.66%	14% - 50%	our study
mRNA@ ZIF-8	~6%	~90%	33
Polymer-based NPs	~11	~73%	34
Lipid-based NPs	Not specified	~95%	35

For cellular internalization and visualization, the RNA@Fe-fum were loaded with the dye calcein and coated with DOPC-liposomes as previously described ³¹. Gel electrophoresis shows that calcein loading leads to a certain extent of partial mRNA degradation, but otherwise, the RNA integrity is maintained (**Figure 5-2**, step 3).

Next, we confirmed that the RNA was internalized into cells via the nanoparticles. To this end, we incorporated RNA labeled with Atto633 into Fe-fums (Atto633RNA@Fe-fum) and incubated the lipid-coated, calcein-loaded Atto633RNA@Fe-fum on *HeLa* cells. After 72 h of incubation, we observed colocalization of the Atto633-labeled RNA and the Fe-fum visualized by the loaded calcein (**Figure 5-3**).

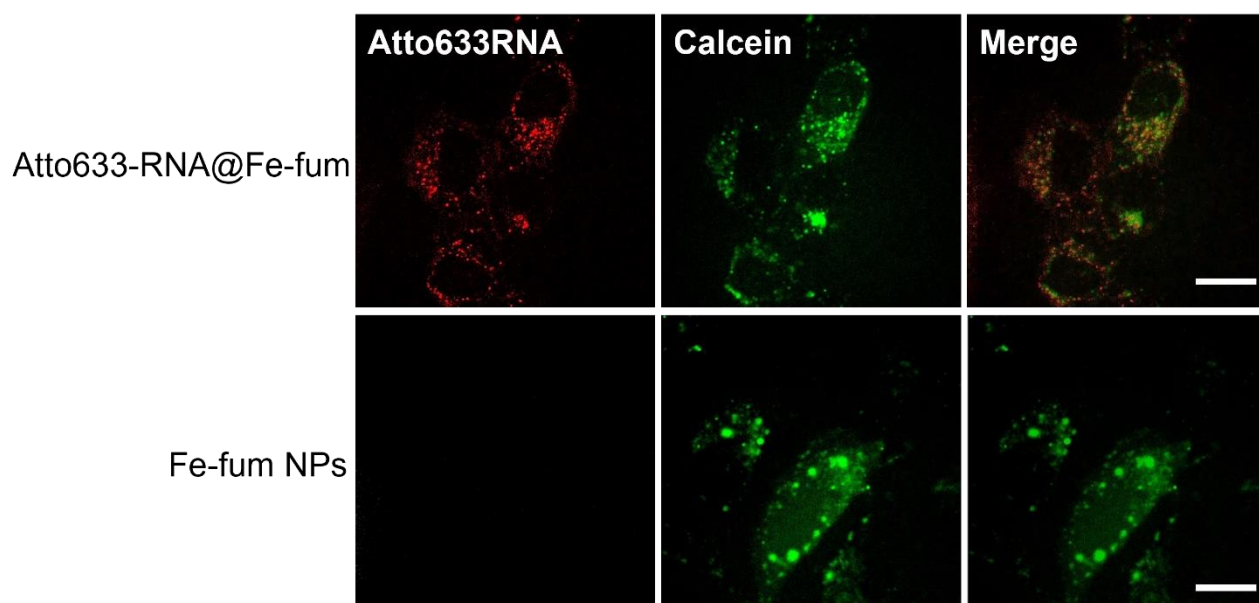


Figure 5-3. Intracellular delivery of RNA via iron fumarate (Fe-fum NPs). Confocal microscopy images of *HeLa* cells treated with lipid-coated and calcein-loaded RNA@Fe-fum for three days. Colocalization of the RNA fluorescently labeled with Atto633 (red) and the Fe-fum visualized by the loaded calcein (green) confirms the intracellular RNA delivery facilitated by Fe-fum NPs. The scale bar is 20 μm .

To observe whether the Fe-fum are able to deliver and release functional mRNA into the cytosol of cells, we incorporated mRNA encoding the fluorescent protein mCherry into the Fe-fum. Three days after incubation, very few cells with mCherry signal were found. Similarly, very few cells with released calcein were found. This is in accordance with our previous finding that unmodified Fe-fum do not trigger sufficient endosomal escape. We, therefore, applied a glucose shock to

induce endosomal escape externally. Indeed, we found released calcein and mCherry expression in cells 8 h after glucose shock, as shown in **Figure 5-4**. Control experiments using bleached calcein and Fe-fum without mRNA confirm that the mCherry signal is due to the delivery of the mRNA. Using bleached calcein confirmed that the red signal is not associated with the bleed-through of the green signal into the red channel and the mCherry signal is solely due to the production of mCherry.

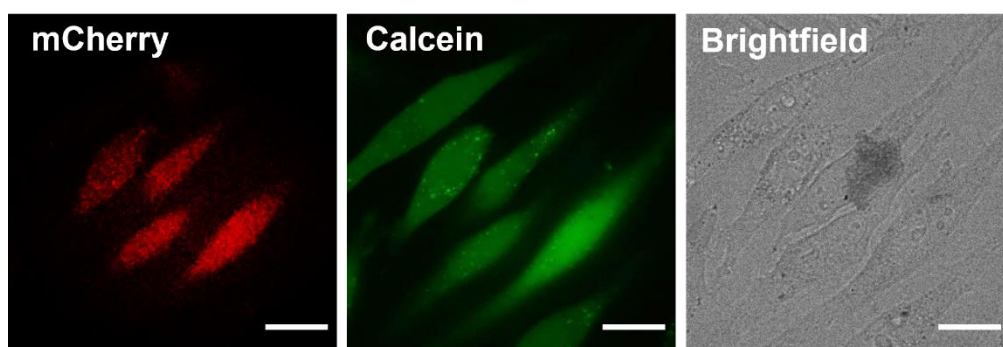


Figure 5-4. mCherry expression of *HeLa* cells transfected with mRNA-loaded iron fumarate nanoparticles (mRNA@Fe-fum). *HeLa* cells were treated with lipid-coated and calcein-loaded mRNA@Fe-fum for three days followed by glucose shock 8 hours before imaging. The uniform cytosolic fluorescent signal in the red channel represents the mCherry production mediated by mRNA. The scale bar is 20 μm .

Heretofore, we demonstrate the capacity for efficient loading of RNA into Fe-fum NPs and delivery of functional RNA molecules into cells. Our previous research has indicated that Fe-fum NPs offer protection to protein cargo against harsh conditions, suggesting a potentially similar protective effect for mRNA³¹. Our preliminary studies have indicated partial protection of mRNA against RNase degradation by Fe-fum NPs, though these experiments require further optimization. While additional exploration is necessary, our findings lay the groundwork for future investigations into the protective potential of Fe-fum NPs in safeguarding mRNA, highlighting the promising prospects for RNA delivery using these nanoparticles.

5.3. Conclusion

To sum up, we have shown that Fe-fum are able to incorporate mRNA with a loading efficiency of up to 50% and deliver it to cells. mRNA can be released from the endosome by a glucose shock, allowing for controlled delivery of mRNA to cells. While additional research is required to fully explore their protective potential for mRNA cargo, our findings lay a promising foundation for future investigations in this area.

5.4. Materials and methods

5.4.1. Synthesis

Chemicals

Chemicals were purchased from Sigma Aldrich (St. Louis, MO, USA), if not stated otherwise.

Biomimetic mineralization of RNA@Fe-fum

5 mL of a 10 mM solution of fumaric acid in RNase-free water was prepared, and the pH of the solution was adjusted to 4.8 by adding NaOH. RNA samples, comprising a 667-nucleotide RNA labeled with Atto633 (Atto633RNA) or mCherry-encoding mRNA (OZ BIOSCIENCES, Catalog number: #MRNA8), were introduced into a fumaric acid solution yielding concentrations ranging from 0.2 to 1.6 $\mu\text{g/mL}$. The mixture was incubated for 10 min at room temperature and 750 rpm stirring. A separate solution of iron chloride in RNase-free water (10 mM, 500 μL) was prepared. Then, the iron chloride solution was added to the fumaric acid and RNA mixture in 5 steps at 20 s intervals. The resulting RNA@Fe-fum was washed three times by centrifugation and subsequent redispersion in 500 μL ethanol. During the synthesis, RNase-free tips and tubes were used, and RNA-containing samples were kept on ice when possible.

Calcein loading

A 1 mM solution of calcein in RNase-free water was prepared. 350 μ L of Fe-fum NPs or RNA@Fe-fum was redispersed in 1 mL of calcein solution. The mixture was then incubated for one hour at 700 rpm, shaking at 4 °C for loading. Then, the nanoparticles were centrifuged for 5 min at 14000 rpm, and the supernatant was discarded to collect the Fe-fum NPs for lipid coating.

Lipid coating

The lipid coating of the Fe-fum NPs was performed via a fusion method. First, a liposome coating solution was prepared by extruding a 1 mg/mL PBS solution of DOPC (1,2-dioleoyl-sn-glycero-3-phosphocholine, Avanti) through an extruder with a 100 nm pore-sized membrane 11 times. Then, the pellet of the calcein-loaded nanoparticles was redispersed in 250 μ L of liposome solution, followed by the addition of 250 μ L of RNase-free water and incubation for 2 hours. The particles were then centrifuged (5 min at 14000 rpm) and redispersed in 250 μ L PBS. All cell experiments were performed with lipid-coated, calcein-loaded nanoparticles.

5.4.2. Characteristic methods

Dynamic Light Scattering (DLS)

DLS and zeta potential measurements were performed by applying a Zetasizer Nano Series (Nano-ZS, Malvern) equipped with a laser with the wavelength $\lambda = 633$ nm. DLS measurements were performed at 25 °C and by using PMMA cuvettes. Samples for DLS measurements were prepared by diluting the freshly produced NPs or lipid-coated NPs in ethanol or PBS, respectively. Samples in water were used for the single-point measurements of the NPs' zeta potential by using DTS107 cuvettes.

X-ray diffraction (XRD)

XRD experiments were performed on dried Fe-fum NPs. The samples were measured on an STOE Diffractometer System STADI P operating in transmission mode. The setup uses Cu K α 1-radiation with a wavelength $\lambda = 0.15418$ nm.

Confocal microscopy

Fluorescence images were captured using a Zeiss Observer SD spinning disk confocal microscope equipped with a Yokogawa CSU-X1 spinning disc unit and an oil objective featuring 63x magnification (1.40 N.A.). The green channel (BP 525/50) and red channel (BP 629/62) were employed with excitation provided by 488 nm and 561 nm lasers, respectively. Subsequently, the acquired images were analyzed using ImageJ v2.35 software for processing.

Cell culture

HeLa cells (a human cervical carcinoma cell line) were cultivated in Dulbecco's modified Eagle's medium (DMEM, Gibco, USA) with 10% (v/v) fetal bovine serum (FBS, Gibco, USA) and 1% (v/v) penicillin-streptomycin (Gibco, USA). Cells were grown in a cell culture incubator (Hera Cell) at 37 °C with 5% carbon dioxide.

Cell viability assay (MTT assay)

The cytotoxicity of the lipid-coated, calcein-loaded mRNA@Fe-fum was studied using an MTT assay (Thermo Fisher, USA). *HeLa* cells were plated in 96-well plates at a density of 5000 cells per well and 200 μ L DMEM. After 24 hours of incubation, the cells were treated with 7 μ L of lipid-coated, calcein-loaded Fe-fum NPs with or without mRNA loading and cells without

treatment were used as a control group. Following a 72-hour incubation, the MTT assay was conducted. In this procedure, the cells were rinsed twice with PBS and subsequently incubated for 2 hours in DMEM containing 500 µg/mL MTT (3-(4,5-dimethylthiazol-2-yl)-2,5-diphenyltetrazolium bromide) within the incubator (37 °C, 5% carbon dioxide). Next, the supernatant was removed, and the cells were lysed by subjecting the plate to an incubation at -80 °C for a minimum of 20 minutes. Subsequently, the resulting purple crystals were dissolved in 100 µL of DMSO per well and the absorption at 590 nm was measured using a SpectraFluor™ Plus microplate reader S4 (Tecan, Groeding, Austria). Cell viability was determined by comparing the absorbance of wells containing treated cells to that of wells with untreated control cells, and the ratio was calculated accordingly. The MTT assay was conducted with two biological replicates, and each treatment was performed in quadruplicate.

RNA integrity assay by gel electrophoresis

A 2 % (w/v) agarose gel was prepared in TBE buffer (Tris/borate/EDTA) supplemented with a 1:1000 dilution of GelRed® Nucleic Acid Gel Stain (Biotium, Catalog number: 41003). A mixture of formamide and DNA Gel loading buffer 6X (Thermo Scientific™, Catalog number: R0611) at a volume ratio of 19 to 1 was prepared. RNA-containing samples were mixed with 10 µL of the formamide mixture, subsequently being heat denatured by incubation at 70 °C for 5 minutes. An additional 2.5 µL of DNA Gel loading buffer 6X was added to the samples prior to loading into the agarose gel. After loading the samples, electrophoresis was carried out at 100 V in 1X TBE buffer for 40 minutes. Subsequently, the RNA/mRNA bands were visualized using a UV illuminator.

Compatibility of NPs' synthesis process with RNA

The compatibility of the synthesis process of the Fe-fum NPs for the RNA molecules was confirmed by performing a gel electrophoresis assay (as described above). The structural integrity of the RNA samples was assessed at different points of the synthesis process: incubation with fumaric acid, after the formation of Fe-fum NPs (before any modification), and after liposome coating (final product used for cellular experiments). To induce a release of the encapsulated RNA, the RNA@Fe-fum before or after liposome coating were centrifuged at 14000 rpm for 5 minutes, and the pellets were decomposed by using a 0.1 M solution of EDTA and incubated for 10 minutes at room temperature. Free RNA was used as a control of intact samples.

Loading efficiency and capacity of mRNA in the Fe-fum NPs

Fe-fum NPs were synthesized in the presence of 2, 4, and 8 μg of mCherry-encoding mRNA, yielding concentrations of 0.4, 0.8, and 1.6 $\mu\text{g}/\text{mL}$, respectively. The mRNA@Fe-fum was then degraded by using EDTA 0.1 M to release the encapsulated mRNA and the samples were run on an agarose gel. Three discrete quantities of free mRNA (0.25 μg , 0.5 μg , and 1 μg) served as positive controls to confirm the presence of intact mRNA and to establish a standard curve correlating mRNA mass with the intensity of the gel band formed on the agarose gel. The intensity of the bands was analyzed using ImageJ v2.35 software.

The mass of the encapsulated mRNA in the Fe-fum NPs was estimated by analyzing the band's intensity and aligning it with the established standard curve. Then, the mRNA loading efficiency was calculated as the percentage of mRNA encapsulated in Fe-fum NPs relative to the total initial

mRNA used for synthesis, and the loading capacity was quantified as the weight ratio of the encapsulated mRNA per μg of Fe-fum NPs.

$$\text{Encapsulation efficiency} = \frac{\text{encapsulated mRNA}}{\text{Initial mRNA}} * 100$$

$$\text{Encapsulation capacity} = \frac{\text{Mass of encapsulated mRNA}}{\text{Mass of nanoparticles}} * 100$$

Intracellular activity of mCherry encoding mRNA

For the *in vitro* transfection study, *HeLa* cells were split one day prior to transfection and seeded at a density of 5000 cells per well into an 8-well microscopy slide (ibidi). The next day, the cells were treated with 10 μL of mRNA@Fe-fum or mRNA@Fe-fum for three days. Negative control samples included untreated cells and cells treated with Fe-fum NPs without mRNA. After three days, the cells were treated with a solution of 1 M glucose in DMEM for 6 minutes to induce the endosomal escape. The cells were then washed twice with PBS to remove the glucose completely and then fresh DMEM was added to the cells for another 8 hours.

5.5. References

1. Shin, H. et al. Recent Advances in RNA Therapeutics and RNA Delivery Systems Based on Nanoparticles. *Adv Ther (Weinh)* 1, 1–27 (2018).
2. Vavilis, T. et al. mRNA in the Context of Protein Replacement Therapy. *Pharmaceutics* vol. 15 Preprint at <https://doi.org/10.3390/pharmaceutics15010166> (2023).
3. Dowdy, S. F. Overcoming cellular barriers for RNA therapeutics. *Nature Biotechnology* vol. 35 222–229 Preprint at <https://doi.org/10.1038/nbt.3802> (2017).
4. Huang, Y. et al. Elimination pathways of systemically delivered siRNA. *Molecular Therapy* 19, 381–385 (2011).
5. Xian, H., Zhang, Y., Yu, C. & Wang, Y. Nanobiotechnology-Enabled mRNA Stabilization. *Pharmaceutics* vol. 15 Preprint at <https://doi.org/10.3390/pharmaceutics15020620> (2023).
6. Yan, Y. et al. Non-viral vectors for RNA delivery. *Journal of Controlled Release* 342, 241–279 (2022).
7. Juliano, R. L. & Carver, K. Cellular uptake and intracellular trafficking of oligonucleotides. *Advanced Drug Delivery Reviews* vol. 87 35–45 Preprint at <https://doi.org/10.1016/j.addr.2015.04.005> (2015).
8. Sahu, I., Haque, A. K. M. A., Weidensee, B., Weinmann, P. & Kormann, M. S. D. Recent Developments in mRNA-Based Protein Supplementation Therapy to Target Lung Diseases. *Molecular Therapy* vol. 27 803–823 Preprint at <https://doi.org/10.1016/j.ymthe.2019.02.019> (2019).

9. Wu, Z. & Li, T. Nanoparticle-Mediated Cytoplasmic Delivery of Messenger RNA Vaccines: Challenges and Future Perspectives. *Pharm Res* 38, 473–478 (2021).
10. Zong, Y., Lin, Y., Wei, T. & Cheng, Q. Lipid Nanoparticle (LNP) Enables mRNA Delivery for Cancer Therapy. *Advanced Materials* (2023) doi:10.1002/adma.202303261.
11. Tenchov, R., Bird, R., Curtze, A. E. & Zhou, Q. Lipid Nanoparticles from Liposomes to mRNA Vaccine Delivery, a Landscape of Research Diversity and Advancement. *ACS Nano* vol. 15 16982–17015 Preprint at <https://doi.org/10.1021/acsnano.1c04996> (2021).
12. Zhang, W. et al. Lipid carriers for mRNA delivery. *Acta Pharmaceutica Sinica B* vol. 13 4105–4126 Preprint at <https://doi.org/10.1016/j.apsb.2022.11.026> (2023).
13. Pontes, A. P. et al. A poly(amidoamine)-based polymeric nanoparticle platform for efficient in vivo delivery of mRNA. *Biomaterials Advances* 156, (2024).
14. DeLong, R. K. et al. Enhancing RNA Payload and Temperature Stability and Activity with Cationic Peptide-Coated Zinc Oxide Nanoparticles. *ACS Pharmacol Transl Sci* 7, 707–715 (2024).
15. Packer, M., Gyawali, D., Yerabolu, R., Schariter, J. & White, P. A novel mechanism for the loss of mRNA activity in lipid nanoparticle delivery systems. *Nat Commun* 12, (2021).
16. Choe, J. A., Brinkman, H. M., Lee, J. S. & Murphy, W. L. Optimized biomimetic minerals maintain activity of mRNA complexes after long term storage. *Acta Biomater* 174, 428–436 (2024).
17. Zhao, P. et al. Long-term storage of lipid-like nanoparticles for mRNA delivery. *Bioact Mater* 5, 358–363 (2020).

18. Dammes, N. & Peer, D. Paving the Road for RNA Therapeutics. Trends in Pharmacological Sciences Preprint at <https://doi.org/10.1016/j.tips.2020.08.004> (2020).
19. Byun, M. J. et al. Advances in Nanoparticles for Effective Delivery of RNA Therapeutics. Biochip Journal Preprint at <https://doi.org/10.1007/s13206-022-00052-5> (2022).
20. Cao, Y., Tan, Y. F., Wong, Y. S., Liew, M. W. J. & Venkatraman, S. Recent advances in chitosan-based carriers for gene delivery. Marine Drugs vol. 17 Preprint at <https://doi.org/10.3390/md17060381> (2019).
21. Janjua, T. I. et al. Silica nanoparticles: A review of their safety and current strategies to overcome biological barriers. Adv Drug Deliv Rev 115115 (2023) doi:10.1016/j.addr.2023.115115.
22. Luther, D. C. et al. Delivery of drugs, proteins, and nucleic acids using inorganic nanoparticles. Advanced Drug Delivery Reviews vol. 156 188–213 Preprint at <https://doi.org/10.1016/j.addr.2020.06.020> (2020).
23. Qiu, G.-H. et al. Synchronous detection of ebolavirus conserved RNA sequences and ebolavirus-encoded miRNA-like fragment based on a zwitterionic copper (II) metal–organic framework. Talanta 180, 396–402 (2018).
24. Teplensky, M. H. et al. A Highly Porous Metal-Organic Framework System to Deliver Payloads for Gene Knockdown. Chem 5, 2926–2941 (2019).
25. Hidalgo, T. et al. Biocompatible iron(iii) carboxylate metal-organic frameworks as promising RNA nanocarriers. Nanoscale 12, 4839–4845 (2020).

26. Tong, P. H. et al. Metal-organic frameworks (MOFs) as host materials for the enhanced delivery of biomacromolecular therapeutics. *Chemical Communications Preprint* at <https://doi.org/10.1039/d1cc05157a> (2021).
27. He, Y. et al. Metal-Organic Frameworks for Gene Therapy and Detection. *Advanced Functional Materials* vol. 33 Preprint at <https://doi.org/10.1002/adfm.202212277> (2023).
28. Poddar, A. et al. Encapsulation, Visualization and Expression of Genes with Biomimetically Mineralized Zeolitic Imidazolate Framework-8 (ZIF-8). *Small* 15, (2019).
29. Chu, Y. et al. Biomimetic synthesis of coordination network materials: Recent advances in MOFs and MPNs. *Applied Materials Today* vol. 10 93–105 Preprint at <https://doi.org/10.1016/j.apmt.2017.12.009> (2018).
30. Liang, K. et al. Biomimetic mineralization of metal-organic frameworks as protective coatings for biomacromolecules. *Nat Commun* (2015) doi:10.1038/ncomms8240.
31. Mirzazadeh Dizaji, N. et al. Biomimetic Mineralization of Iron-Fumarate Nanoparticles for Protective Encapsulation and Intracellular Delivery of Proteins. *Chemistry of Materials* 34, 8684–8693 (2022).
32. Järvinen, P., Oivanen, M. & Lönnberg, H. Interconversion and Phosphoester Hydrolysis of 2',5'- and 3',5'-Dinucleoside Monophosphates: Kinetics and Mechanisms. *Journal of Organic Chemistry* (1991) doi:10.1021/jo00018a037.
33. Sameni, M. et al. ZIF-8 Nanoparticle: A Valuable Tool for Improving Gene Delivery in Sperm-Mediated Gene Transfer. *Biol Proced Online* 26, (2024).

34. Sharifnia, Z. et al. In-vitro transcribed mrna delivery using plga/pei nanoparticles into human monocyte-derived dendritic cells. *Iranian Journal of Pharmaceutical Research* 18, 1659–1675 (2019).
35. Li, S. et al. Payload distribution and capacity of mRNA lipid nanoparticles. *Nat Commun* 13, (2022).

5.6. Supplementary figures

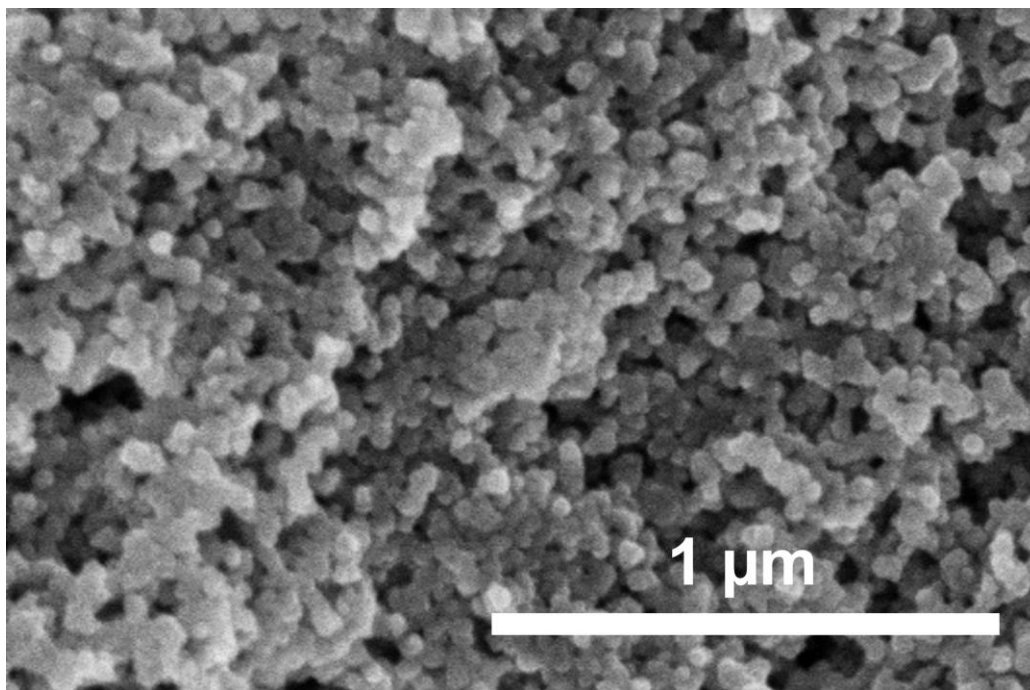


Figure S 5-1. SEM micrograph of Fe-fum NPs synthesized via biomimetic mineralization technique in the presence of mRNA.

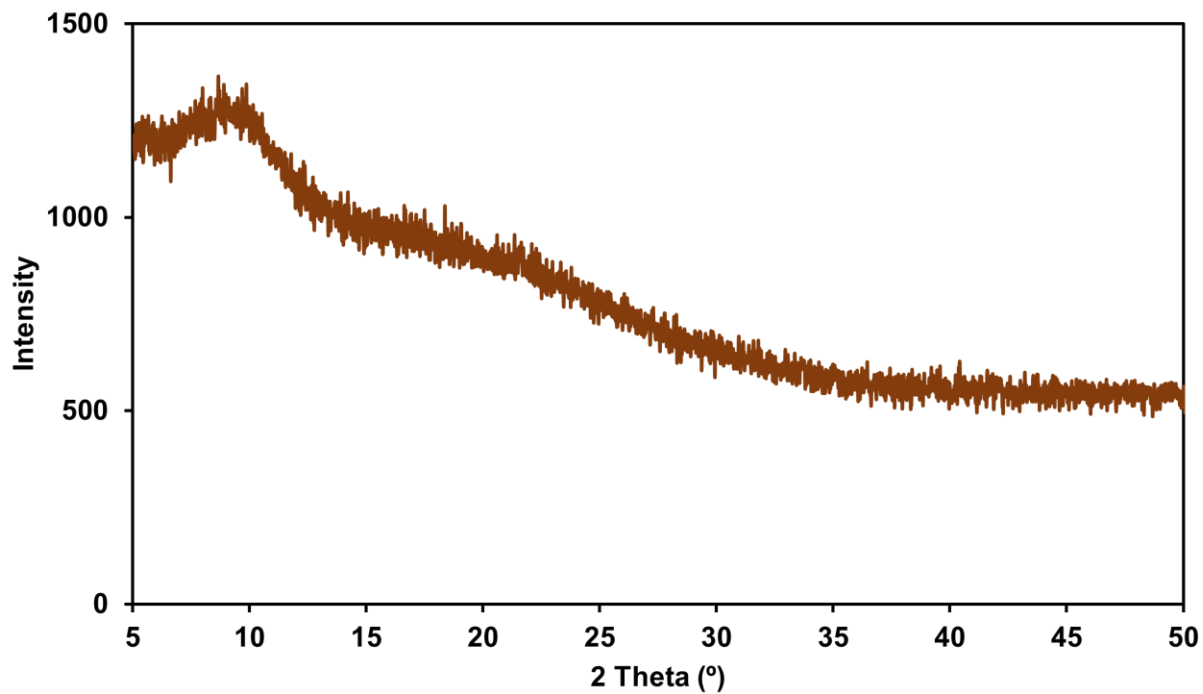


Figure S 5-2. XRD measurements of iron fumarate nanoparticles

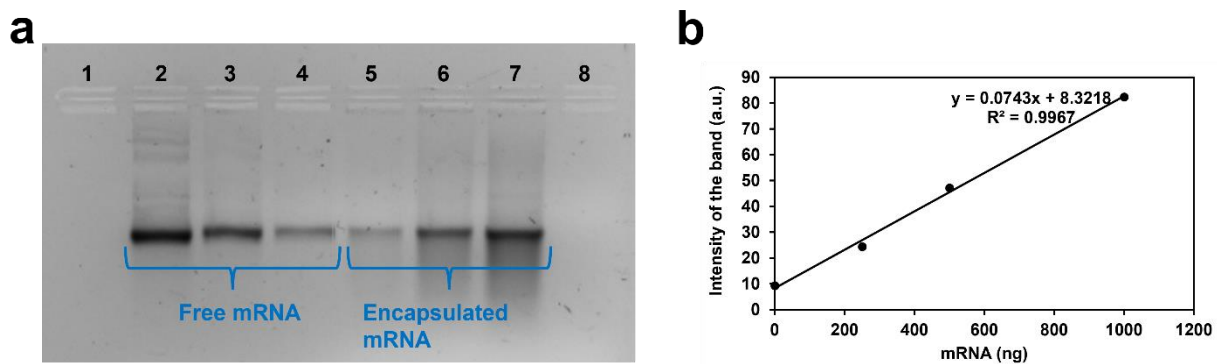


Figure S 5-3. Agarose gel assay of free mRNA and mRNA-loaded iron fumarate nanoparticles (mRNA@Fe-fum). (a) Agarose gel electrophoresis with free mRNA or degraded mRNA@Fe-fum. Lane 1 is without any treatment, and lanes 2-4 represent free mRNA containing 1, 0.5, and 0.25 μg of mRNA, respectively. Lanes 5-7 illustrate the degraded mRNA@Fe-fum synthesized in the presence of 2, 4, and 8 μg of mRNA, respectively. Lane 8 represents the Fe-fum NPs without mRNA. (b) The standard curve illustrating the correlation between mRNA mass and gel band intensity

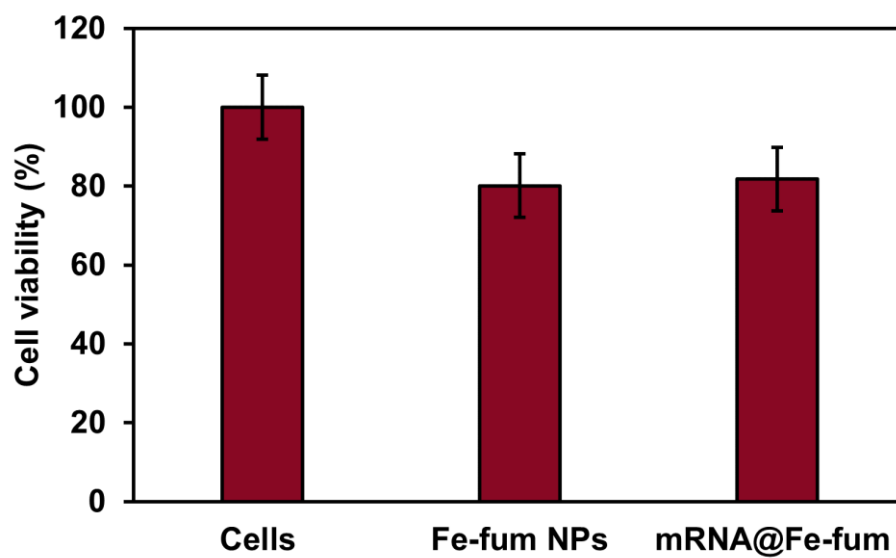


Figure S 5-4. Viability of *HeLa* cells treated with lipid-coated and calcein-loaded Fe-fum NPs and mRNA@Fe-fum for 72 h measured with an MTT assay (n=8).

CHAPTER 6

Conclusion and Outlook

6. Conclusion and Outlook

This thesis aimed to develop iron fumarate nanoparticles (Fe-fum NPs) as a robust platform for the delivery of biomacromolecules. The work explored various facets of nanoparticle synthesis, characterization, and application, focusing on proteins, ribonucleoproteins (RNPs), and messenger RNA (mRNA). The following summarizes the key findings and insights derived from each chapter of the thesis and outlines future directions for this research.

In the third chapter, we addressed the challenge of controlling the size of Fe-fum NPs under protein-friendly synthesis conditions via the biomimetic mineralization technique. Initial attempts to optimize synthesis conditions resulted in increased nanoparticle size and aggregation, which posed significant challenges. By systematically investigating various synthesis parameters, including the method for iron addition, the use of modulators, various dispersants, and lipid coating, we identified conditions that allowed for the production of small, uniformly sized nanoparticles in the range suitable for drug delivery purposes.

Furthermore, we investigated various strategies to enhance the cellular release of encapsulated cargo. We demonstrated that glucose shock was a highly efficient method for promoting the release of both proteins and small molecules from the nanoparticles. Moreover, the introduction of histidine as an internal trigger enhanced the release efficiency of small molecule cargo, although it was not as effective for protein cargo. This finding highlights the need for further research to identify suitable triggers for the efficient release of larger biomacromolecules.

The fourth chapter delved into the incorporation of various proteins and ribonucleoprotein (RNP) complexes into Fe-fum NPs, highlighting the versatility of our developed technique. The Fe-fum

NPs demonstrated high loading efficiency for different model proteins, including bovine serum albumin (BSA), green fluorescent protein (GFP), horseradish peroxidase (HRP), and Cas9/sgRNA RNPs. These nanoparticles successfully delivered the proteins into cells, maintaining their structural integrity and biological activity. Specifically, the delivery of Cas9/sgRNA RNPs achieved efficient gene knockout in *HeLa* cells, demonstrating the functional delivery capability of Fe-fum NPs. Furthermore, the Fe-fum NPs provided significant protection to the encapsulated RNP against degrading conditions, such as acidic pH, and allowed for long-term storage at 4 °C for over two months.

In a continuation of our work with Fe-fum NPs, the fifth chapter explored the encapsulation and delivery of RNA with a focus on mRNA molecules. The nanoparticles successfully encapsulated mRNA while maintaining its integrity. To validate the functionality of the encapsulated mRNA, we used mCherry-encoding mRNA as a model system. Upon delivery into cells, the Fe-fum NPs facilitated the expression of the mCherry protein, indicating that the mRNA remained intact and functional throughout the encapsulation and delivery process. This successful translation of mCherry within the cells underscored the potential of Fe-fum NPs to deliver functional mRNA.

In summary, the research presented in this thesis has established Fe-fum NPs as a versatile and effective platform for the delivery of biomacromolecules. The ability to control nanoparticle size and encapsulate a variety of proteins, RNPs, and functional mRNA highlights this system's broad applicability. The findings contribute to the advancement of nanoparticle-based delivery systems, offering promising solutions for medical and biotechnological applications.

Future research should focus on further optimizing the synthesis conditions to enhance the loading efficiency and release profiles for different types of biomacromolecules. Identifying suitable

internal triggers for the release of larger molecules, such as proteins, remains a key area for investigation. Additionally, exploring the protective capabilities of Fe-fum NPs for mRNA and other delicate biomolecules under various conditions will be crucial for their successful application in clinical settings.

Continued development of Fe-fum NPs could lead to significant advancements in the delivery of therapeutic proteins, genetic materials, and mRNA-based vaccines. By addressing the current challenges and building upon the foundation laid by this research, Fe-fum NPs have the potential to become a cornerstone technology in the field of nanomedicine and biotechnology.

CHAPTER 7

Curriculum Vitae

7. Curriculum Vitae

Personal Information

Name	Mirzazadeh Dizaji, Negar
Place of Birth	Tabriz, Iran
Nationality	Iranian

Education

April 2019- December 2024	PhD in Chemistry and Pharmacy Ludwig-Maximilians Universität München, Munich, Germany Supervisors: Prof. Thomas Bein and Prof. Hanna Engelke <u>Thesis:</u> Iron Fumarate Nanoparticles as Carriers for Functional Biomacromolecules
September 2012- September 2014	Mater of Science in Chemical engineering, Biotechnology Tarbiat Modares University Tehran, Iran Supervisors: Prof. Abbas Shojaosadati and Prof. Dina Morshedi <u>Thesis:</u> An Investigation on the Effect of Albumin Nanoparticles Size on Fibrillation of Alpha-synuclein.
September 2007- September 2011	Bachelor of Science in Chemical engineering Sahand University of Technology Tabriz, Iran

Publications

1. **Negar Mirzazadeh Dizaji**, Stefan Wuttke, Ulrich Lächelt, Thomas Bein and Hanna Engelke. “Control of aggregation and degradation of iron fumarate nanoparticles for protein encapsulation and intracellular delivery”, *under preparation*
2. **Negar Mirzazadeh Dizaji**, Alexander Borodavka, Thomas Bein and Hanna Engelke. “Intracellular delivery of mRNA by iron fumarate nanoparticles”, *under preparation*
3. **Negar Mirzazadeh Dizaji**, Yi Lin, Thomas Bein, Ernst Wagner, Stefan Wuttke, Ulrich Lächelt, and Hanna Engelke. “Biomimetic Mineralization of Iron-Fumarate Nanoparticles for Protective Encapsulation and Intracellular Delivery of Proteins”. *Chemistry of Materials* **2022**; 34 (19): 8684-8693
4. **Negar Mirzazadeh Dizaji**, Hossein Mohammad-beigi, Farhang Aliakbari, Amir Tayaranian Marvian, Seyed Abbas Shojaosadati, Dina Morshedi. “Inhibition of lysozyme fibrillation by human serum albumin nanoparticles: Possible mechanism”. *International Journal of Biological Macromolecules* **2016**; 93: 1328-1336
5. Hossein Mohammad-Beigi, Seyed Abbas Shojaosadati, Dina Morshedi, **Negar Mirzazadeh**, and Ayyoob Arpanaei. “The Effects of Organic Solvents on the Physicochemical Properties of Human Serum Albumin Nanoparticles”. *Iranian Journal of Biotechnology*. **2016**; 14(1): 45–50.